Oxygen ions as a single and combined modality in radiotherapy

Sauerstoff-Ionen als einzelne und kombinierte Strahlentherapie-Modalität
Vom Fachbereich Physik der Technischen Universität Darmstadt
zur Erlangung des akademischen Grades eines Doktors der Naturwissenschaften (Dr. rer. nat.)
genehmigte Dissertation von Dipl.-Phys. Olga Sokol aus Dubna, Russland
Tag der Einreichung: 29.01.2018, Tag der Prüfung: 09.04.2018
Darmstadt — D 17

1. Gutachten: Prof. Dr. Marco Durante
2. Gutachten: Prof. Dr. Thomas Aumann

TECHNISCHE UNIVERSITÄT DARMSTADT

GSI

Oxygen ions as a single and combined modality in radiotherapy
Sauerstoff-Ionen als einzelne und kombinierte Strahlentherapie-Modalität

Genehmigte Dissertation von Dipl.-Phys. Olga Sokol aus Dubna, Russland

1. Gutachten: Prof. Dr. Marco Durante
2. Gutachten: Prof. Dr. Thomas Aumann

Tag der Einreichung: 29.01.2018
Tag der Prüfung: 09.04.2018

Darmstadt — D 17

Bitte zitieren Sie dieses Dokument als:
URN: urn:nbn:de:tuda-tuprints-74541
URL: http://tuprints.ulb.tu-darmstadt.de/7454

Dieses Dokument wird bereitgestellt von tuprints,
E-Publishing-Service der TU Darmstadt
http://tuprints.ulb.tu-darmstadt.de
tuprints@ulb.tu-darmstadt.de

Die Veröffentlichung steht unter folgender Creative Commons Lizenz:
Namensnennung – Keine kommerzielle Nutzung – Keine Bearbeitung 4.0 International
http://creativecommons.org/licenses/by-nc-nd/4.0/

Abstract

Ion beam therapy is a rapidly developing branch of tumor treatment. Since ions deposit most of the energy at the end of their ranges, they are good candidates for an effective treatment of deeply-seated tumors together with an efficient sparing of the normal tissue in the beam entrance channel. Currently, only protons and carbon ions are used in clinics. This work aims at experimental study of the relevant properties and exploring the possibility of introducing another ion type, ^{16}O oxygen, to clinical practice, primarily for treatment of hypoxic tumors.

In this work, the first multi-scale description of ^{16}O beams, including their experimental characterization from the physical and radiobiological points of view, and the following treatment planning studies, is introduced. Apart from that, the new approach suggesting the irradiation of hypoxic tumors with several primary ions, implemented to the GSI in-house treatment planning system TRiP98, is described and the corresponding treatment planning study is carried out with oxygen and helium beams.

The verification of the absorbed dose profiles, as well as the *in vitro* cell survival experiments, including the measurements in hypoxia, were carried out at the Heidelberg Ion-Beam Therapy Center and GSI Helmholtz Centre for Heavy Ion Research (Germany). These experiments confirmed the present status of the physical and radiobiological beam models for oxygen beams and the reliability of the produced treatment plans. For the first time, the benefit of oxygen ions over carbon ions for irradiation of hypoxic tumors was experimentally indicated. The further comparative study of the treatment plans with oxygen and lighter ion beams revealed that the usage of oxygen ions for hypoxic tumors allows the most uniform target coverage, decrease of the dose received by residual tissue in the entrance channel and avoiding local dose hotspots in the organs at risk. Treatment planning studies using the kill-painting approach suggested that by combining heavy and light primary beams within the same treatment plan one can further improve the outcome of radiotherapy for some cases of hypoxic tumors due to the further reduction of dose received by the critical structures and residual tissue.

Zusammenfassung

Die Ionenstrahltherapie ist ein sich rasch entwickelnder Zweig der Tumorbehandlung. Da Ionen den größten Teil der Energie am Ende ihrer Reichweite deponieren, sind sie gute Kandidaten für eine effektive Behandlung von tief sitzenden Tumoren und ermöglichen gleichzeitig eine effiziente Schonung des Normalegewebes im Strahleingangskanal. Derzeit werden nur Protonen und Kohlenstoff-Ionen in Kliniken verwendet. Ziel dieser Arbeit war eine experimentelle Untersuchung der relevanten Eigenschaften und eine Analyse der Möglichkeit, einen anderen Ionentyp, ^{16}O Sauerstoff, hauptsächlich zur Behandlung von hypoxischen Tumoren, in die klinische Praxis einzuführen.

In dieser Arbeit werden die erste umfassende Beschreibung von ^{16}O-Ionen einschließlich ihrer experimentellen Charakterisierung sowohl aus physikalischer als auch aus strahlenbiologischer Sicht sowie die daraus folgenden Studien zur Behandlungsplanung vorgestellt. Darüber hinaus wird ein neuer Ansatz zur Bestrahlung von hypoxischen Tumoren mit mehreren Primärionen beschrieben, der in das hauseigene Bestrahlungsplanungssystem TRiP98 von GSI implementiert wurde. Die entsprechende Behandlungsplanung wird mit Sauerstoff- und Heliumstrahlen durchgeführt.

Die Verifizierung der Energiedosisprofile sowie die *in vitro* Zellüberlebensexperimente einschließlich der Messungen in Hypoxie wurden am Heidelberger Ionenstrahl-Therapiezentrum und am GSI Helmholtz-Zentrum für Schwerionenforschung (Deutschland) durchgeführt. Diese Experimente bestätigten den aktuellen Stand der physikalischen und strahlenbiologischen Modelle für Sauerstoff-Ionen und die Zuverlässigkeit der erstellten Bestrahlungspläne. Zum ersten Mal konnte experimentell gezeigt werden, dass Sauerstoff-Ionen gegenüber Kohlenstoff-Ionen für die Bestrahlung von hypoxischen Tumoren von Vorteil sein können. Der weitere Vergleich der Bestrahlungspläne mit Sauerstoff- und leichteren Ionenstrahlen ergab, dass die Verwendung von Sauerstoff-Ionen für hypoxische Tumore eine möglichst gleichmäßige Zielerfassung, eine Verringerung der Dosis im Eingangskanal und eine Vermeidung lokaler Dosis-Hotspots in kritischen Organen ermöglicht. Der hier vorgeschlagene Ansatz, der kill-painting mit der Verwendung von mehreren Ionentypen mit verschiedenen Eigenschaften in einem Bestrahlungsplan verbindet, kann den Therapieerfolg für einige Fälle von hypoxischen Tumoren verbessern, da eine zusätzliche Verringerung der Dosis im Normalgewebe und in kritischen Organen erreicht werden kann.

Contents

Introduction **11**

1. Research background and fundamentals **15**
1.1. Ion beam therapy . . . 15
1.1.1. Basic physics of ion beam therapy . . . 16
1.1.2. Beam delivery . . . 21
1.1.3. Relative biological effectiveness . . . 23
1.1.4. Local effect model . . . 26
1.1.5. TRiP98 treatment planning system . . . 27
1.2. Tumor hypoxia . . . 29
1.2.1. Definition and influence on the treatment planning . . . 29
1.2.2. Hypoxia imaging . . . 32

2. Experimental analysis of physical and radiobiological properties of oxygen beams **35**
2.1. Introduction . . . 35
2.2. Materials and methods . . . 35
2.2.1. Treatment planning . . . 35
2.2.2. Irradiation systems . . . 38
2.2.3. 3D absorbed dose measurements . . . 39
2.2.4. Biological measurements . . . 39
2.3. Results and discussion . . . 43
2.3.1. Physical dose verification . . . 43
2.3.2. Relative biological effectiveness . . . 44
2.3.3. Oxygen enhancement ratio . . . 49
2.3.4. Extended hypoxic target irradiation . . . 50
2.3.5. Summary . . . 53

3. Treatment planning studies with oxygen beams **55**
3.1. Introduction . . . 55
3.2. Materials and methods . . . 55
3.2.1. Model volume studies . . . 55
3.2.2. Patient plans . . . 57
3.3. Results and discussion . . . 60
3.3.1. Basic analysis accounting for target hypoxia . . . 60

3.3.2. Tumor control probability analysis 63
3.3.3. Analysis of patient plans from GSI pilot project 67
3.3.4. Summary 82

4. Multiple ion treatment planning involving oxygen beams 85
4.1. Introduction 85
4.2. Materials and methods 86
4.2.1. TRiP98-multiion-OER 86
4.2.2. RBE- and OER-weighted dose calculation 86
4.3. Results and discussion 88
4.3.1. Dose redistribution for unevenly oxygenated tumors 88
4.3.2. Comparison with single-ion optimized plans 91
4.3.3. Summary 104

Summary and conclusion 105

A. X-ray response of CHO-K1 cell line 109

B. Water equivalent ratio of materials used in cell irradiation setups 111

C. Calibration for beam monitors in ^{16}O beam at HIT facility 113

D. Measurements of the pinpoint chambers for the absorbed dose profiles verification 115

E. Survival measurements for the data presented in Chapter 2 121

F. Optimization accounting for a three-dimensional pO_2 distribution 125

G. Entrance channel survival data used for analysis in Chapter 3 129

References 133

List of abbreviations

ACC	Adenoid Cystic Carcinoma
BED	Biologically Effective Dose
BNL	Brookhaven National Laboratory
CNAO	Centro Nazionale di Adroterapia Oncologica (The National Centre for Oncological Hadrontherapy)
CT	Computer Tomography
CSDA	Continuous Slowing Down Approximation
DKFZ	Deutsches Krebsforschungszentrum (German Cancer Research Center)
DSB	Double Strand Break
DVH	Dose-Volume Histogram
FMISO	Fluoromisonidazole
FWHM	Full Width at Half Maximum
GSI	Gesellschaft für Schwerionenforschung (German Centre for Heavy Ion Research)
HC	Hypoxic Chamber
HIT	Heidelberger Ionenstrahl-Therapiezentrum (Heidelberg Ion Beam Radiotherapy Centre)
LEM	Local Effect Model
LET	Linear Energy Transfer
LQ	Linear-Quadratic
MDF	Maximal Dose Fraction
MRI	Magnetic Resonance Imaging
NTCP	Normal Tissue Complication Probability
OAR	Organ at Risk
OER	Oxygen Enhancement Ratio
PER	Peak to Entrance Ratio
PET	Positron Emission Tomography
PIDE	Particle Irradiation Data Ensemble
PMMA	Polymethylmethacrylat
PTCOG	Particle Therapy Co-Operative Group
RBE	Relative Biological Effectiveness
RT	Radiation Therapy
SEM	Standard Error of the Mean

SIS18	GSI Heavy Ion Synchrotron (Schwerionensynchrotron)
SOBP	Spread-Out Bragg Peak
TCF	Tissue Culture Flask
TCP	Tumor Control Probability
TPS	Treatment Planning System
TRiP98	Treatment Planning for Particles (GSI software for treatment planning)
UNILAC	Universal Linear Accelerator
VOI	Volume of Interest
WEPL	Water-Equivalent Path length
WF	Weight Factor

Publications related to this work

Peer-reviewed articles

Krämer, M., Scifoni, E., Schmitz, F., **Sokol, O.** and Durante, M., 2014. Overview of recent advances in treatment planning for ion beam radiotherapy. *The European Physical Journal D*, 68(10), p.306.

Sokol, O., Scifoni, E., Tinganelli, W., Kraft-Weyrather, W., Wiedemann, J., Maier, A., Boscolo, D., Friedrich, T., Brons, S., Durante, M. and Krämer, M., 2017. Oxygen beams for therapy: advanced biological treatment planning and experimental verification. *Physics in medicine and biology*, 62(19), pp.7798-7813.

Scientific reports

Sokol, O., Scifoni, E., Tinganelli, W., Brons, S., Friedrich, T., Durante, M. and Krämer, M., 2015. Biological characterization of therapeutic oxygen beams. *GSI Scientific Report 2015*.

Scifoni, E., Tinganelli, W., Durante, M., **Sokol, O.** and Krämer, M., 2015. Advances in OER-driven biological optimization with ion beams. *GSI Scientific Report 2015*.

Sokol, O., Scifoni, E., Hild, S., Durante, M. and Krämer, M., 2016. Towards the multi-ion treatment planning with ^{16}O beams. *GSI Scientific Report 2016*.

Introduction

First proposed in the 1970s in Berkeley [Tobias et al., 1971], cancer therapy with heavy ions has recommended itself as a promising alternative to the therapy with photons and protons. In contrast to the first type of irradiation, due to the 'inverse' depth-dose profile, ions achieve the same level of conformity for the tumor irradiation, while sparing the residual tissue more efficiently [Schardt et al., 2010; Loeffler and Durante, 2013]. At the same time, compared to protons, heavier ions offer reduced lateral scattering and higher radiobiological effectiveness, thus leading to enhanced cell kill in the Bragg peak region [Durante and Loeffler, 2009]. The branch of tumor treatment with particles is rapidly growing, and, by the end of 2015, about 150 000 patients received the corresponding treatment [Jermann, 2016]. Apart from protons, at the moment the facilities in operation offer the treatment only with carbon ions, while some of them are in principle able to deliver other particles. However, in the past decade the interest towards introducing other modalities to the clinical practice has increased.

In particular, ^{16}O oxygen beams are being widely discussed mainly due to their increased linear energy transfer (LET). The main benefit one can get from this feature is the possibility to overcome the problem of increased radiosensitivity of hypoxic tumors [Baverstock and Burns, 1976; Michael, 1996] due to the decreased values of oxygen enhancement ratio. The semi-empirical models, describing the OER-LET dependencies based on the available experimental data [Wenzl and Wilkens, 2011; Stewart et al., 2011; Scifoni et al., 2013; Antonovic, 2014; Bopp et al., 2016] predict the drastic reduction of OER when the particle LET exceeds the value of $\approx$100 keV/μm. The first trials with high-LET particles, mainly with neon ^{20}Ne, were carried out at Berkeley times [Tobias et al., 1982; Castro, 1995], however, at that time there was no sufficient knowledge about the beam radiobiological properties. Researchers came back to the idea of using heavier ions when the ideas of LET redistribution in the treatment plan were proposed by the different groups (the so-called 'LET-painting' [Bassler et al., 2010, 2014] or 'kill-painting' [Scifoni et al., 2013; Tinganelli et al., 2015] approaches).

At the same time, the use of ^{16}O ions possesses several drawbacks that need to be taken into account, such as an increased dose behind the Bragg peak and in the entrance channel, caused by the increased portion of nuclear fragmentation. Additionally, the increased relative biological effectiveness (RBE) compared to the lighter ions, may also lead to an unnecessary damage to residual tissue. Thus, the successful treatment of tumors with ^{16}O beams requires the precise knowledge about its physical and radiobiological properties, as well as complementary comparative treatment planning studies to identify in which cases they can be the most beneficial.

While already a few modern facilities offer ^{16}O beams at a high level of dosimetric accuracy, the full description of the beam is still missing. [Kurz et al., 2012] were the first to report the results of experimental verification of physical depth dose distributions of oxygen ions at Heidelberg Ion Beam Radiotherapy Centre (HIT). Further studies of ^{16}O beams properties are continued in the works of [Dokic et al., 2016; Tessonnier et al., 2017a,b], aimed at comparing them with the lighter modalities, such as ^{12}C, ^{4}He, and protons, from physical and also radiobiological points of view.

Despite the few treatment planning systems (TPS) starting to be able to handle ^{16}O beam model for planning [Tessonnier et al., 2017a; Inaniwa et al., 2017; Resch et al., 2017], the GSI in-house TPS TRiP98 is the only TPS that is able to perform the optimization accounting for the biological properties of the beam and tumor oxygenation. The latter is possible thanks to the newly introduced "kill-painting" approach [Tinganelli et al., 2015] which by the start of the current project was tested only with carbon ions.

In parallel to the idea of developing the tumor therapy with alternative ions, the interest in combining several ions inside a single therapy session is rising. This way, the flexibility of treatment planning is expected to be increased due to considering and optimally combining the physical and the radiobiological properties of all the relevant ions, thus also avoiding the negative consequences caused by one ion by replacing it with another one if needed. Moreover, this idea can be technically possible due to the recently reported short switching times between the different ion species [Toshiba, 2017]. The first indications of the benefits of such an approach were the use of a boost radiation during the treatment of patients. During the GSI pilot project, this was a carbon boost for a smaller region of the tumor, after the primary irradiation with photon fields. The later study presented by [Schulz-Ertner et al., 2005] demonstrated almost a three-fold increase of the locoregional control after four years for the patients with ACC treated in 1995-2003, who received a carbon boost in addition to the photon therapy, compared to those who received the photon treatment only.

The study of [Böhlen et al., 2013] was already proposing the idea of achieving the constant RBE inside the target by combining protons and carbon ions inside one treatment plan by optimizing with a constraint of a minimum variation of RBE through all the target. However, the price to pay was the increase of the cell kill in the entrance channel. Another approach introduced in the same work was the delivering of a heavy-ion boost to hypoxic regions of the target to achieve a constant biological dose distribution. The latter idea arose from the previously published works on dose- and LET-painting methods, introducing the ideas of redistributing the particles LET during the treatment planning [Bassler et al., 2010; Brahme, 2011; Bassler et al., 2014; Unkelbach et al., 2016]. The recent paper of [Inaniwa et al., 2017] demonstrated the first implementation of the intensity modulated composite particle therapy (IMPACT), which enables the optimization of the dose and the LET distributions in a patient. At this point, no radiobiological models were included in the planning, and the optimization was carried out only for the absorbed dose and a given LET.

Nowadays the only TPS which can perform the simultaneous biological optimization of several different ion fields is TRiP98. [Krämer et al., 2014] demonstrated a proof-of-concept example of such optimization with ^{12}C and protons for a C-shaped target representing the tumor wrapping an OAR. However, up to now, there was no tool available, which can simultaneously perform the optimization of several ion fields, accounting at the same time for the tissue radiosensitivity and tumor hypoxia.

The presented work was pursuing two goals:

- Further characterization of ^{16}O ion beams aimed at their future implementation in clinics. For that, its relevant physical and radiobiological properties were studied and verified experimentally, and extensive treatment planning tests with ^{16}O beams were carried out.
- Enabling the optimization with several primary ions accounting for tumor hypoxia by expanding the current version of TRiP98 TPS, and testing its validity with ^{16}O beams.

The structure of this dissertation is as follows. Chapter 1 gives an overview of the current status of ion beam therapy and the related physical aspects. In Chapter 2 the results of experimental verification of oxygen beam properties, relevant for their clinical application in radiation therapy are reported. This implies the absorbed dose profiles verification, as well as the radiobiological measurements in normoxia and hypoxia. In Chapter 3 the results of the comparative treatment planning tests with oxygen beams are presented for normoxic and hypoxic targets. The idea of further improvement of the treatment of hypoxic tumors with oxygen beams by combining them with the lighter modalities inside one treatment plan is proposed and tested in Chapter 5. The work is rounded up with a conclusion which summarizes the main results and discusses the necessary future steps.

1 Research background and fundamentals

1.1 Ion beam therapy

The principal goal of cancer therapy is to eliminate all the cancer stem cells in a primary tumor and regional lymph nodes while avoiding the damage to the residual tissue as much as possible [Baumann et al., 2016]. Nowadays radiotherapy is one of the essential components of cancer therapy along with surgery and chemotherapy, and quite often these methods are used in combination.

About 80% of the people receiving the radiotherapy are getting treatment with X-rays, the rest is treated with the brachytherapy or gamma-knife; the ion beam therapy with protons or heavier ions is only 0.8% [Durante and Paganetti, 2016]. However, the number of patients, who received this treatment, is increasing every year.

The pioneering work was conducted at Lawrence Berkley Laboratory (USA) where 2487 patients were treated in 1957-1992 [Castro, 1995; Castro et al., 1994]. The treatment was carried out with ^{4}He helium beams and heavier modalities such as neon ^{20}Ne, with which 440 patients were treated. Apart from that, few patients were exposed to ^{18}Ar and ^{14}Si, however, these trials had to be terminated because of the severe side effects since at that time no proper radiobiological model for heavy existed.

Currently, the ion beam therapy is performed only with protons and ^{12}C ions. Since the Berkeley times, the related physical and radiobiological knowledge have significantly improved. However, there are still many challenges remaining. Among them are the intrafractional moving of several tumor types such as lung cancer, the problem of describing the radiobiological response of the tissue using the particles' RBE, tumor hypoxia, etc. Despite that, the number of patients is rapidly growing. According to [Jermann, 2011, 2016], in the last five years, the total number of patients treated with ions had increased almost twice from 84492 to 154203. Regarding the operating facilities, currently, there are in total 11 ^{12}C centers, situated in Germany (2), Japan (5), China (2), Italy (1) and Austria (1). Regarding the proton therapy centers, the geographical distribution is much broader, and there are 64 facilities in 17 countries [PTCOG, 2016a]. Figure 1.1 summarizes the PTCOG most recent data. Apart from that, at the time of this writing there are 41 facilities in the building stage [PTCOG, 2016b].

While only the two ion types are actually being used, there is a high interest in implementing the alternative modalities, such as ^{4}He or ^{16}O. The first one is mainly discussed as an alternative to protons (a so-called "better proton") and the plans on the start of the clinical trials in the next years are being reported [Haberer et al., 2017]. The physical and radiobiological evidence for using these ions will be addressed in the following sections in this chapter.

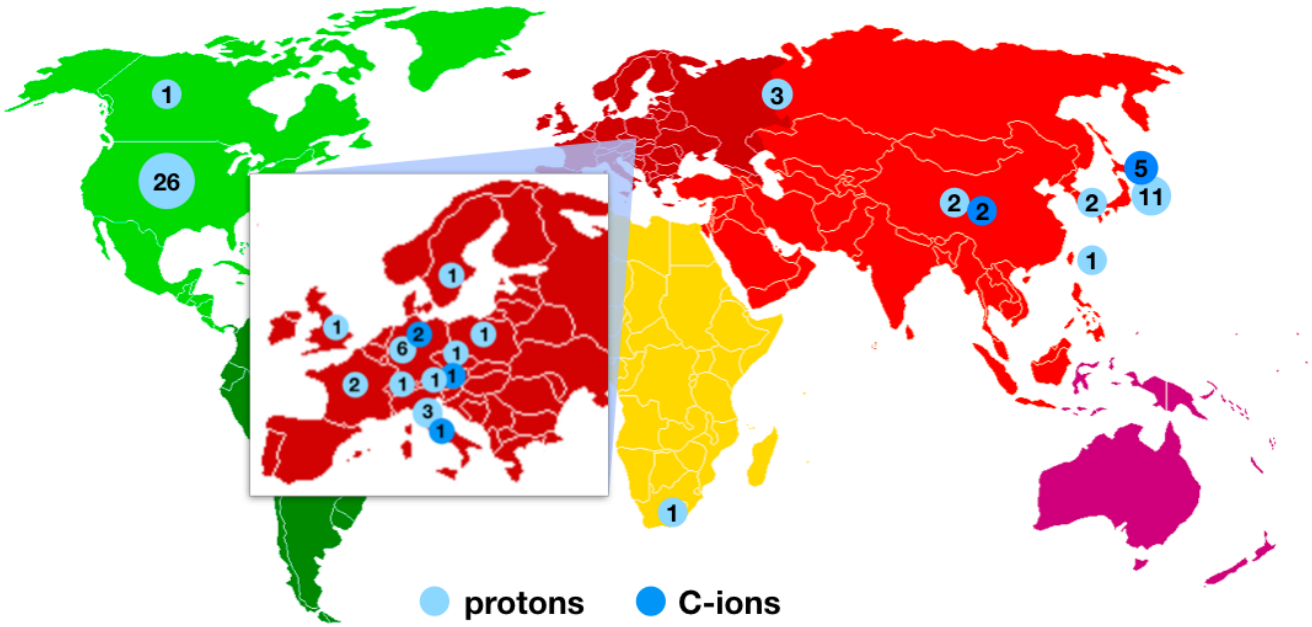

Figure 1.1.: Geographical distribution of the operating proton and carbon ion radiotherapy centers. The numbers in circles represent the number of corresponding centers in the country. Based on the statistics provided by PTCOG [PTCOG, 2016a].

1.1.1 Basic physics of ion beam therapy

The main argument for using ions in radiotherapy is their inverse depth-dose profile, often referred as a Bragg curve [Bragg and Kleeman, 1905]. In contrast to the X-ray radiation, demonstrating the steep energy decrease in depth, or a broad peak near the surface of the patient's body, the depth-dose distribution for protons or heavy ions has a pronounced narrow maximum at the end of the range while delivering a relatively low dose in the entrance channel.

In radiotherapy, the absorbed dose is measured in Gray [Gy] and is defined as the energy dE absorbed in a mass element dm:

$$D = \frac{dE}{dm} \quad \left[1\text{Gy} = 1\frac{\text{J}}{\text{kg}}\right]. \tag{1.1}$$

The dose delivered in a thin layer of material by the parallel beam with particle fluence F can be calculated as follows:

$$D[Gy] = 1.6 \times 10^{-9} \times \frac{dE}{dx}\left[\frac{\text{keV}}{\mu\text{m}}\right] \times F[\text{cm}^{-2}] \times \frac{1}{\rho}\left[\frac{\text{cm}^3}{\text{g}}\right], \tag{1.2}$$

with dE/dx standing for the energy loss per unit path length ('stopping power') and ρ for the density of the material.

The main physical process contributing to the longitudinal profile of the ion beams is the ionization of the atomic shell electrons. The lateral profile, characterizing the beam broadening, is mainly affected by the elastic scattering on the target nuclei. Another essential process affecting both the longitudinal and lateral profiles of the beam is the nuclear fragmentation.

Electromagnetic energy loss

The total stopping power for the ion is the sum of those for the electromagnetic energy loss, due to interactions with the nuclei and due to radiative energy losses. The latter two, however, are not relevant for the ions of therapeutic energies.

The electromagnetic energy loss rate dE/dx of the ion due to the inelastic collisions with the electrons of the target is described by the Bethe-Bloch formula [Bethe, 1930; Bloch, 1933; Fano, 1963]:

$$\frac{dE}{dx} = \frac{4\pi e^4 Z_t Z_i^2}{m_e v^2}\left[\ln\frac{2m_e v^2}{I} - \ln\left(1-\beta^2\right) - \beta^2 - \frac{C}{Z_t} - \frac{\delta}{2}\right], \tag{1.3}$$

where Z_t and Z_i stand for the nuclear charges of the target and the ion, e and m_e are the electron charge and rest mass, v - the velocity of the ion, and $\beta = v/c$, where c is the speed of light in vacuum. The last two terms are the shell (corrects for atomic bindings in the material) and the density (for medium polarisation at high particle speeds) effects corrections, accordingly. The ionization energy of the target atom or molecule, I, for protons and ions in water is ≈78 eV [Schardt, 2007].

From the $1/v^2$ terms it follows, that the energy loss is increasing with decreasing energy of the particle. The peak region in the depth-dose distribution, where the energy loss of the ion reaches its maximum is called Bragg peak.

In the continuous slowing down approximation (CSDA), when the energy loss is assumed constant for every penetration depth, and the trajectory of the particle with initial energy E_0 to be a straight line, based on the equation 1.3 the range can be calculated as

$$R_{CSDA} = \int_0^{E_0} \frac{dE}{dE\ /\ dx}. \tag{1.4}$$

The statistical fluctuations of the energy loss lead to the broadening of the beam. The corresponding energy loss fluctuations [Vavilov, 1957] for the multiple collisions on a first approximation can be described by the Gaussian distribution and result in a range straggling. The ratio between the range straggling and the mean range remain nearly constant and is proportional to $1/\sqrt{M}$ where M stands for the particle mass. Thus, range straggling plays a less important role for the heavier particles, resulting in a narrower shape of the Bragg peak.

Lateral beam spread

The knowledge about the lateral scattering of the beam is essential for the estimation of the doses received by the organs at risk (OAR) [Kraft, 2000]. The spread of the lateral profile of the ions is caused by the elastic multiple Coulomb interactions with target nuclei. A commonly accepted theoretical description for this effect was given by [Moliére, 1948] and confirmed by the experiments with proton beams [Gottschalk et al., 1993]. The [Highland, 1975] approximation yields the following parametric equation for the characteristic multiple-scattering angle θ [rad]:

$$\sigma_\theta = \frac{14.1\ MeV}{\beta pc} Z_p \sqrt{\frac{L}{L_{rad}}} \left[1 + 0.038 \ln\left(\frac{L}{L_{rad}}\right)\right] \tag{1.5}$$

where βc, p, and Z_p are the velocity, momentum and nuclear charge of the projectile, respectively. L and L_{rad} characterize the thickness and the radiation length of the absorber. From the equation 1.5 the three conclusions can be made:

- The targets containing heavy elements cause increased scattering of the beam, compared to to the light-element targets of equal thickness;
- Due to the $1/(\beta pc)$ factor, the scattering decreases at higher energies;
- Heavier ions demonstrate a smaller lateral spread as compared to lighter beams at the same range.

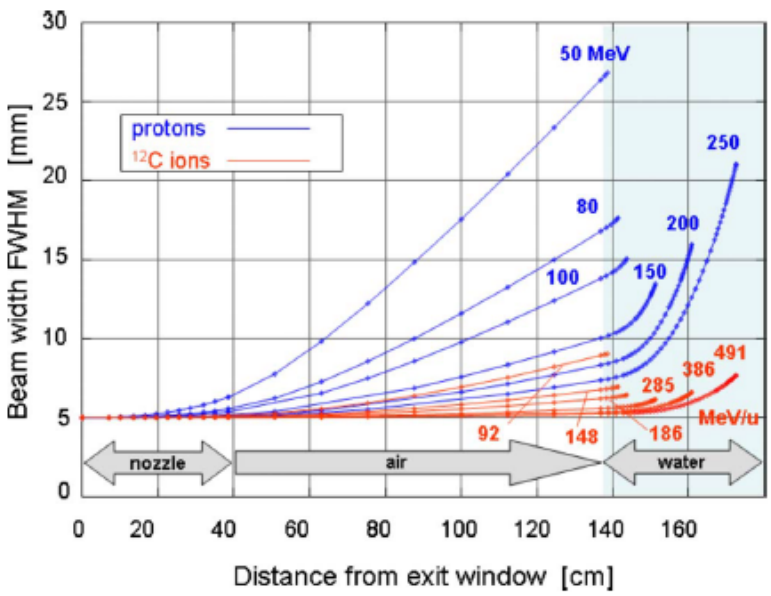

Figure 1.2.: Beam spread of the initially parallel narrow proton and ^{12}C ion beams in a typical treatment beam line. Figure taken from [Schardt et al., 2010].

Figure 1.2 demonstrates the lateral beam spread of protons and carbon ions in a typical beamline. The beam exits from a nozzle, passes the 1 m air gap and enters a water absorber.

^{12}C exhibit a significantly lower scattering and the final beam width for the given energies do not increase more than a factor of ≈1.5, while the scattering for protons is more significant.

Fragmentation

The knowledge of the fragmentation processes is essential for predicting the physical and radiobiological effect of the ion beams, especially for the heavier modalities. The study of [Lühr et al., 2012] has demonstrated the possible change of up to 10% in the prediction of the physical dose in the SOBP region due to the 20% uncertainties in inelastic nuclear cross sections.

In the particle therapy with ^{12}C ions only half of the primary ions reaches the Bragg peak while the rest undergoes fragmentation [Durante and Paganetti, 2016], which leads to the further lateral spread of the beam and the increased dose behind the Bragg peak, the so-called fragmentation tail. The TRiP98 treatment planning system prediction of the fragment spectra of the 160 MeV/u ^{16}O ion beam slowing down in water is shown in Figure 1.3. As can be seen, when the primary beam is lost at $z \approx 45$ mm depth, the remaining fragments, which are mainly protons and ^{4}He, travel more than twice this distance.

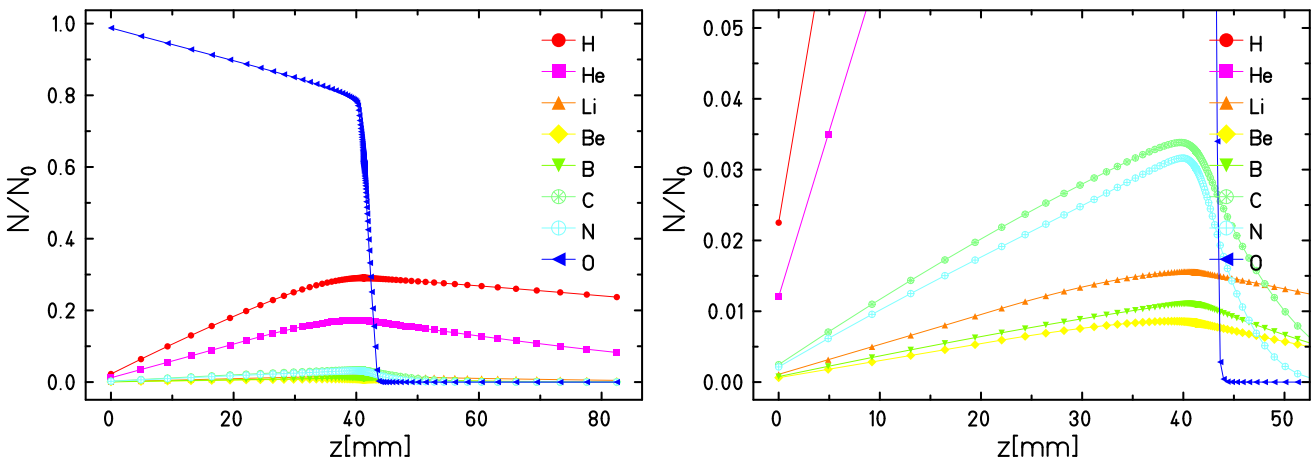

Figure 1.3.: Buildup of secondary fragments produced by 160 MeV/u ^{16}O beam slowing down in water, generated by the TRiP98 software (described below). The plot of the right is a zoom-in demonstrating the buildup of the heavier fragments.

The most commonly used model to describe the fragmentation process is abrasion-ablation (or cascade and evaporation) model [Serber, 1947; Hüfner et al., 1975], illustrated in Figure 1.4. At the abrasion stage, the nucleons in the projectiles overlap zone are sheared off forming the 'fireball', and the peripheral nucleons remain almost not affected. The velocity of the produced fragment is similar to the initial velocity and same refers to the ratio of mass over nuclear charge $(A/Z)_f \approx (A/Z)_p$. At the second stage (ablation) the remaining fragments de-excite by thermalizing or producing neutrons, protons and lighter nuclei until reaching their ground state. This step is described by a statistical model, with the probability of a fragment creation depending on the energy on the excitation energy gained in the previous stage. The produced

secondary fragments have the velocities very similar to the one of the primary projectile, and their ranges are generally longer.

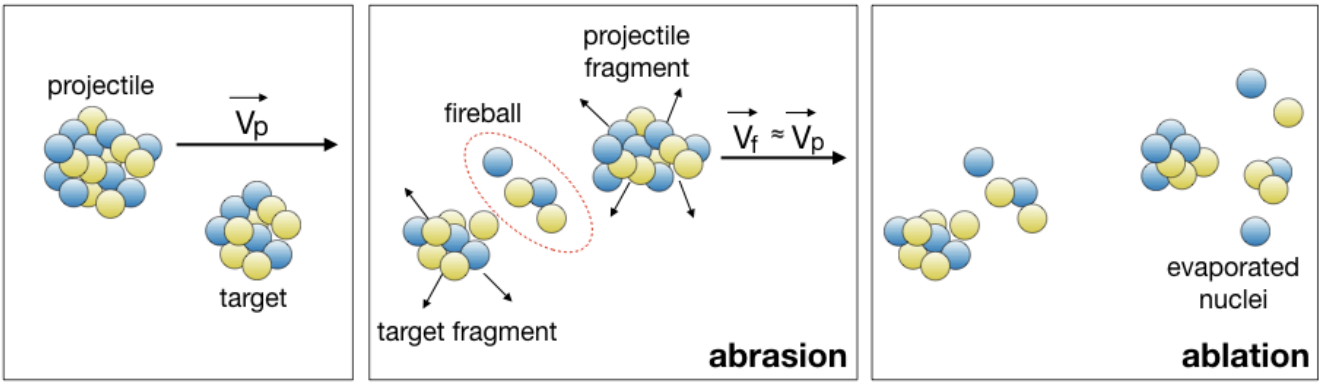

Figure 1.4.: Illustration of the abrasion-ablation model for nucleus-nucleus interactions at high energies. V_p and V_f stand for the velocities of the initial particle and its fragment, respectively.

The total reaction cross-section, describing the probability of all the possible nuclear reactions in the interaction of the projectile with the target via nuclear forces, and including the charge-changing and non-charge changing cross-sections, is the difference between the total and elastic cross-sections. It can be described by the Bradt-Peters formula [Bradt and Peters, 1950]:

$$\sigma_r = \pi r_0^2 \left(A_P^{1/3} + A_T^{1/3} - \delta\right)^2 \tag{1.6}$$

with A_P and A_T standing for the masses of the projectile and the target, $r_0 = 1.1$ fm for the effective nuclear radius, and δ being the correction (overlap) parameter. For the high-energetic beams (1-1.5 GeV/u), this formula gives an accurate description of σ_r, while for the lower therapeutic energies it requires additional energy-dependent corrections. For the description of the total reaction cross sections, the semi-empirical models of [Sihver et al., 1993; Kox et al., 1987] can be applied. According to all of these models, there is no significant change for the high-energetic beams with energies down to ≈100 MeV/u. With the further energy decrease, these models predict the increase of σ_r due to the mechanisms like deep inelastic collisions or fusion reactions.

One of the commonly accepted approaches to describe the energy dependence of the total reaction cross-sections, in particular, implemented to the GSI in-house TPS TRiP98, is the one suggested by [Tripathi et al., 1996, 1999]. According to it, the formula 1.6 can be expanded to

$$\sigma_r = \pi r_0^2 \left(A_P^{1/3} + A_T^{1/3} - \delta_E\right)^2 \left(1 - R_c \frac{B}{E_{cm}}\right). \tag{1.7}$$

The last multiplier in this equation describes the impact of Coulomb interaction at lower energies, with E_{cm} (MeV) standing for colliding system center of mass energy, and B being the Coulomb interaction barrier:

$$B = 1.44\ Z_p Z_t / R, \tag{1.8}$$

where Z_p and Z_t are the charges of the projectile and the the target, respectively, and R is the radius for evaluating the Coulomb barrier height. The transparency and Pauli blocking, relevant for the intermediate and high energies, are taken into account via the energy-dependent δ_E term. The semi-empirical Coulomb multiplier parameter R_c was introduced in order to adjust the underestimated Coulomb energy effect for the light systems, e.g., p+^{4}He, p+^{7}Li or p+^{12}C, based on the existing experimental data.

Several measurements of the charge-changing reactions cross-sections for ^{16}O beams with energies in the range of 200-700 MeV/u on water targets were published in the works of [Schardt et al., 1996; Schall et al., 1996; MacCabee and Ritter, 1974], however, further measurements in the therapeutic energy range are needed to benchmark the present TPSs.

1.1.2 Beam delivery

For successful treatment of the deep-seated tumors, the ions need to have a range of up to approximately 30 cm (for example, to treat the prostate cancer). This requires their acceleration to up to several hundred MeV/u and precise delivery to the desired location.

The acceleration of the ions for therapy nowadays is done with two kinds of accelerators, cyclotrons, and synchrotrons. While being relatively compact, cyclotrons have a disadvantage of offering only beams with constant energies and intensities. Thus, to achieve a desired dose distribution in the target, the use of the beam energy degraders is required. In contrast, the synchrotrons, used for the ion irradiation offer the active beam energy variation for each spill. The price for that is the required complicated ion optics; however, according to [Jäkel et al., 2008], synchrotrons are still expected to become a standard in radiotherapy after the improvement of the techniques used to control the beam position and intensity.

Apart from delivering the beam to the desired depth, creating the spread-out Bragg peak (SOBP) with its further shaping to the irregular tumor geometry is required to avoid the damage to the tissues in its proximity. Two techniques, the passive and active beam scanning, are used to achieve it.

The main idea of the passive beam delivery, which was historically the first method applied in the ion beam therapy, is shown in Figure 1.5(a), taken from [Schardt et al., 2010]. The initially narrow beam is broadened by the scattering system (typically with passive double scattering or a magnetic wobbler [Kraft, 2000]) and spread by the range modulator to cover the whole length of the tumor. The latter usually consists of rotating wheels of various thicknesses or a ridge filter [Chu et al., 1993]. The further beam shift in depth is possible using the range shifter which is a set of the absorber plates. After that, the unnecessarily large outer area of the beam is cut

using the collimator, and the depth pattern is shaped to the tumor by using the compensator. The disadvantage of this method is the dose deposition outside the tumor volume, which can be decreased by, e.g., using the dynamic collimator of variable width.

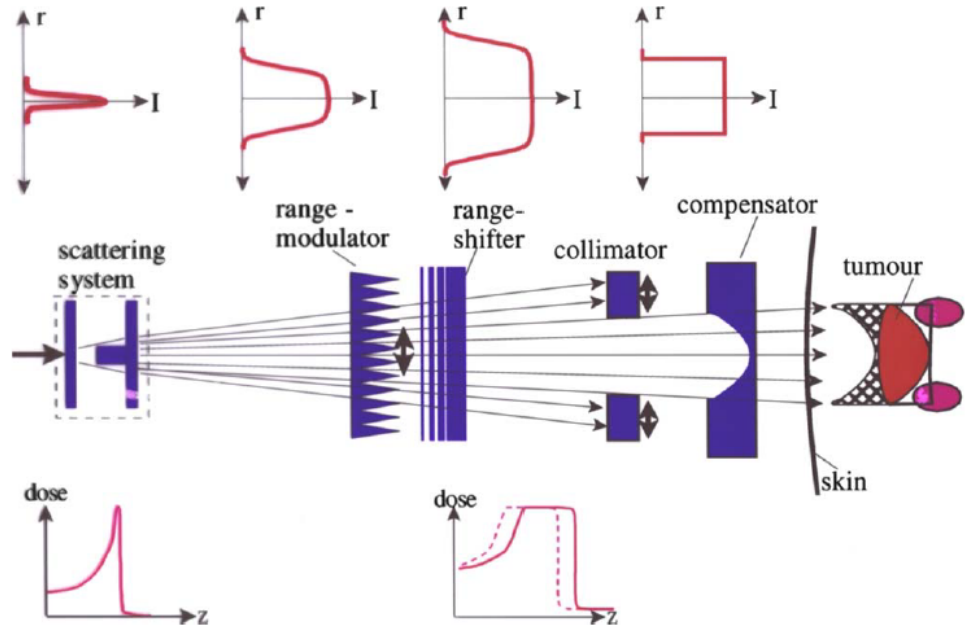

(a)

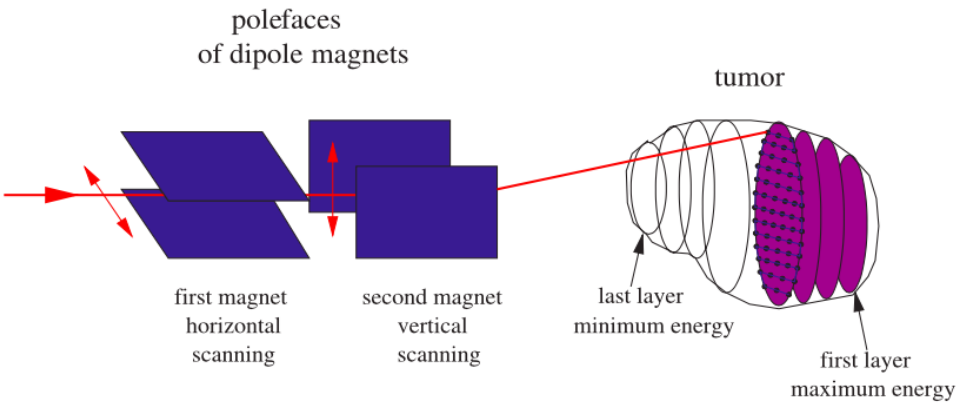

(b)

Figure 1.5.: Beam delivery systems used in ion beam therapy. (a) Passive beam delivery system, figure taken from [Schardt et al., 2010]. (b) Active beam delivery system, figure taken from [Kraft, 2007].

The second method, active beam scanning, firstly developed at NIRS in Japan [Kanai et al., 1983], is considered to be more advanced. The same publication of [Jäkel et al., 2008] predicts it becoming a standard for RT. The principle of the active beam delivery system is illustrated in Figure 1.5(b). The target volume is divided into several layers in depth to which the narrow pencil beam of the corresponding energy will be delivered. Each layer is further divided into equally sized subvolumes, and using the magnetic scanning in horizontal and vertical directions, each

tumor layer can be scanned with the desired number of particles delivered sequentially to every subvolume. This method offers more flexibility compared to the passive beam delivery since avoids the manufacturing of any patient-specific compensators or collimators, and minimizes the amount of material in the beam path thus reducing primary particle loss and production of secondary particles [Schardt et al., 2010]. On the other hand, this method is more problematic when it comes to treatment of moving tumors, such as lung cancer, due to the interplay between the organ motion and the beam scanning. This may end up in the organs at risk (OAR) or residual tissue receiving the dose that was initially expected to be delivered to the tumor.

1.1.3 Relative biological effectiveness

The damage caused by the radiation to a living cell is mainly determined by its location; the most critical is the damage to the cell nucleus, in particular, the DNA molecules stored inside, which may lead to cell death, mutations, or carcinogenesis. There are two pathways for the DNA damage: the direct ionization of its components or the indirect damage through the hydroxyl groups produced during the water radiolysis in the particle track. The direct damage is more relevant for the high-LET radiation, such as the ion radiation, which has denser tracks than low-LET radiation.

The difference in the biological effects caused by the X-ray radiation compared to ion beams arise from the different microscopic dose distribution, as illustrated in Figure 1.6.

Photons transfer their energy by photoelectric or Compton processes, giving rise to the following ionization events and electron production. However, compared to the charged particle interactions, these processes have low cross sections, leading to small numbers of ionization events. The distribution of photons that has to deposit a relevant dose is random, leading to a homogeneous dose distribution, as illustrated in Figure 1.6, top left. In case of the ion irradiation, the deposited energy is extremely localized along the primary beam trajectory (Figures 1.6, top right and bottom left). The reason for a peaked dose distribution is the low energy distribution of the largest part of emitted electrons, thus traveling at very short distance from the track. The further increase of the ions energies leads to the decrease in their LET and broadening their tracks, increasing the homogeneity of the dose distribution making it resemble the photon dose distribution (Figure 1.6, bottom right).

To quantify the cellular or tissue response to irradiation, the concept of the relative biological effectiveness, or RBE, is used. The RBE of the test radiation, e.g., ion radiation, is defined as a ratio of the absorbed doses of a reference radiation and the test radiation, leading to the same biological effect [Hall and Giaccia, 2006]. Most commonly ^{60}Co γ -rays are taken as a reference radiation [ICRU, 1993], while in many radiobiological experiments, the orthovoltage X-rays serve this purpose.

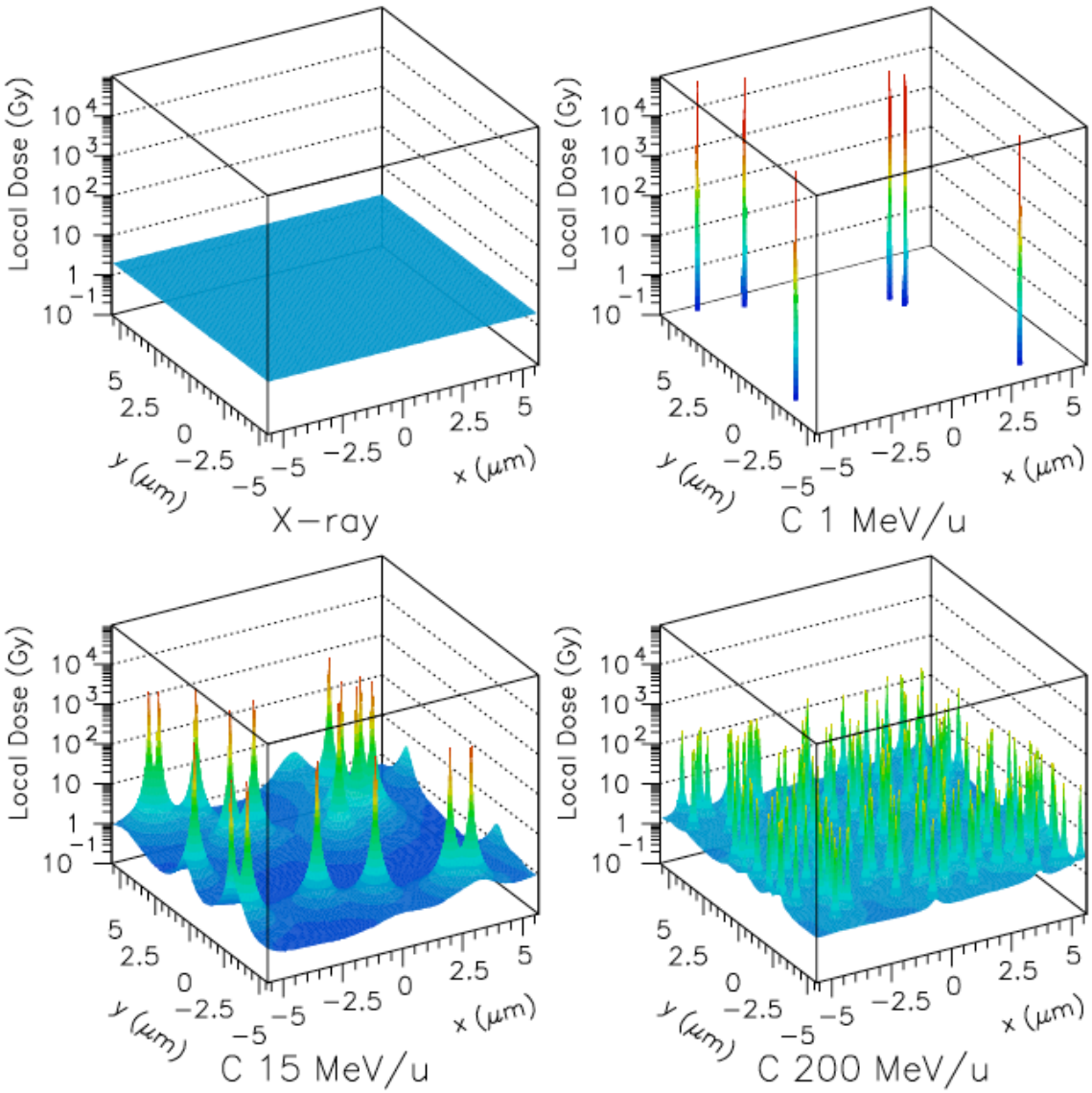

Figure 1.6.: Spatial microscopic dose distribution modeled for the different types of radiation: X-ray (top left) and ^{12}C ions of different energies for the same average microscopic dose of 2 Gy. Figure taken from [Krämer et al., 2003].

A common approach to define the RBE of the radiation of interest is comparing its influence on the cell survival with the one of the conventional photon radiation using the clonogenic survival curves. They describe the relationship between the absorbed dose of radiation and the proportion of cells that remain able to reproduce, i.e., to divide and form colonies after receiving this dose [Hall and Cox, 2010]. An example is shown in Figure 1.7, comparing the survival curves for X-rays and a generic ion radiation. The curves plotted in a logarithmic scale have a characteristic shouldered shape. To describe this behavior, the linear-quadratic (LQ) approach is used, describing the cell survival as the following function of dose:

$$\ln S = -\left(\alpha D + \beta D^2\right), \tag{1.9}$$

with S standing for the cell survival after receiving the dose D. The α (Gy^{-1}) and β (Gy^{-2}) coefficients are the radiobiological cell- or tissue-specific constants, characterizing the initial slope and the curvature of the survival curve, respectively, and their ratio emphasizes the difference between early- and late-responding tissues in response to fractionated treatment [Hall and Cox, 2010]. For densely ionizing radiation, such as neutrons or high-LET ion radiation the survival curves are described only by the α parameter and thus look like a straight line when plotted on the logarithmic scale. It is important to mention that the linear and quadratic contributions to the cell killing are equal at a dose $D = \alpha/\beta$. While the LQ model is good at describing the biological effect at low doses (not higher than $\approx$ 10 Gy), a more advanced approach is required to account for the linear transition of the survival curve shape at a higher dose D_t. This issue can be addressed by switching to the quadratic-linear model (LQ-L) [Astrahan, 2008]:

$$-\ln(S) = \begin{cases} -\left(\alpha D + \beta D^2\right), & D < D_t \\ -\left(\alpha D + \beta D^2 + \gamma(D - D_t)\right), & D \geq D_t \end{cases} \tag{1.10}$$

with γ being is the $\log_e$ cell kill per Gy in the linear part of the survival curve at high doses.

As follows from the shape of the survival curve, the ratio of the ion and X-ray doses, leading to the different survival levels, is different. In the current work, RBE_{10} of the ion beam is calculated as a ratio a dose of X-ray radiation (D_X) to an ion dose (D_{ion}), leading to the 10% cell survival:

$$\mathrm{RBE}_{10} = \left.\frac{D_X}{D_{ion}}\right|_{\mathrm{S}=10\%}. \tag{1.11}$$

Apart from the dependency on the dose or selected survival level, there is a strong dependency on the LET of the particle: the RBE is increasing along the LET range, due to the increasing ionization density leading to more complex damage [Barendsen, 1968; Friedrich et al., 2013b]. However, after a certain LET value, a decrease in the dependency is observed. The reason is that for the more densely radiation the energy becomes 'wasted' since the DNA damage sites

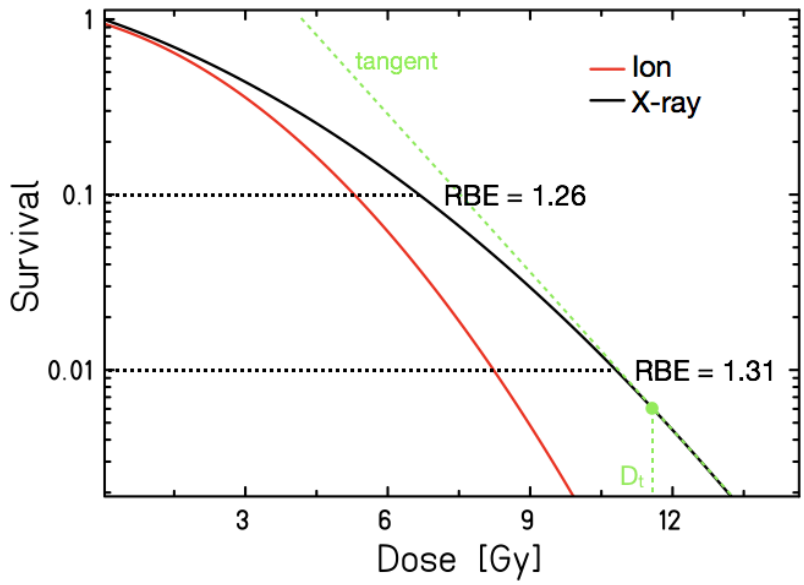

Figure 1.7.: Definition of the relative bilological effectiveness based on the cell survival curves for a given ion radiation (solid red line) and reference X-ray radiation (solid black line). Different RBE values for survival levels of 10% and 1% are shown. Additionally, the transition dose D_t is marked for the X-ray response curve.

are located too close to each other and thus not changing the outcome. This is the so called "overkill" effect. Thus, it has the same efficiency per track but is less efficient per unit dose [Hall and Cox, 2010]. Another experimentally demonstrated dependency [Furusawa et al., 2000], arising from the differences in the energy distribution in the particle track, is the dependency on the ion type: for the heavier ions, the maximum of the RBE-LET dependency is shifting towards higher LET values. Apart from that, one has to keep in mind, that the biological effect is not solely determined by the properties of radiation, but also by the characteristics of the cell line. Irradiation of the cell lines with different repair capabilities might lead to very different RBE-LET dependency behavior [Scholz, 2003].

1.1.4 Local effect model

For the estimation of the final effect of irradiation, the RBE has to be calculated for each position inside the treatment field. One of the approaches for estimating the RBE is using the local effect model (LEM), which is based on the knowledge of particle track structure and the cell or tissue response to conventional photon radiation [Scholz and Kraft, 1996; Friedrich et al., 2013a]. The principal assumption of the initial versions of the model (LEM I-III) was the independence of the biological effect on the type of irradiation. Instead, it depends on the deposited local dose. The cell nucleus was assumed to be the sensitive target, and the biological effectiveness of ion was calculated based on the microscopic local dose distribution pattern of ion traversals within it. The most recent version, LEM IV [Elsässer et al., 2010; Friedrich et al., 2012], assumes the radiation effect to be dependent on the spatial distribution of the DNA damage (essentially the double strand breaks (DSB) distribution) rather than the microscopic

local dose distribution, and a similar DSB distribution leads to a same effect. However, the recent study of [Grün et al., 2012] involving the treatment planning tests with patient data demonstrated that the differences in the predicted absorbed doses leading to the same biological outcome between versions I and IV for typical tumor volumes are less than 10%.

The input parameters for the RBE estimations with LEM IV are the X-ray response parameters α_X, β_X and transitional dose D_t, characterizing the response of the cells to conventional photon radiation according to the LQ-L approach [Scholz et al., 1997; Astrahan, 2008]. These parameters are different for different cell lines or tissues as well as for varying experimental or clinical endpoints.

All the calculations presented in this work were based on the RBE predictions done with LEM IV, despite the LEM I still being used in clinics. The reason for using this version is that it allows handling any type of particle species and energies, as well as for arbitrary α_X/β_X ratio, while the LEM I was benchmarked only for ^{12}C ions and for $\alpha_X/\beta_X \approx 2$ Gy.

1.1.5 TRiP98 treatment planning system

Planning software is an essential tool in treatment planning studies. Today the two 'competitive' types of the treatment planning systems (TPS) for the active beam scanning are being developed. The first one is based on the Monte Carlo (MC) calculations of dose and particle numbers due to their high accuracy and ability to consider emerging secondary radiation and explicit 3-dimensional particle distribution [Grevillot et al., 2012; Mairani et al., 2013; Böhlen et al., 2013], based on GEANT4 [Agostinelli et al., 2003] or FLUKA MC code [Battistoni et al., 2007].

The disadvantages of the MC TPS are their calculation speed, complexity, and maintainability, making them still not completely suitable for the clinical routine. The second TPS type is based on fast analytic dose engines using pencil beam (PB) algorithms and is able to perform dose optimization accounting for radiobiological effects caused by radiation. An example of such TPS is TRiP98 (Treatment Planning for Particles), developed in 1998 [Krämer et al., 2000] to provide the treatment plans for the GSI pilot project with ^{12}C ions and raster scanning technique. Nowadays it serves for research purposes in research centers in Heidelberg, Aarhus, and Lyon and was a prototype for the commercial TPS such as Siemens SynGo/PT or RaySearch. The simple scripting language of TRiP98 allows well documented repeated runs as well as batch communications needed for systematic studies. This section describes the basics of treatment planning with TRiP98, while the more specific details, related to the current work, will be described in the Materials and Methods sections of the following chapters.

The overview of the general structure of the TPS is given in Figure 1.8. As mentioned above, during the active beam scanning procedure the irradiated volume is virtually voxelized, and every point is irradiated by a pencil beam formed by magnetic beam deflection system in the lateral direction. The task of the TRiP98 code is to find an optimum set of accelerator energies to cover the whole depth range and the corresponding particle numbers for each energy and

spot position to achieve the prescribed dose. This procedure is called inverse planning. For the imaging and localization of tumors in addition to other tasks the computed tomography (CT) is used. The morphological information is usually stored in the VOXELPLAN format (developed at the German Cancer Research Center (DKFZ) [Gademann et al., 1993]) and can be converted from the commonly clinically used DICOM format. Recently also functional PET is providing information on intratumor heterogeneity, which is essential for biologically adaptive treatment planning.

The optimization process is performed in two steps. At first, the absorbed dose is considered using input parameters like the number of fields, field weighting, and beam spot size. Second, after an acceptable solution is found, the optimization with respect to the biologically effective dose starts and voxel-specific RBE, and recently also OER values have to be calculated.

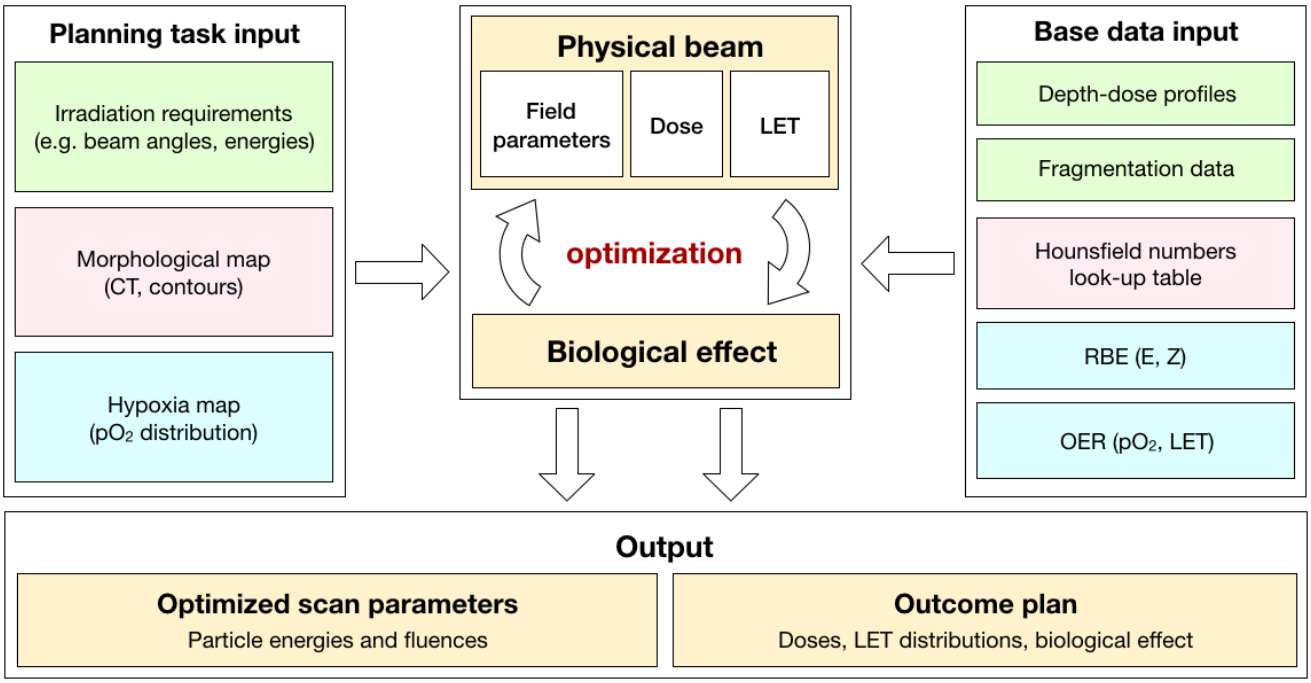

Figure 1.8.: A sketch of the general structure of TRiP98. Z stands for the particle charge and E for its energy. The morphological maps and hypoxia maps are created externally by external diagnostic tools. The base data input is loaded in form of tables.

The optimization is carried out by minimization of the objective function $\chi^2\left(\overrightarrow{N}\right)$ [Krämer et al., 2000; Gemmel et al., 2008]

$$\chi^2\left(\overrightarrow{N}\right) = \sum_{i \in target} \frac{[D_p - D_a^i(\overrightarrow{N})]^2}{\Delta D_p^2} + \sum_{i \in OAR} \frac{[D_{max} - D_a^i(\overrightarrow{N})]^2}{\Delta D_{max}^2} \Theta(D_a^i(\overrightarrow{N}) - D_{max}) = \min \quad (1.12)$$

which is dependent on the number of particles within each raster scanner spot (components of the vector $\overrightarrow{N}$). $\chi^2\left(\overrightarrow{N}\right)$ accounts for the difference between the actual dose D_a^i and the prescribed dose D_p at each voxel i. The second term in the equation, defined by the Heaviside

function, is a 'penalty' added to the function if the maximal allowed dose to the OAR D_{max} is exceeded and can be run through several OAR if needed. D_{max} is defined by the user as a fraction of prescribed dose:

$$D_{max} = MDF \times D_p, \tag{1.13}$$

where MDF stands for maximal dose fraction and is normally defined in the range between 0.3 and 0.8. ΔD_p and ΔD_{max} in equation 1.12 are the adjustable dose tolerance coefficients defining the weights of each two contributions and balancing the tumor coverage and OAR sparing:

$$\Delta D_p = f_w \times D_p \ / \ \upsilon_{w,T} \tag{1.14}$$

$$\Delta D_{max} = f_w \times D_{max} \ / \ \upsilon_{w,OAR}. \tag{1.15}$$

Here, f_w reflects the allowed average deviation of actual dose from its prescribed value and is usually set to 0.025, and $\upsilon_{w,T}$ and $\upsilon_{w,OAR}$ are the weight factors allowing to (de-)emphasize dose deviations for the target or a given OAR, respectively.

Calculations of radiobiological effect are based on LEM IV model described in the previous section. The loaded RBE tables store the data for each particle and its energy as their maximum and intrinsic values, i.e., for single ion traversal. During the total effect calculation all the contributions from the resulting particles in the mixed radiation field have to be considered with appropriate algorithms [Krämer and Scholz, 2006].

To handle different ion modalities, physical base data are necessary. These comprise depth dose profiles and tabulated particle energy spectra as a function of depth, in order to calculate absorbed dose distributions and biological effects accordingly.

The most recent version of TRiP98, the so-called TRiP98-OER [Scifoni et al., 2013; Tinganelli et al., 2015] accounts additionally for the target oxygenation status and requires the additional input of the externally generated hypoxia maps. This way, the effect of the oxygen enhancement ratio is accounted additionally at the step of the biological dose calculation. The problem of the tumor hypoxia is addressed in the next section.

1.2 Tumor hypoxia

1.2.1 Definition and influence on the treatment planning

The condition of tumor hypoxia, leading to its chemo- and radioresistance, invasiveness, the formation of metastases, altered metabolism and genomic instability [Brown, 2007; Wilson and Hay, 2011], refers to the cases of tumors with insufficient molecular oxygen supply due to the uncontrolled oncogene-driven proliferation of cancer cells [Eales et al., 2016]. The effect is caused by the imbalance between the consumption and delivery of molecular oxygen due to the interruptions of the blood flow through the tumor. Two pathways are usually defined (Figure

1.9(a)): the chronic and the acute (cycling) [Hall and Giaccia, 2006; Hoppe-Seyler et al., 2017]. Chronic hypoxia occurs as a result of an increased tumor growth when the blood vessels can not immediately reach the newly formed tumor regions (diffusion problem). The acute hypoxia is usually defined as the result of a temporary occlusion of the blood vessel (perfusion problem).

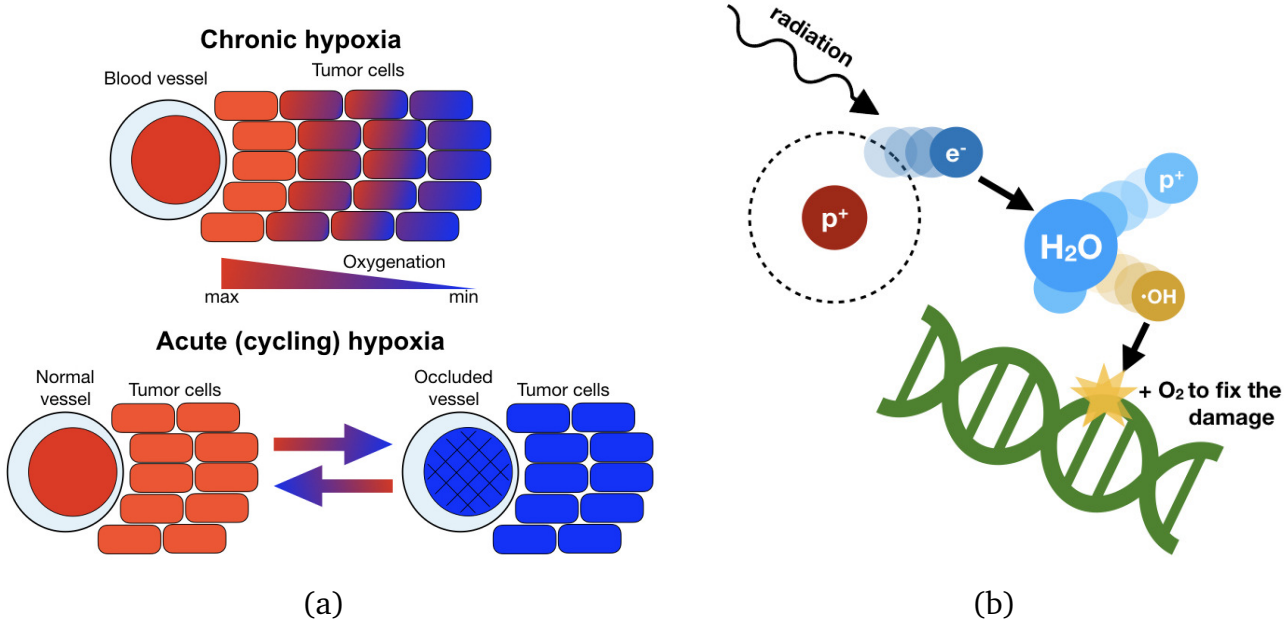

Figure 1.9.: (a) Chronic and acute hypoxia. Chronic hypoxia occurs due to increase distance between tumor blood vessel and tumor cells, resulting in an interrupted oxygen supply. Red: oxygenated tumor cells, blue: hypoxic tumor cells. The acute, or cycling hypoxia happens when the blood vessel gets occluded, e.g., through blood cell aggregates, resulting in the fluctuating cycles of normoxia and hypoxia for surrounded tissues. Adapted from [Hoppe-Seyler et al., 2017]. (b) Oxygen fixation hypothesis: a high energy electron interacts with a water molecule, creating a highly-reactive hydroxyl radical $OH^{\bullet}$. After its interaction with a DNA molecule, it can damage it by producing the $DNA^{\bullet}$. When the molecular oxygen is presented, a peroxy radical is formed ($DNA{-}OO^{\bullet}$), which ′fixes′ the damage into a permanent irreparable state. Adapted from [Grimes and Partridge, 2015] and [Hall and Giaccia, 2006].

Both pathways lead to an increased radioresistance of a tumor. The reason for that, still quite debated in the radiobiological community, but one of the most accredited, is the so-called 'oxygen fixation of damage' phenomenon at the chemical stage of the radiation interaction with matter [von Sonntag, 1987; Hall and Giaccia, 2006; Grimes and Partridge, 2015]. The idea of the oxygen fixation hypothesis is illustrated in Figure 1.9(b). Among the products of an indirect action of radiation with water, the hydroxyl radicals ($R^{\bullet}$) are the main source of the DNA base damage. Normally, this kind of radical damage can be chemically repaired. However, the presence of the molecular oxygen (O_2) may lead to the formation of peroxyl radicals, $RO_2^{\bullet}$. The damage caused by these type of radicals is much higher and almost impossible to for the cell

to repair. Thus, under hypoxia, the indirect damage can be mainly restored, but in the presence of molecular oxygen it will be likely made permanent, or 'fixed'.

In order to quantitatively estimate the dosimetric effect of hypoxia, the concept of oxygen enhancement ratio (OER) is used, which is defined as a ratio of doses applied to normal and hypoxic regions respectively, resulting in the same radiobiological effect (e.g. cell survival):

$$\mathrm{OER}_S = \left.\frac{D(p\mathrm{O}_2)}{D_{normoxic}}\right|_S, \tag{1.16}$$

where $D(p\mathrm{O}_2)$ and $D_{normoxic}$ are the doses at a given oxygen concentration (or partial oxygen pressure) and in the normoxic (partial oxygen pressure $p\mathrm{O}_2 = 21\%$) condition, accordingly, resulting in the same cell survival fraction S in the target.

Ion beam therapy is considered as an effective solution for tackling the problem of hypoxia. Experimental studies of [Furusawa et al., 2000] showed the decrease of OER down to almost 1 for LET values of several hundreds keV/μm. The explanations for this effect are based on the particle track structure [Alper and Bryant, 1974]. The high-LET particles have denser ionization tracks, which increase the chances for radicals to interact between themselves. At the same time, the chance of producing molecular oxygen in the track region is increased as well.

The decrease of OER values with increasing LET of the particle is described by the model studies of [Wenzl and Wilkens, 2011; Stewart et al., 2011; Scifoni et al., 2013; Antonovic, 2014]. The key conclusion of all of them is that with the increase of the LET, depending on the oxygen concentration in the region, one would expect a significant reduction (up to 2-3 times) of dose, that has to be delivered to a tumor.

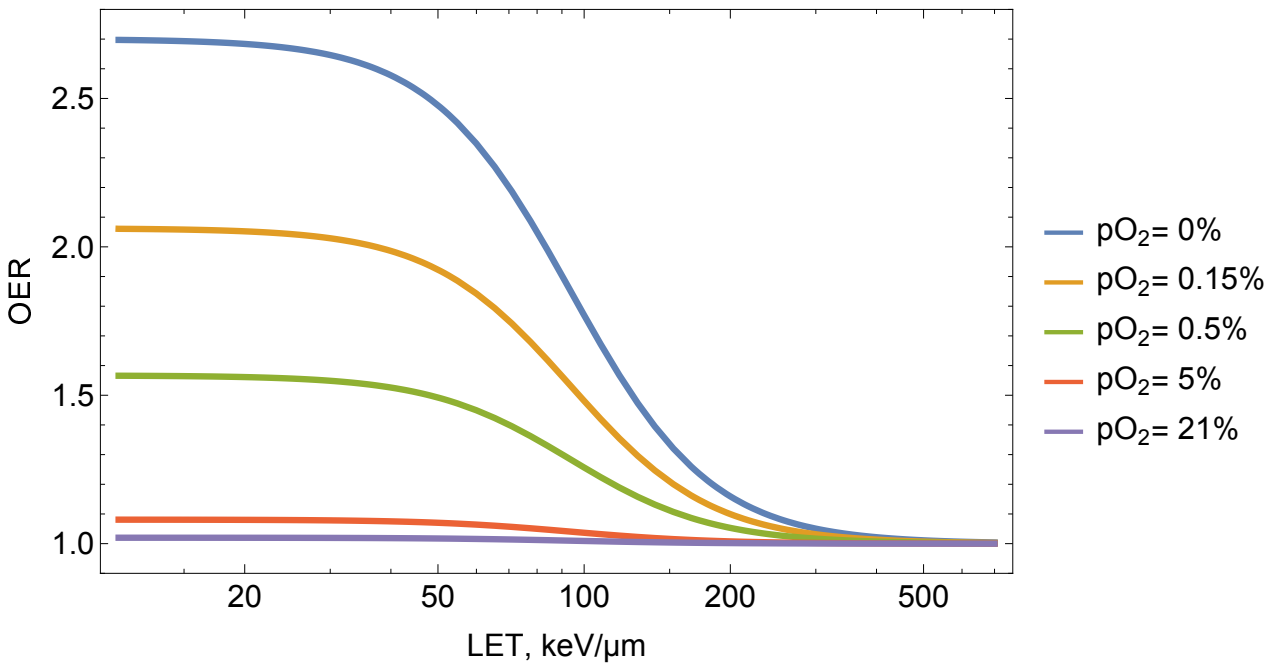

Figure 1.10.: OER dependency on several values of partial oxygen pressure ($p\mathrm{O}_2$) and the LET of the particle. Lines represent the model cuts from [Tinganelli et al., 2015].

Figure 1.10 shows the model cuts of the semi-empirical model developed earlier at GSI [Scifoni et al., 2013; Tinganelli et al., 2015], which describes the dependence of OER on the tissue oxygenation level and the LET of the particle as

$$OER\left(pO_2, \overline{LET}\right) = \frac{b\left(Ma + \overline{LET}^{\gamma}\right) / \left(a + \overline{LET}^{\gamma}\right) + pO_2}{b + pO_2}, \tag{1.17}$$

with pO_2 standing for the partial oxygen pressure, $\overline{\text{LET}}$ - for the dose-averaged LET, and b, a, γ, and M being semi-empirical parameters set to 0.25%, 8.27× 10^5, 3, and 2.7 for CHO cell line, respectively. As follows from the model, the reduction of OER by a factor of 2 happens at LET values of around 100 keV/μm almost independently on the target oxygenation. Thus, especially for the highly hypoxic regions, applying the high-LET beams allow a significant reduction of the delivered dose.

1.2.2 Hypoxia imaging

Since the presence of hypoxia can change the treatment outcome, possession of a reliable tool for its visualization is crucial. The ideal tool for imaging hypoxia is expected to be non-invasive, applicable to any tumor cite, amenable to repeated measures, able to distinguish the perfusion- and diffusion-related hypoxia, non-toxic and simple to perform. Nowadays numerous approaches to determine the oxygenation of the tissues are suggested, among them are:

- Positron emission tomography imaging, in particular, ^{18}F fluoromisonidazole PET (FMISO-PET), which is nowadays the most dominating among all the proposed strategies. It is a non-invasive method based on the determination of the fluoromisonidazole uptake, acting as a tracer, by the tissues [Cheney et al., 2014b; Eschmann et al., 2005]. Initially the nitroimidazole compounds were developed for radiosensitizing hypoxic cells. They have a nitro group (NO_2), which under hypoxia can undergo a reduction to the amino group (NH_2), producing the intermediate highly reactive products that will bind to the macromolecules inside the cell. Labeling the nitroimidazole with ^{18}F allows one to identify the bound product and thus the presence of hypoxia with PET [Horsman et al., 2012]. Nowadays this method is considered to be the most promising; however, the problem of interpretation of the uptake data is still not completely solved [Toma-Daşu et al., 2009; Mena-Romano et al., 2015].
- Oxygen-enhanced Magnetic Resonance Imaging (MRI) [O'Connor et al., 2016], which can be also promising since proton MRI is already actively used in the clinical routine. The method is based on the sensitivity of the MRI longitudinal relaxation rate to changes in the level of molecular oxygen dissolved in blood. In normoxia, hemoglobin molecules in erythrocytes are saturated with oxygen and form oxyhemoglobin. Inhaling a gas with an increased proportion of oxygen will not affect the proportion of oxyhemoglobin in blood, but will alter only the amount of dissolved molecular oxygen in plasma. This will increase

the tissue longitudinal relaxation rate, which is can be detected with MRI. In contrast, inhalation of hyperoxic gas in hypoxia will lead to the formation of more oxyhemoglobin molecules but almost with no impact on O_2 amount in plasma, thus causing almost no changes to the relaxation rate.

- Eppendorf oxygen electrode [Brizel et al., 1996], which, despite being a precise method, is invasive, applicable only for the easily accessible tumors and requires considerable operator skills.
- Perfusion estimation with PET using ^{15}O-labeled water or with CT [Ng et al., 2009], which allows identifying fluctuating hypoxia, however, do not give a complete picture of hypoxia distribution.
- Identification of oxygen-responsive signaling mechanisms mediating the cellular responses to hypoxia.

The latter two methods, despite being also quite promising, face a range of challenges. Among them are the issue of penetration to cells distant from blood vessels and their toxicity.

2 Experimental analysis of physical and radiobiological properties of oxygen beams

2.1 Introduction

The precise calculation of the delivered physical and RBE-weighted dose at any given target spot requires the knowledge of the main beam properties. The basic input data required for treatment planning with TRiP98 implies the knowledge of the beam depth-dose distribution, fragment spectra, as well as its radiobiological properties and the behavior in hypoxic conditions (where the ^{16}O beams are mainly planned to be applied).

The current status of the beam model for ^{16}O, based on the data for the underlying ions and the recent measurements carried out earlier at GSI, was accessed through measuring the beam-eye view and lateral dose profiles for an extended target irradiation. The radiobiological measurements included an extensive series of RBE measurements for the CHO-K1 cell line, determination of the oxygen enhancement ratio and the subsequent verification in hypoxia implying the extended target irradiation.

The material presented in this chapter was published in [Sokol et al., 2017].

2.2 Materials and methods

2.2.1 Treatment planning

The general structure of the TRiP98 TPS was already described in the previous chapter. In this section, all the treatment plans used for irradiations, radiobiological estimations and comparative studies were generated using TRiP98 in the proof-of-concept version including the OER dose weighting [Scifoni et al., 2013]. In this version, the optimization is performed employing the kill-painting approach, where the optimized quantity is no longer the RBE-weighted dose, but a desired uniform survival level in the target. Thus, apart from the RBE, the system accounts additionally for tumor oxygenation by including the OER values in the calculation of the biological effects, both in forward and inverse planning. This way, the resulting calculated biological dose is RBE- and OER-weighted.

According to the low-dose approximation, introduced by [Krämer and Scholz, 2006], the RBE-weighted dose can be calculated as

$$D^{i}_{bio}(\overrightarrow{N}) = \sqrt{\frac{\overline{\alpha}_i \cdot \left(\overrightarrow{c}^{T}_{i} \cdot \overrightarrow{N}\right) + \overline{\beta}_i \cdot \left(\overrightarrow{c}^{T}_{i} \cdot \overrightarrow{N}\right)^2}{\beta_x} + \left(\frac{\alpha_x}{2\beta_x}\right)^2} - \frac{\alpha_x}{2\beta_x} \tag{2.1}$$

where α_x and β_x describe the response to photon irradiation, $\overline{\alpha}_i$ and $\overline{\beta}_i$ describe the response to ion irradiation after dose averaging in the mixed field at voxel i. $\overrightarrow{c}^{T}_{i}$ is the corresponding row of the dose correlation matrix, characterizing the contribution of raster spots to a given voxel [Krämer and Durante, 2010].

In order to introduce the OER as a dose-modifying factor, the ion response parameters had to be modified as follows [Scifoni et al., 2013]:

$$\overline{\alpha}'_i\left(\overline{\mathrm{LET}}_i, p\mathrm{O}_{2,i}\right) = \overline{\alpha}_i \,/\, \overline{OER}\left(\overline{\mathrm{LET}}_i, p\mathrm{O}_{2,i}\right) \tag{2.2}$$

$$\overline{\beta}'_i\left(\overline{\mathrm{LET}}_i, p\mathrm{O}_{2,i}\right) = \overline{\beta}_i \,/\, \overline{OER}^2\left(\overline{\mathrm{LET}}_i, p\mathrm{O}_{2,i}\right) \tag{2.3}$$

For enabling the dose calculation with ^{16}O beams, the standard transport model was updated with the recent primary ^{16}O beam attenuation measurements (courtesy of G. Martino, GSI) and the fragmentation data available for the lighter ions.

Since all the experiments were carried out using the CHO cell line, the LEM IV RBE tables for it were produced based on the corresponding measured X-ray response data (see Appendix A).

2.2.1.1 Physical dose verification for extended target irradiation

For the physical dose verification experiments, an extended water target of 60 × 40 × 60 mm centered at 82 mm in depth inside the water cube of 100 × 150 × 166 mm was emulated. Two types of optimization were performed:

- physical (**phys**) - optimization for a uniform physical dose of 4 Gy;
- biological (**bio**) - optimization for a uniform RBE-weighted dose of 6.5 Gy for CHO cell line.

The optimization was performed applying the plain gradient optimization algorithm [Schmidt, 2005; Krämer et al., 2000]. For the RBE-weighted dose calculation, the low-dose approach was used [Krämer and Scholz, 2006]. The following scanner/beam parameters were considered:

- Nominal focus value for the beam spot (FWHM): 7 mm;
- Approximate spacing between subsequent peak positions (scanner stepsize in depth): 3 mm;
- Raster stepsize in x- and y-directions: 3 mm.

2.2.1.2 Expected survival estimation

For each dose sample related to a particular survival curve, a separate plan was produced. The field size was defined by the dimensions of a vessel used for culturing the cells (see the following section).

The monoenergetic beams of 3, 146 and 280 MeV/u (with corresponding LET values of 670, 38 and 23 keV/μm) are available at UNILAC and HIT, respectively. For them, the cell curvival was estimated in the beam entrance channel. To collect the survival data for the intermediate LET values of 83 and 166 keV/μm, which are not available at any of these facilities, additional experiments were conducted in an "extended" Bragg peak of 1 cm. This approach requires to perform the survival calculations not for the pure LET values, but rather for the dose-averaged LET values, defined as

$$\overline{\mathrm{LET}} = \langle \mathrm{LET} \rangle_D = \frac{\sum_i \mathrm{LET}_i \, D_i}{\sum_i D_i} = \frac{\sum_i \mathrm{LET}_i^2 \, F_i}{\sum_i \mathrm{LET}_i \, F_i} \tag{2.4}$$

with D_i dose and F_i fluence of the radiation component i.

The "extended" peak was modeled as a superposition of peaks created by the beams with five selected energies. The shallower region in the resulting dose-averaged LET depth distribution was chosen, to have some safety margins in measurements, related to the positioning of the sample. The expected survival values were calculated at the selected position. The example of the approach for the LET of 166 keV/μm is displayed in Figure 2.2.1.2.

For the estimation of the survival levels for the experiments with extended target irradiation, the position of each cell sample in the treatment plan was calculated based on the knowledge of the water equivalents of the setups' materials. The corresponding data is provided in Appendix B.

2.2.1.3 Hypoxia distribution modeling

To estimate the survival for the experiment in hypoxia presented in this chapter, an unevenly oxygenated symmetric target geometry was emulated. Its size and the corresponding sizes of hypoxic subvolumes were modeled according to the real sizes of the used cell culture vessels. The total size of the simulated volume was 40 × 40 × 160 mm in water equivalent (WEQ) and the target was centered at 80 mm depth (WEQ). By superimposing several phantom configurations the following symmetric pO_2 distribution along the beam direction z was emulated: 20% for $z < 62$ mm and $z > 98$ mm, 0.5% for $62 \leq z < 74$ mm and $86 < z \leq 98$ mm, and 0% for $74 \leq z \leq 86$ mm. These values of oxygenation were then used directly for the estimation of the OER and dose calculations.

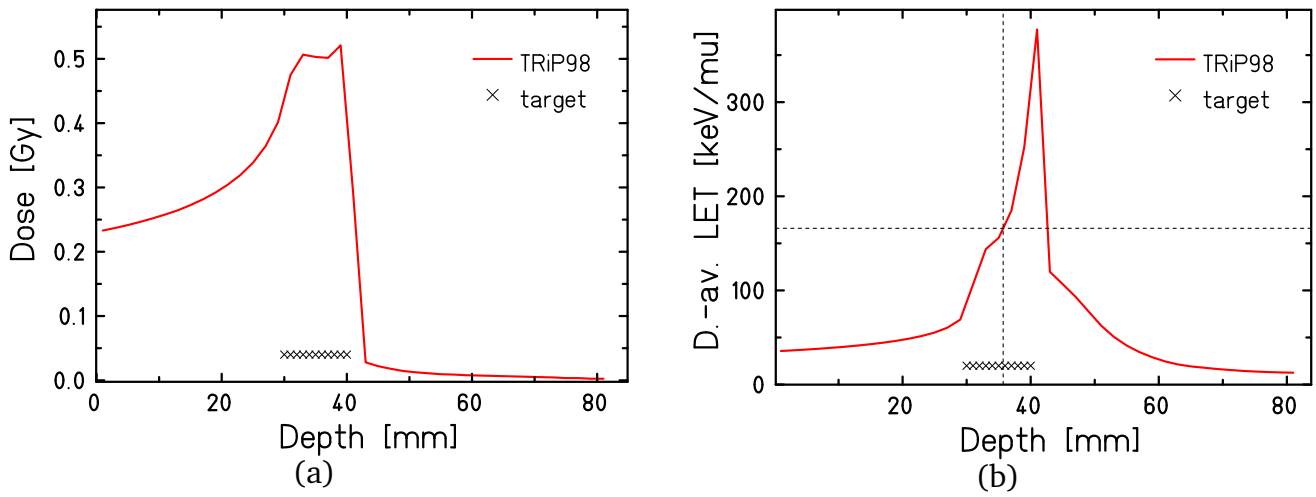

Figure 2.1.: Example of dose-averaged LET estimation for a particular position inside the extended Bragg peak of 1 cm. The Bragg peak corresponding to the dose of 0.5 Gy in Figure (a) is a superposition of five peaks generated by beams with energies of 145.88, 150.24, 154.58, 158.78, 162.93 MeV/u. The corresponding dose-averaged LET profile is shown in Figure (b). A relatively shallow position in the target region (dashed lines) is chosen, and the corresponding dose-averaged LET (166 keV/μm) and depth values are defined for further survival estimation.

2.2.2 Irradiation systems

3D physical dose verification, all the hypoxic irradiations, and part of the RBE measurements were carried out in the experimental 'quality assurance' (QA) room at HIT. A pool of monoenergetic oxygen beams is available there [Kurz et al., 2012], with energies ranging from 103.77 up to 430 MeV/u, all of them delivered using a 3D intensity-controlled raster scanning system. To assure the high accuracy of the dose delivery, prior to the start of irradiation procedure, the calibration of the dose with the Farmer chamber has to be carried out. More information on the procedure at HIT is given in Appendix C.

For the survival measurements at a given dose-averaged LET ($\overline{\text{LET}}$) of 166 keV/μm and 83 keV/μm cell monolayers were placed in the middle of a 3D oxygen ion plan covering a depth of 10 mm at a water equivalent depth of 35 mm, which was adjusted using a 30 mm or 25 mm acrylic glass (PMMA) bolus, accordingly. For measuring the survival for LET = 38 keV/μm and 23 keV/μm, cells were irradiated with monoenergetic beams with energies of 146 and 280 MeV/u on target, respectively.

Radiobiological measurements for the energy of 3 MeV/u on target, corresponding to the LET value of $\approx$ 670 keV/μm, were carried out at the Universal Linear Accelerator (UNILAC) at GSI. The details on a specialized setup for this measurement are given below.

All the accompanying reference X-ray irradiations were performed at GSI with the Isovolt DS1 X-ray machine (Seifert, Ahrensberg, Germany) at a dose rate of 2 Gy/min and a peak voltage of 250 kV.

2.2.3 3D absorbed dose measurements

Measurements of the absorbed dose distribution were performed inside a water phantom (MP3-P, PTW, Germany) using a set of pinpoint ionization chambers. Each chamber has a diameter of 2.9 mm and a sensitive volume of 0.03 cm^3. They are arranged in 6 staggered rows of 4 chambers, and the construction can be moved along x- and y-directions to achieve a higher spatial resolution up to 0.1 mm (refer to [Karger et al., 1999] for more details). The scheme of the configuration is shown in Figure 2.2.

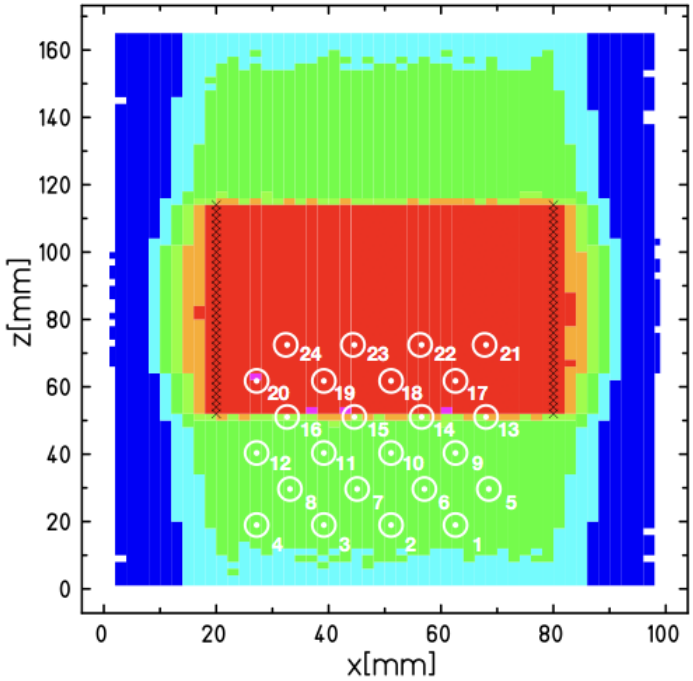

Figure 2.2.: An example of the projection of the three-dimensional arrangement of 24 pin point chambers for measuring the absorbed dose distribution onto the (*x*,*z*) plane. The first and last two lines along z are staggered ±6 mm in y-direction.

2.2.4 Biological measurements

2.2.4.1 General procedure

The Chinese hamster ovary (CHO-K1) cell line was selected for the irradiation due to its stability and a short doubling time. The biological effects were accessed and quantified using a clonogenic (colony forming) assay. Twenty-four hours prior to irradiation, cells were seeded in monolayers with a concentration of $\approx 5 \times 10^4$ cells per sample. After the irradiation, approximately 100 cells able to divide (clonogenically active) were re-seeded per T-25 (Falcon) tissue culture flask (TCF) in 5 ml of medium (Ham's F12 supplemented with 10% Fetal Bovine Serum superior and 1% penicillin-streptomycin, Biochrom GmbH). To minimize the seeding error, for each irradiated sample 3 corresponding TCF (triplicates) were prepared. After that, cells were

incubated for seven days at 37 °C in a humidified atmosphere of 5 to 10% CO_2 in air, then stained with 1% methylene blue staining solution. Colonies containing more than 50 cells were considered as survived and counted.

Depending on the experiment, irradiations were performed with three types of cell culture vessels: T-25 flasks, Petri dishes, and specially designed rings [Tinganelli et al., 2013]. It was previously demonstrated that these vessels could be used consistently for biological effect measurements [Tinganelli et al., 2015]. The first two vessels were used for the survival measurements in normoxic conditions. The details on the irradiation in hypoxia are given below.

2.2.4.2 Irradiation at UNILAC

For ^{16}O ions with an energy of 3 MeV/u, the continuous slowing down approximation (CSDA) range in water is expected to be ≈ 56 micron (estimated using LISE++ software [Tarasov and Bazin, 2008]). This means that standard closed vessels, such as TCF, Petri dishes or well plates are not applicable for irradiation with the low-energy particles since the beam will be absorbed in the material. To overcome this issue, a particular setup is used at the UNILAC. It allows irradiating the cell monolayers in open Petri dishes stored inside a special chamber. With the help of a robotic system, the desired sample can be extracted from the magazine and placed in front of the beam exit window. This method allows minimizing the beam energy losses, since the only remaining material in the beam path are the 28 mm air gap and the 20 μm thin medium film covering the cell monolayer. More details on the UNILAC irradiation procedure can be found in [Kraft-Weyrather et al., 1989].

2.2.4.3 Irradiation in hypoxic conditions

For irradiating the cell monolayers in hypoxic conditions, GSI uses a specially designed and patented [von Neubeck, 2006] combination of rings and chambers. The cells are cultivated onto the hydrophilic side of a round piece of 25 μm thick gas permeable foil (biofolie 25 from Greiner Bio One) equal to 47 μm water-equivalent (WEQ) thickness. The cell growth area size is 4.52 cm^2. The foil is attached to a ring made out of polyvinyl-chloride, which is then filled with the 3 mm thick layer of growth medium and closed with a similar foil on the other side. After that, the rings are kept into the dedicated hypoxic chamber (HC), in the quantities of one (single HC), or three (triple HC). The photo of a single HC is shown in Figure 2.3. For reaching the desired gas concentration, the chambers have to be flushed with the required gas mixture for ≈ 2 hours. The details of this procedure are reported in [Schicker et al., 2009] and [Tinganelli et al., 2013]).

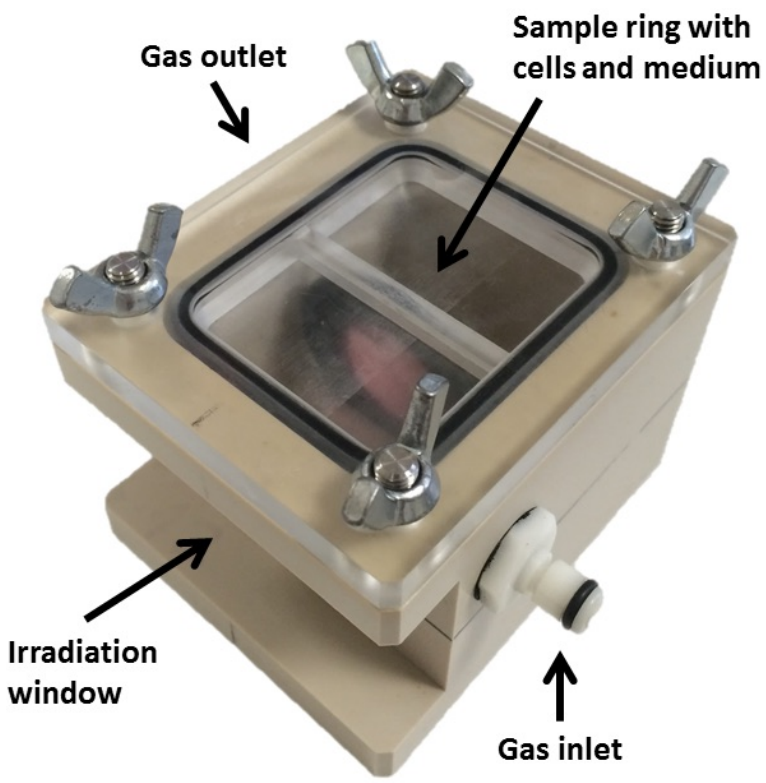

Figure 2.3.: Photo of a single chamber (HC) used for irradiating cells at the desired level of pO_2. The ring sample containing the foil with the cell monolayer is fixed inside, and the chamber is closed with a special lid preventing the gas exchange with the environment. Via the gas inlet and outlet, the chamber can be connected to the gas source, and a constant gas mixture flow can be provided. For a single HC, the wall on one side is thinner, and this side is normally used for irradiation to minimize the beam loss and fragmentation in the wall material. In case of a symmetric triple HC, which is usually used for the extended target irradiation, the walls are of equal thickness.

2.2.4.4 Extended hypoxic target irradiation

For testing the kill-painting approach for the treatment of hypoxic targets [Scifoni et al., 2013; Tinganelli et al., 2015], modeling of an extended unevenly oxygenated target is needed. To emulate a target with a hypoxic region in the center, a combined setup consisting of TCFs and a triple HC was assembled, similar to the one described in [Tinganelli et al., 2015]. The scheme of the phantom is shown in Figure 2.4(a). The entrance channel and target parts with normal oxygenation level are imitated by the TCFs, and the triple HCs, gassed to the desired oxygen concentrations (0.5% or 0% pO_2), imitated the hypoxic regions. For increasing the spatial resolution of the measurements, additional range shift was created by adding TCFs filled with water and the polystyrene blocks to the setup, keeping the same overall WEQ length of the phantom. The water equivalents of the materials used are presented in Appendix B. In total, five different configurations of the phantom, each in two repetitions, were irradiated.

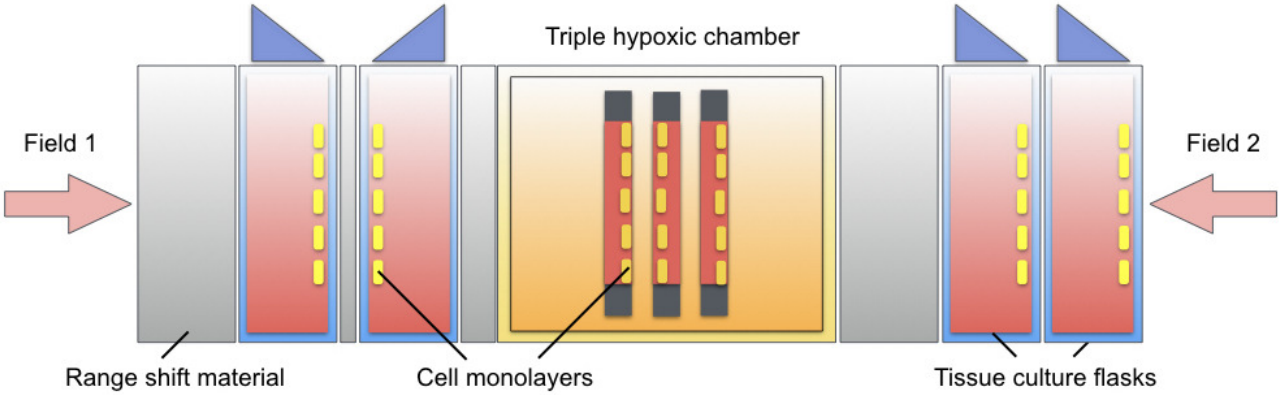

(a)

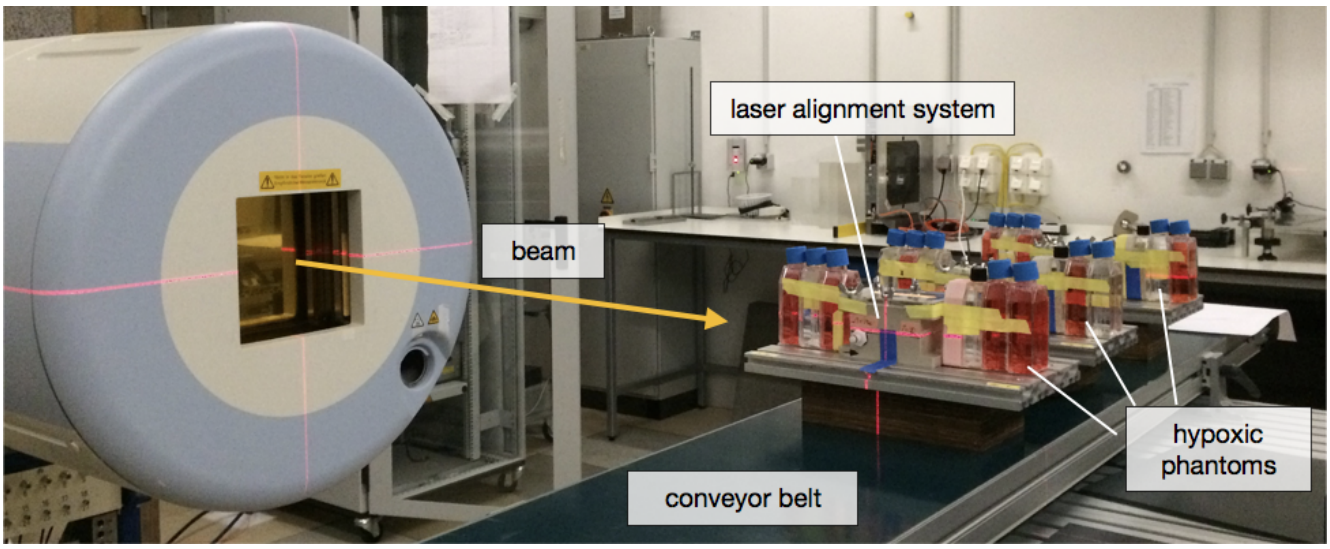

(b)

Figure 2.4.: (a) A sketch of the phantom setup imitating the target with uneven oxygenation, consisting of the triple hypoxic chamber and differently oriented tissue culture flasks. Arrows mark the direction of the fields during the irradiation. (b) A photo of the QA cave of HIT facility with three hypoxic phantoms positioned in front of the beam exit window.

2.3 Results and discussion

2.3.1 Physical dose verification

The result of the verification of the beam's eye view depth-dose profiles for a target of 60 × 40 × 40 mm centered at a depth of 82 mm in water are shown in Figure 2.5. The circles represent the average and the standard error (± SEM) of the two central pinpoint chambers of each row of the configuration, described above. These errors are of an order of 1-3% and are smaller than the data symbols. The numerical data for each point is given in Appendix D.

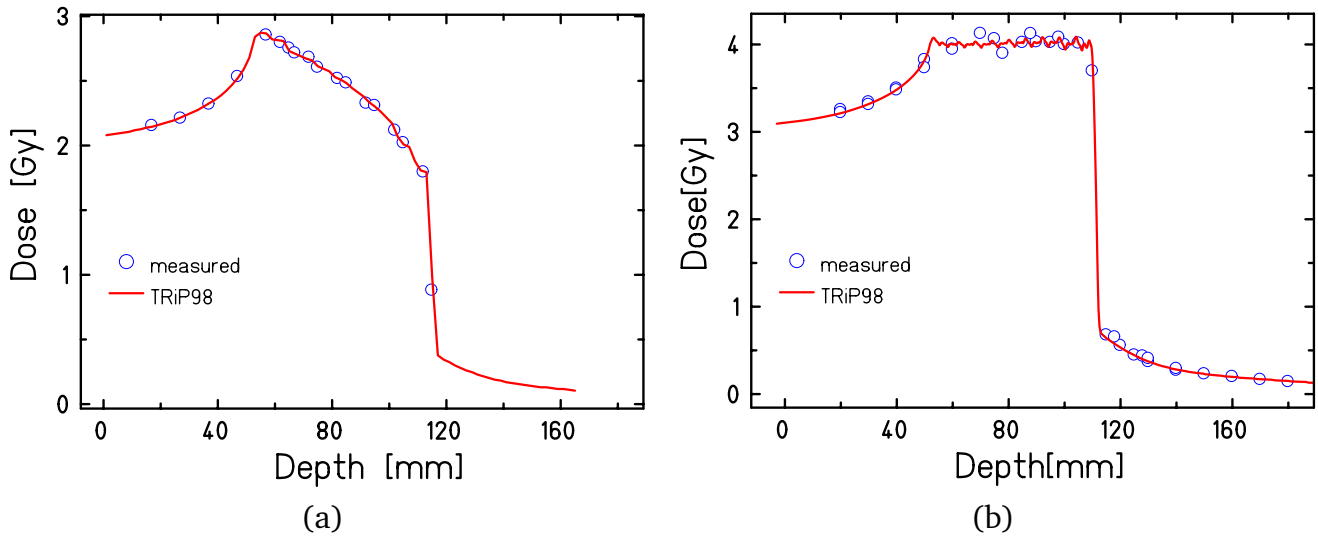

Figure 2.5.: Verification of the absorbed dose in beam-eye view direction for a target volume at 82 mm depth, covering a depth range of 60 mm. Plan is optimized for a (a) flat RBE-weighted dose of 6.5 Gy (b) flat physical dose of 4 Gy. Circles correspond to single pinpoint measurements, the line represents the TRiP98 prediction. The error bars, representing the standard error (± SEM) of the two central pinpoint chambers of each setup row, are smaller than the symbol size, thus cannot be distinguished.

For the absorbed dose profile presented in Figure 2.5(a) the treatment plan was optimized for a uniform RBE-weighted (biological) target dose of 6.5 Gy. Since the dose-averaged LET distribution is increasing towards the end of the beam range, the RBE distribution in depth is increasing. Thus, to achieve a flat RBE-weighted dose profile, the absorbed dose profile has to be decreasing towards the distal edge of the target. The difference between the calculated and the measured dose is ≈ 1.3% in the entrance channel and ≈ 2.5% in the target region. For this experiment, the dose in the fragmentation tail was not verified.

Figure 2.5(b) demonstrates the verification of a dose profile for a plan optimized for a prescribed uniform absorbed (physical) dose of 4 Gy. The overall difference between the measured data and the TRiP prediction is the following: ≈ 1.5% in the entrance channel, ≈ 3.3% in the target and ≈ 9.2% at the distal fall-off. The presented data were collected over several indepen-

dent experiments separated by several weeks, and the slight change in experimental conditions can be the reason for an intrinsic measured dose fluctuation of around 5% in the target region.

For the treatment plan optimized for a uniform absorbed dose the additional analysis of the lateral dose profiles at different depths was carried out. Four positions, corresponding to the entrance channel (19.7 mm depth in water), the front part of the target (59.7 mm depth in water), the distal part of the target (89.7 mm depth in water) and the fragmentation tail (129.7 mm depth in water) were chosen. The corresponding lateral profiles for the absorbed dose are shown in Figure 2.6. In contrast to the previous measurements, each point is an independent measurement of a single pinpoint chamber. In this case, the measured dose errors can be estimated in a similar way as in [Schwaab et al., 2011] as

$$\delta D_i = \sqrt{D_i}/100 \tag{2.5}$$

where D_i is the value of the dose in Gy measured by the chamber.

The positioning error of the chambers in the horizontal direction is defined by their diameter and the sensitive volume, which in case of the chambers of type TM31015 [PTW, 2017] with a sensitive volume of 30 mm^3 and an inner radius of 2.9 mm, is not expected to exceed the value of ≈0.8 mm.

Although there is a good agreement with the TRiP calculation for the first two positions, the discrepancy is slightly increasing with depth. In the region of the fragmentation tail, the dose at the edges of the target volume is slightly underestimated. It needs to be further investigated whether any beam components were not considered correctly in the calculation, or if it is induced by experimental conditions.

2.3.2 Relative biological effectiveness

The level of the knowledge of the RBE values of oxygen beams at the moment of the start of the current work could be described as poor. In 2013 the available RBE data for all the beams were summarized by [Friedrich et al., 2013b] as a Particle Irradiation Data Ensemble (PIDE). Here, twelve values of RBE_{10} for ^{16}O beams are cited, with six values for CHO cell line [Scholz et al., 1997; Scholz, 2003], four for V79 [Wulf et al., 1985], and one for C3H10T1/2 [Miller et al., 1995], and M3-1 [Todd, 1975]. Thus, these data at the moment of the start of the current project was more than ten years old. One additional value of RBE for the V79 cell line was published in [Pathak et al., 2007], but not included to the PIDE. Regarding the CHO data, the mentioned RBE values were calculated by [Friedrich et al., 2013b] based on the survival data obtained using the procedure of plot digitalization since no numerical data was published in the respective references.

In recent years, several more works reporting the RBE of ^{16}O were published. In particular, these are the works of [Tinganelli et al., 2013] who measured the effect of 140 keV/μm ^{16}O on the CHO cells while investigating the influence of hypoxia; [Habermehl et al., 2014] reported

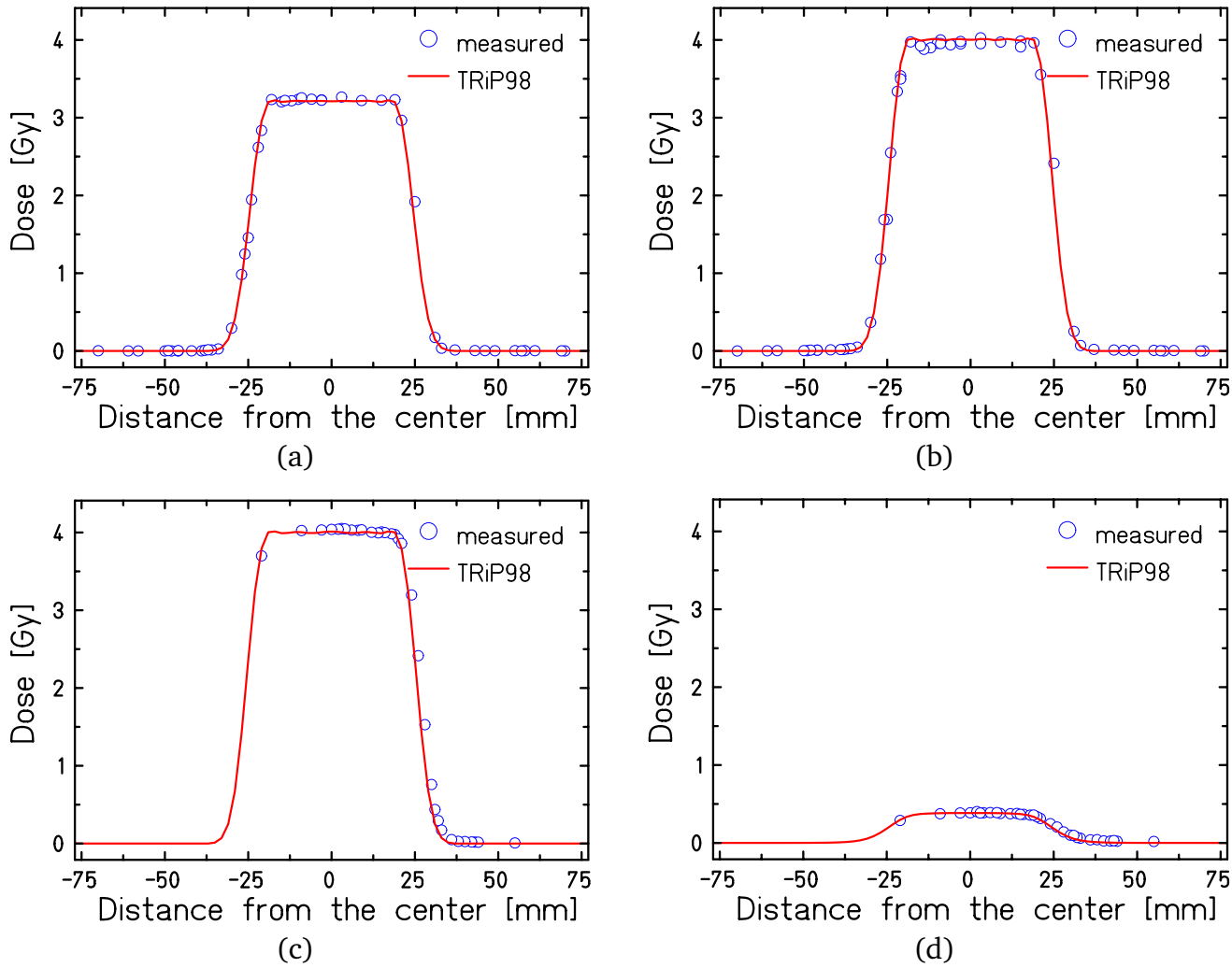

Figure 2.6.: Verification of the absorbed dose in the lateral direction at depths of (a) 19.7 mm, (b) 59.7 mm, (c) 89.7 mm and (d) 129.7 mm. Circles correspond to the pinpoint measurements, and the lines represent the TRiP98 predictions. The error bars, representing the intrinsic dose measurements errors, and the positioning uncertainties in horizontal direction, are smaller than the symbol size, thus cannot be distinguished.

measurements for HEPG2, HEP3B, HUH7, and PLC cell lines, [Dokic et al., 2016] presented one RBE value for a human alveolar adenocarcinoma cell line. However, based only on these data, for none of the mentioned cell lines it is possible to estimate the behavior of the RBE-LET dependency since not the entire energy range was covered.

Since the CHO-K1 cell line remains the most described cell line regarding the ^{16}O RBE and is one of the easiest cell lines in terms of handling, it was selected for performing the additional survival measurements in order to verify the existing RBE_{10} values and to expand the dataset for other LET values. The resulting pool of the corresponding survival curves including the measured values and the fitted curves is shown in Figure 2.7 and the numerical data are given in Appendix E. The X-ray measurements used for the further RBE estimations are shown in black. As mentioned above in the Materials and Methods section, the measurements for the

'reconstructed' energies of 19.6 and 46.8 MeV/u correspond to the extended target irradiations with $\overline{\text{LET}}$ = 166 keV/μm and 83 keV/μm, respectively.

Based on these measurements, the RBE_{10} were calculated as described in the previous chapter. Using the LQ approach, the equation 1.11 can be rewritten as

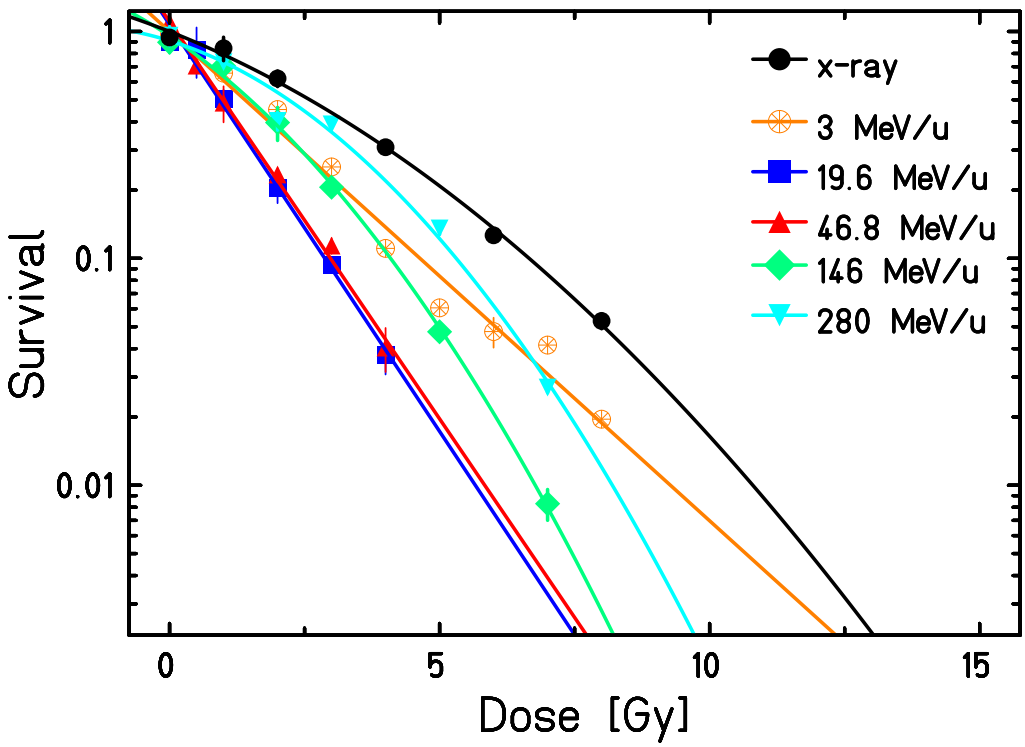

Figure 2.7.: Survival fraction of the CHO-K1 cell line as a function of dose for ^{16}O beams of different residual energies. The reference X-ray is presented in black. The symbols and the error bars represent the average ± SEM of two (for the energies of 3, 146 and 280 MeV/u) or three (for the energies of 19.6 and 46.8 MeV/u) independent repetitions. Lines represent the fit of data. For the energies of 3, 19.6, and 46.8 MeV/u a linear fit was applied; the curves for 146, 280 MeV/u, and the X-ray curve were fitted using a linear-quadratic equation.

$$\text{RBE}_{10} = \frac{\beta_{ion}}{\beta_X} \cdot \frac{\alpha_X + \sqrt{\alpha_X^2 - 4\beta_X \ln(0.1)}}{\alpha_{ion} + \sqrt{\alpha_{ion}^2 - 4\beta_{ion} \ln(0.1)}} \tag{2.6}$$

where α_{ion} and β_{ion} are the LQ parameters for a given ion survival curve, and α_X and β_X are the LQ X-ray parameters. This calculation is applicable for the energies of 146 and 280 MeV/u; for the energies of 3, 19.6 and 46.8, where the survival is described as $\ln S = -\alpha D$, the equation 1.11 transforms into the ratio of the α parameters of the corresponding curves:

$$\text{RBE}_{10} = \frac{\alpha_{ion}}{\alpha_X}. \tag{2.7}$$

The resulting values of the RBE_{10} are summarized in Table 2.1. The corresponding error δRBE_{10} was estimated based on the fitting errors for the corresponding α and β values for the survival curves. According to the general trend observed for the RBE data in [Friedrich et al., 2013b], the maximum of the RBE-LET dependency is expected to be established in the LET range of 100-400 keV/μm, and the measured data follows this trend. However, more precise estimation of the position of this maximum is not possible since at HIT and GSI no corresponding monoenergetic beams with the energies in the range of $\approx$ 10-40 MeV/u were available at the moment. Based on the statistics from the same work [Friedrich et al., 2013b], the maximal values of the RBE are expected to be in the range of 2-4; the maximal value observed in this work is 2.285±0.211 for the $\overline{LET}$=166 keV/μm. However, it was measured for an extended target of 1 cm for a set of five beams with the energies of 145.88, 150.24, 154.58, 158.78, and 162.93 MeV/u, which brings the additional uncertainty to the position of this data point in Figure 2.8. The RBE value for $\overline{LET}$ = 140 keV/μm ^{16}O ions (2.27 ± 0.09) measured by [Tinganelli et al., 2013] also for an extended target of 1 cm is in agreement with these measurements.

Table 2.1.: Numerical values for the RBE_{10} calculated based on the survival data, presented in Figure 2.7 and in Appendix E. Additionally, for each LET value the linear-quadratic parameters α and β for the corresponding survival curve are presented. For the LET values of 83, 166, and 670 keV/μm (corresponding to the energies of 46.8, 19.6 and 3 MeV/u, accordingly) the linear fit was applied, thus no β values are given.

LET (keV/μm)	RBE_{10}	LQ parameters	
		α	β
23	1.222 ± 0.197	0.170 ± 0.073	0.046 ± 0.011
38	1.640 ± 0.279	0.389 ± 0.093	0.044 ± 0.015
83	2.123 ± 0.243	0.734 ± 0.057	-
166	2.285 ± 0.211	0.794 ± 0.029	-
670	1.436 ± 0.132	0.497 ± 0.018	-

An additional comparison of the data for the CHO cell line measured in 1992-1993 was performed. As can be seen from Figure 2.8, the older RBE values in the region of the intermediate and high LET values tend to be higher, while there is a match with the recent data in the low- and very high-LET regions within the error bars. There can be several reasons for the observed discrepancy. First, in contrast to the recent dataset, in 1992-1993 all the RBE values were measured for monoenergetic beams. Second, slight differences in cell culturing procedure, such as the cell growth surface or the medium used (the former protocol for the CHO cell line was described by [Mitaroff et al., 1998]), can also contribute to this discrepancy.

The updated RBE-LET data pool, summarizing all the currently published data for ^{16}O beams, including the values presented above, is given in Figure 2.9.

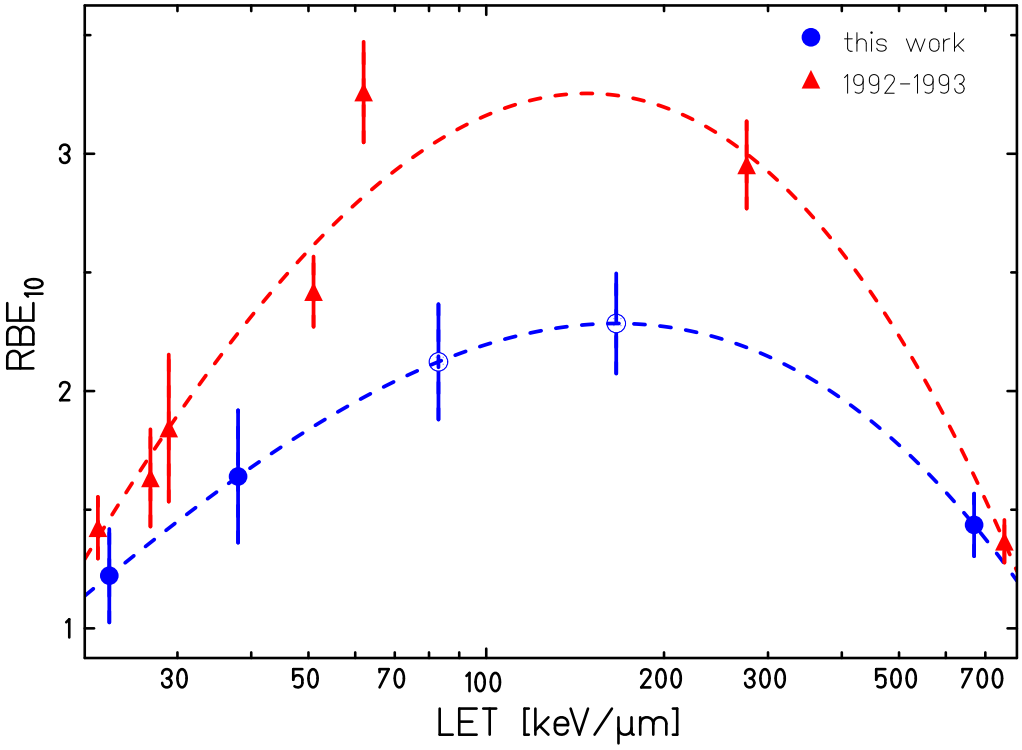

Figure 2.8.: A comparison of the calculated RBE_{10} values presented in Table 2.1 with the data measured in 1992-1993, recently published in [Sokol et al., 2017]. The closed symbols correspond to the monoenergetic irradiations, and the two open symbols correspond to the dose-averaged LET values for the 1 cm target irradiation.

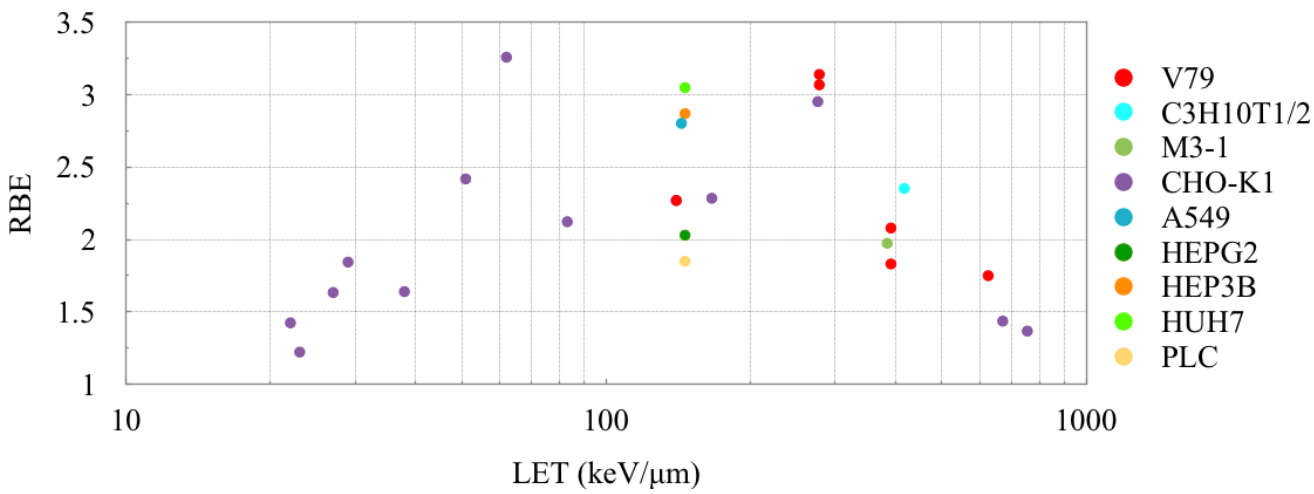

Figure 2.9.: Relative biological effectiveness of oxygen ions at 10% survival level as a function of the particle LET for various cell lines. The data for V79 cell line is taken from [Wulf et al., 1985; Pathak et al., 2007], for C3H10T1/2 - from [Miller et al., 1995], for M3-1 - from [Todd, 1975], for A549 - from [Dokic et al., 2016], for HEPG2, HEP3B, HUH7, and PLC - from [Habermehl et al., 2014], for CHO - from [Tinganelli et al., 2013; Sokol et al., 2017] and this work.

2.3.3 Oxygen enhancement ratio

Since the main area of the potential application of ^{16}O ions in therapy is expected to be the treatment of hypoxic tumors, verification of the biological effect of ^{16}O beams under this condition is essential. As a part of the RBE measurements series described above, the survival experiment for $\overline{\text{LET}}$ = 166 keV/μm was additionally repeated for the CHO cells in the anoxic (0% pO_2) condition. The comparison of the cell survival curves in normoxic and anoxic conditions is presented in Figure 2.10. For both cases, the fitting was performed based on the LQ approach with $\ln S = -\alpha D$. The numerical values for the corresponding points are given in Appendix E. For most of the data points the sizes of the symbol are larger than the error bars; thus the latter cannot be distinguished. The dashed line represents the fitted values of survival prescribed by TRiP98. There is an agreement between the prediction and the measurements in normoxic conditions within the error bars. At the same time, there is a small deviation between the TPS calculations and the measurements for the anoxic case, which needs further investigation. However, the difference between the dose values, leading to the 10% survival, predicted by TRiP98 and obtained from the fitting of experimental data, does not exceed 5%.

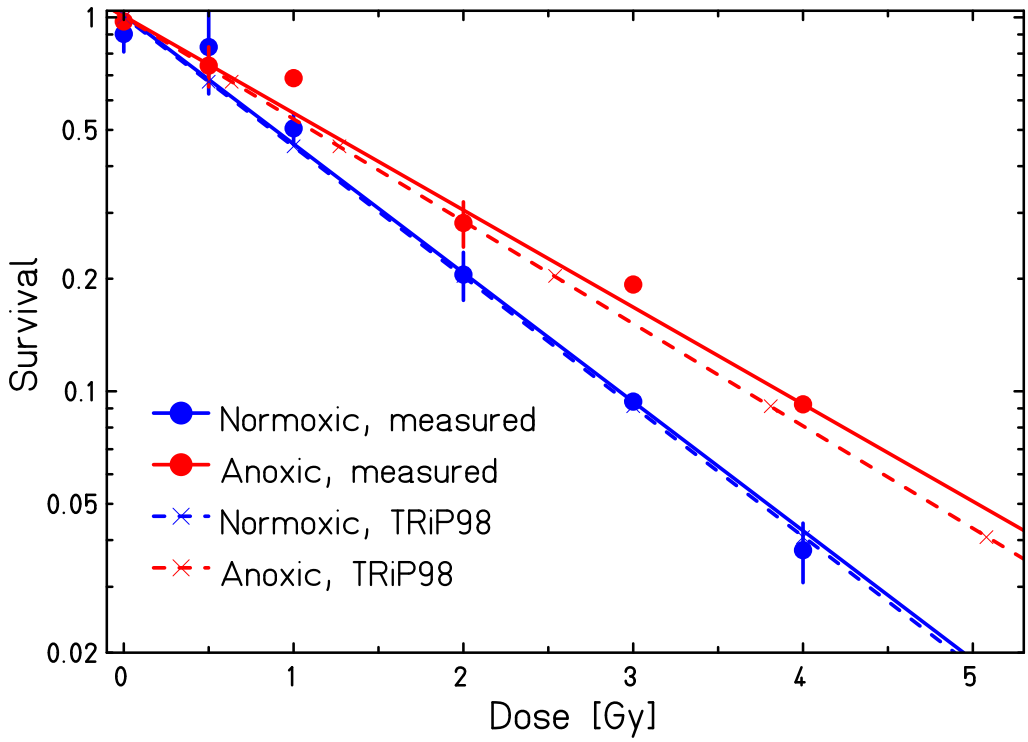

Figure 2.10.: Survival of CHO cells after irradiation with ^{16}O ions of $\overline{\text{LET}}$ = 166 keV/μm in normoxic (21% pO_2) (blue) and anoxic (0% pO_2) (red) conditions. The symbols and solid lines represent the measured survival values and the linear fitting, accordingly. The dashed lines correspond to the TRiP98 calculations. The error bars represent the ± SEM of the three corresponding independent experiments. For the dose values of 3 Gy in normoxic and 1, 3 and 4 Gy in anoxic conditions, the sizes of the error bars are smaller than the symbol size and thus they cannot be distinguished.

Based on these measurements the OER_{10} at 10% survival level can be calculated as

$$OER_{10} = \left.\frac{D(pO_2 = 0\%)}{D_{normoxic}}\right|_{S=10\%} = \frac{\alpha_{normoxic}}{\alpha_{anoxic}}, \tag{2.8}$$

where $\alpha_{normoxic}$ and α_{anoxic} are the radiobiological parameters for the survival curves in normoxic and anoxic conditions, accordingly. The resulting OER_{10} are given in Table 2.2. The measured value of OER of 1.33 ± 0.05 is in agreement with the TRiP98 prediction of 1.27 within the limits of the fitting error. From the match of this value with the model prediction of [Scifoni et al., 2013], which was originally developed based on the data for ^{12}C ions, the weak dependency of the model on the particle type for the range of charge between ^{12}C and ^{20}Ne can be concluded, as it was also found in [Furusawa et al., 2000].

Table 2.2.: The LQ parameters and the values of the OER_{10} for the survival curves in normoxic and anoxic (0% pO_2) conditions for ^{16}O ions of $\overline{LET}$ = 166 keV/μm. Both measured (fitted) and predicted (TRiP98) values are given.

pO_2	α_{TRiP98} (Gy^{-1})	α_{fitted} (Gy^{-1})	$OER_{10,TRiP98}$	$OER_{10,measured}$
21%	0.800	0.794 ± 0.029	1.27	1.33 ± 0.05
0%	0.630	0.598 ± 0.002		

2.3.4 Extended hypoxic target irradiation

Prior to the test irradiation of an unevenly oxygenated extended target, the irradiation of the similar phantom consisting of tissue culture flasks and rings with two opposite ^{16}O fields in normoxic conditions was performed. The optimization was carried out for a uniform RBE-weighted dose of 6.5 Gy. The resulting depth-survival profile along the central line is shown in Figure 2.11. The error bars are the ± SEM of two independent repetitions. The numerical values for each point are given in Appendix E. Both the measurements done with the tissue culture flasks and the rings are in the good agreement with the TPS prediction for both the entrance channel and the target regions within the error bars.

For a comprehensive testing of the biological effects caused by ^{16}O in the presence of hypoxia, the verification of the plan optimized for the same extended but partially hypoxic target was performed. Using the kill-painting approach [Tinganelli et al., 2015], the treatment plan for the CHO-K1 cell line was optimized for a uniform survival level in the target of 10%, corresponding to the RBE- and OER-weighted dose of 6.5 Gy.

The resulting survival profile measurements in depth along the central line shown in Figure 2.12. The different color regions correspond to the differently oxygenated parts of the geometry. Each measurement presented in the Figure is the average ±SEM of two independent repetitions; the numerical data are provided in the Appendix E. In general, there is a good agreement with

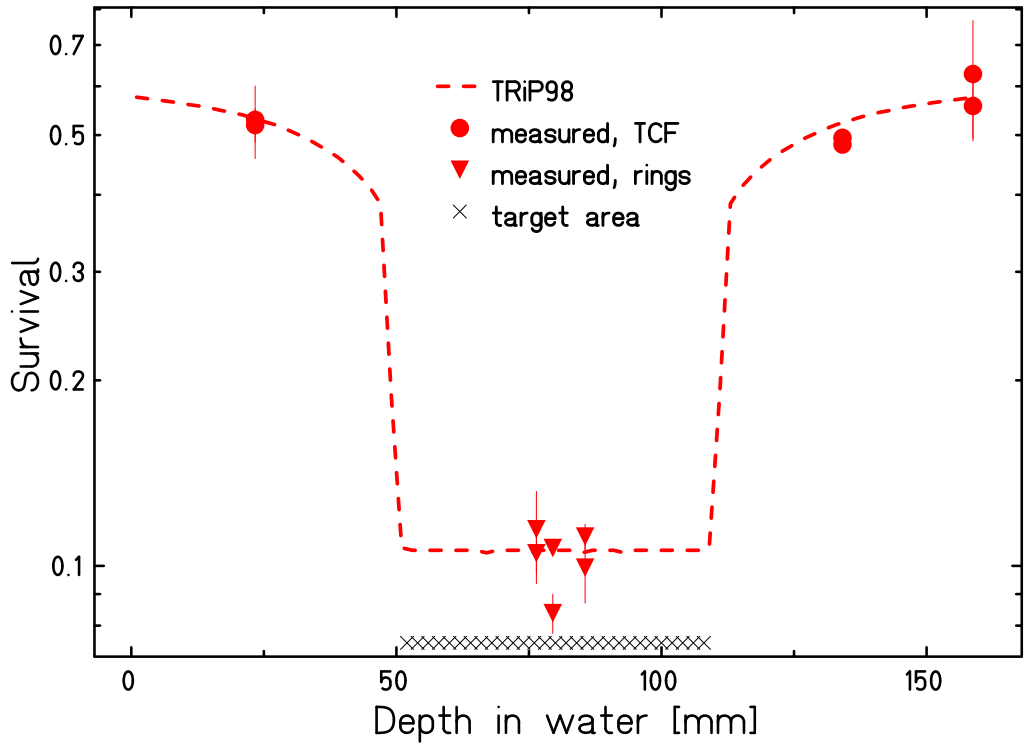

Figure 2.11.: Cell survival distribution in depth along the central line for a double-field plan optimized for a flat RBE-weighted dose of 6.5 Gy or uniform target survival level of 10% in normoxia. The dashed line corresponds to the TRiP98 prediction, the symbols - to the measured survival values. Circles correspond to the values measured with tissue culture flasks, triangles - with rings (in chambers). The target area is marked with a row of crosses.

the TRiP98 prediction (solid red line) within the frames of the error bars in both entrance channel and the target region, except the discrepancy, observed in the region with $pO_2 = 0.5\%$. However, this discrepancy, in any case, does not exceed 10%. This uncertainty can occur due to the difficulties of maintaining the intermediate level of hypoxia. A slighter increase in the oxygenation can induce a slightly lower survival since the OER values are the most sensitive to the variations of pO_2 in in this range.

For the estimation of changes in cell survival in this region that might caused by the potential fluctuations in phantom oxygenation, an additional analysis was carried out. The already produced raster files for the original phantom were taken as an input for a forward planning, and the plans were recalculated for the new oxygenation distributions. For the latter, pO_2 values were kept as 0% in the target central region, 21% in peripheral target parts and residual tissue, while the intermediate values in the target were changing from 0.1 to 0%. If pO_2 exceeds 0.5%, the recalculation will lead to the lower survival rates in this region, since the new OER values will be lower than in the original plan. Similarly, when pO_2 is lower than 0.5%, the recalculated survival rates are expected to get higher, since in this case the negative effect of hypoxia will be underestimated. The results of the analysis are given in Figure 2.13, which demonstrates the dependency of the cell survival at a depth of 65 mm for the treatment plan on the oxygenation

in the above mentioned region. As one can see from the plot, an increase of pO_2 to 0.7-0.8% leads to the drop of survival down to 0.09.

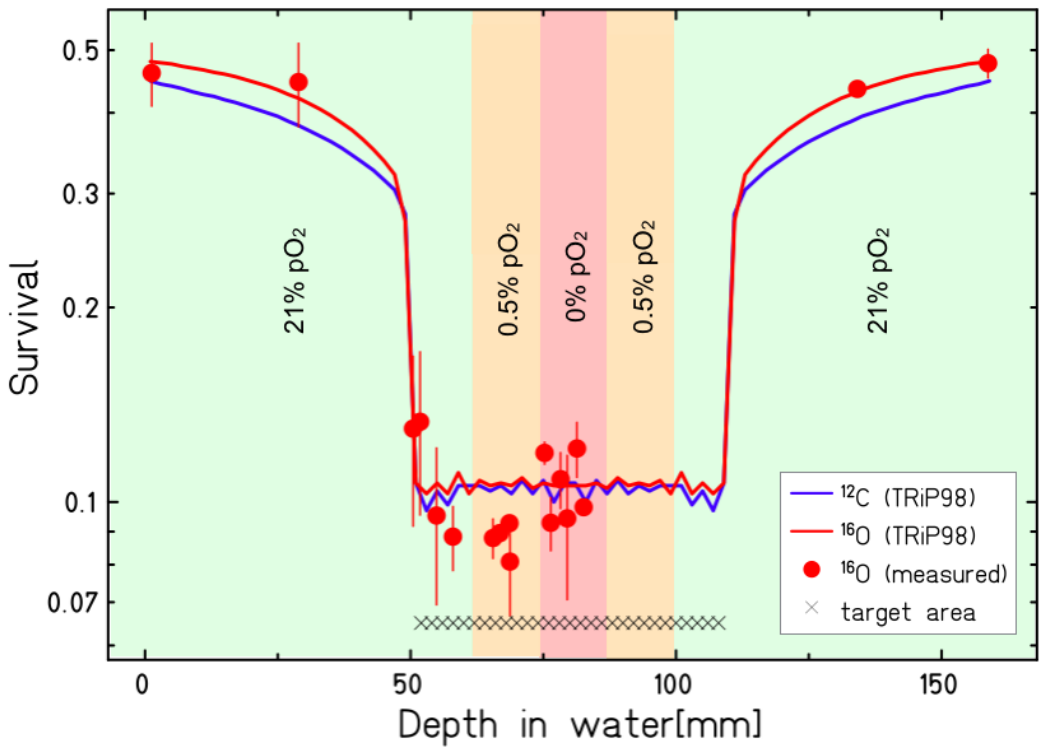

Figure 2.12.: Cell survival distribution in depth along the central line for a double-field plan optimized using the kill-painting approach for a uniform target survival level of 10%. Shaded areas correspond to differently oxygenated regions: light red - to 0% pO_2, light yellow - to 0.5% pO_2 , light green - to 21% pO_2. Points and lines correspond to the experimental results and the TRiP98 prediction for ^{12}C (blue) previously published in [Tinganelli et al., 2015] and ^{16}O (red), accordingly. The error bars represent the ± SEM of the two independent repetitions. The target area is marked with a row of crosses.

In Figure 2.12 the additional comparison with a similar plan for ^{12}C, performed by [Tinganelli et al., 2015], is included. For the sake of clarity, the comparison with only the TRiP98 prediction is performed, assuming the experimentally proven match of the corresponding experimental data with the TPS calculation. As can be seen, with a given equal survival level of 10% in the target region, ^{16}O demonstrate the better sparing of the cells in the entrance channel (EC). For a given plan, the improvement of the EC survival reaches the value of up to 10.2% at a depth of ≈ 30 mm compared to the plan optimized with ^{12}C. However, at this point one should consider the error bars for the corresponding experimental verification; thus, a more thorough analysis of this potential difference between the ions is required and is a subject of the following chapter.

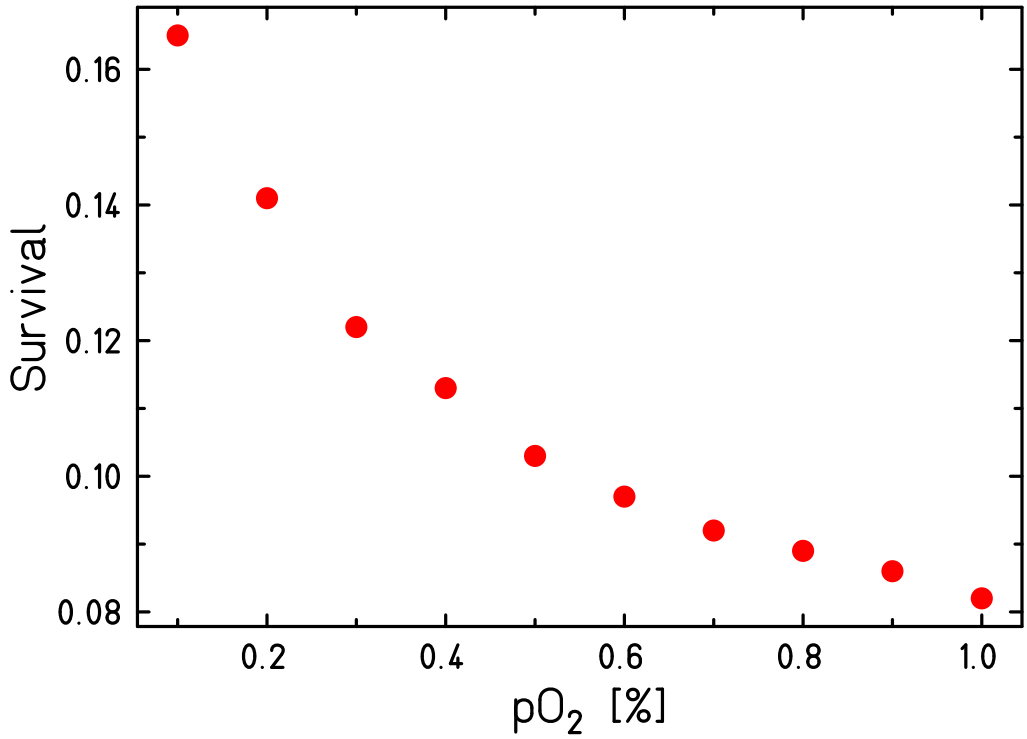

Figure 2.13.: Dependency of the cell survival at 65 mm depth for a plan, optimized for the pO_2 distribution as shown in Figure 2.12, on the fluctuations of pO_2 in the region $62 \leq z < 74$ mm.

2.3.5 Summary

The results presented in this chapter can be summarized as a first multi-scale and multi-effect description of the ^{16}O beams from a clinical point of view. The verification of physical dose profiles together with the study of radiobiological properties of the beam were carried out. The latter included the survival experiments for the cells in both normoxia and hypoxia, thus covering the range of conditions where the ^{16}O ions are expected to be applied.

The match between the pinpoint chamber measurements and the TRiP98 calculations for the absorbed dose profiles in both beam-eye view and lateral directions prove the reliability of the current status of the beam model. However, the slight discrepancy between the prediction and measurements of the lateral beam profile in the region of the fragmentation tail needs further investigation. For this particular level of the dose (less than 0.4 Gy) this deviation is negligible and will not affect the quality of the treatment plan.

The RBE measurements for the CHO-K1 cell line expand the RBE-LET dataset available for the ^{16}O ions. The measured tendency for the RBE-LET dependency follows the general trend observed by other groups for other ions, however, determining the value of the maximum requires further experiments, possibly at alternative accelerator facilities. An accompanying cell survival experiment in anoxic conditions prove both the TRiP98 radiobiological effects calculation as

well as the applicability of the OER modeling suggested by [Tinganelli et al., 2015] also for the ^{16}O ions.

The verification of the survival effect for an extended target irradiation was performed for normally oxygenated and partially hypoxic targets involving the setup consisting of different cell culture vessels. For both cases, TRiP98 was able to adequately predict the biological effect. Based on that, one can proceed with the further comparative treatment planning studies involving ^{16}O beams.

3 Treatment planning studies with oxygen beams

3.1 Introduction

The experimental verification of physical and radiobiological properties of ^{16}O beams, presented in the previous chapter, demonstrates that the currently implemented biologically effective dose calculation algorithm accounts reasonably well for both physical and biological characteristics of the beam, and proves the reliability of treatment plans produced with TRiP98.

The first indication of the potential benefit of ^{16}O over ^{12}C ions was demonstrated by the calculations of Tommasino et al. [2015] who carried out a treatment planning test for an idealized partially hypoxic box target. These estimations were confirmed by the experiment presented in the previous chapter. However, considering the error bars of these measurements, the difference in the measured survival values is not large and might be even questionable. Thus, on the one hand, it is essential to perform an additional extended analysis in the same idealized geometry to estimate the maximal possible effect of hypoxia on the plans for different ions. On the other hand, this geometry is not realistic, and in case of a real patient plan with the complex irregular shape of the target and organs at risk configuration, the effect of hypoxia can give a different contribution to the outcome.

In this chapter, a series of extended tests, including a series of primary tests with the varying impact of hypoxia on the plan, as well as several more realistic tests involving the patient data for the typical cases of chordoma, adenoid cystic carcinoma, and prostate cancer, are presented. The analysis of the results aimed at identifying the potential benefits of using oxygen ions for radiotherapy was performed, both on pure geometrical considerations and in a realistic clinical scenario.

3.2 Materials and methods

3.2.1 Model volume studies

A basic comparison of the entrance channel survival rates for ^{4}He, ^{12}C, and ^{16}O ions was performed for an idealized target geometry with varying impact of tumor hypoxia. The beam model used to generate the plans with ^{4}He was developed and validated recently by [Krämer et al., 2016].

A scenario similar to the experiment in hypoxia described in the previous chapter was used: a rectangular target of 40 × 40 × 60 mm, placed at a depth of 80 mm in water was modeled, and the entrance channel survival fraction values were calculated at 5 mm depth. The dimension of the modeled CT was 100 × 100 × 80 voxels with a voxel size of 2 × 2 × 2 mm. The scheme of the geometry showing the target and hypoxic regions configuration is shown in Figure 3.1. To stay consistent with the experiment described in the previous chapter, for the RBE prediction, the photon dose-response curve parameters $\alpha_X = 0.216$ and $\beta_X = 0.019$ (see Appendix A) for the CHO-K1 cell line, were chosen for both the target and the residual tissue. For each treatment plan, a minimum number of particles per raster point was set to 11000 in order to be consistent with the scanning monitor system capabilities. The water equivalent offset was kept as 2.89 mm which corresponds to the offset between the beam outlet and irradiation volume at HIT. The following beam characteristics and scanner parameters were set: 6, 6, and 7 mm as the beams spots focus values for ^{12}C, ^{16}O, and ^{4}He ions, accordingly, and for all the beams the scanner step size in x- and y-directions, and the approximate distance between the subsequent peak positions were set to 3 mm also considering the ripple filter used for the heavier ions. Since ^{12}C and ^{16}O beams show similar lateral scattering, it was decided to use the same widths of these beams. The optimization was performed using the plain gradient method [Horcicka et al., 2013] and the low-dose approximation for the biological dose calculation [Krämer and Scholz, 2006]. For the sake of clarity, the tests were performed for only one pO_2 value per target (a symmetrical central region with oxygenation levels of $pO_2 = 0.5\%$ or $pO_2 = 0.15\%$ along the beam direction). Three cases of prescribed survival in the target (S_T): 6.5%, 10% and 30% (which would correspond to flat RBE-weighted target doses of 4, 6.5 and 7.5 Gy of normoxic plans with the same parameters, accordingly) were investigated. In total, for each combination of S_T and pO_2 values 21 sample runs with a hypoxic region size step of 2 mm were performed for each ion.

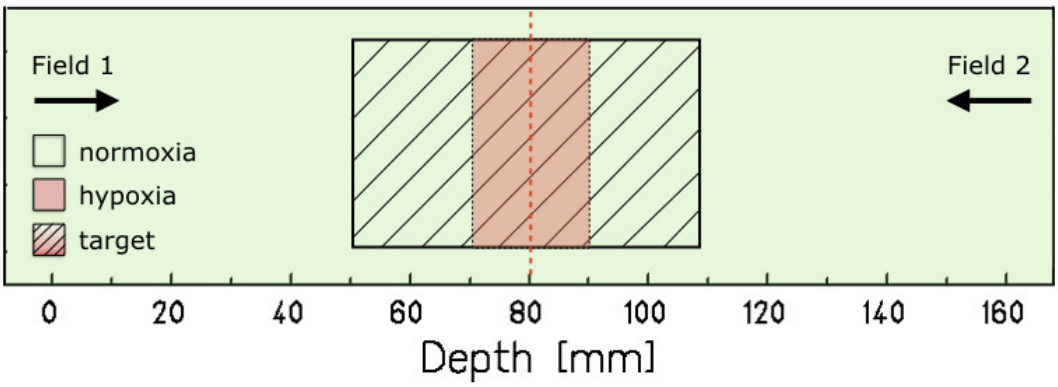

Figure 3.1.: Schematic representation of the geometry for entrance channel survival tests. The normally oxygenated area of the simulated geometry is shown in light green. The shaded area represents the target, where the area in light red corresponds to the hypoxic (0.5 or 0.15% pO_2) central part the size of which was varied between the tests. The red dashed line depicts the center of geometry at z = 80 mm in water. The two opposite fields are indicated by arrows.

3.2.2 Patient plans

The base treatment data for the three pairs (later referred as cases A and B) of typical cases of skull base chordoma, adenoid cystic carcinoma (ACC) and prostate cancer were taken from the GSI pilot project patients archive. This includes the imaging files, such as CT and contours files, and the TPS plans files used for treatment with ^{12}C ions. From the latter ones, the technical parameters such as the target centers, field configurations, and directions, were transferred to the new plans to preserve the clinically reasonable conditions. The new treatment plans were generated using the most recent base data for ^{1}H, ^{4}He, ^{12}C, and ^{16}O ions. The radiobiological parameters were chosen as $\alpha_X = 0.003$ Gy^{-1}, $\beta_X = 0.0015$ Gy^{-2}, and transitional dose D_t = 22 Gy as in [Grün et al., 2015], based on the photon input parameters for late toxicity in the central nervous system.

The focus values for the beam spots were chosen as 10, 7, 5, and 5 mm for ^{1}H, ^{4}He, ^{12}C, and ^{16}O, respectively. To provide a reasonable ratio between the number of raster points and the number of voxels (i.e. to avoid overdetermination), the scanner step sizes in *x-, y*-directions and the approximate distance between the subsequent peak positions were set to 3 mm.

Each plan was optimized for two ion fields aiming at a flat RBE- (in normoxia) or RBE and OER-weighted (in hypoxia) dose of 2 Gy per fraction. The CT parameters and beam angles, exported from the original treatment plans of the pilot project are given in Table 3.1.

Table 3.1.: Characteristics of the treatment plans generated for the test involving the patient plans for chordoma, adenoid cystic carcinoma and prostate cancer based on the plans used during the GSI pilot project with ^{12}C ions. The given geometry parameters are corresponding total CT dimensions, voxel sizes (CT steps) in and the target center position in *x-, y-, and z*-directions. Each plan was optimized for the two fields, thus two corresponding couch angles are given.

Tumor	CT dimension			CT steps, mm			Target center, mm			Couch angle	
	x	y	z	x	y	z	x	y	z	Field 1	Field 2
Chordoma A	256	256	98	1.12	1.12	3	144.62	128.23	126.0	100	-100
Chordoma B	256	256	110	1.21	1.21	3	153.33	153.79	135.0	100	-100
ACC A	256	256	111	1.21	1.21	3	133.81	146.83	151.5	50	104
ACC B	256	256	114	1.12	1.12	3	176.43	130.05	171.0	-50	-104
Prostate A	256	256	113	1.95	1.95	3	228.96	245.07	192.0	90	-90
Prostate B	256	256	139	1.91	1.91	3	243.6	248.49	187.5	90	-90

For each plan, the organs in the proximity of the target volume were defined as organs at risk, which implies applying the dose constraints (equation 1.12) to these structures. The constraints defined by the clinicians during the pilot project were mainly preserved. For the plans for chordoma the brainstem was selected and the maximal dose fraction (MDF), e.g., the maximal

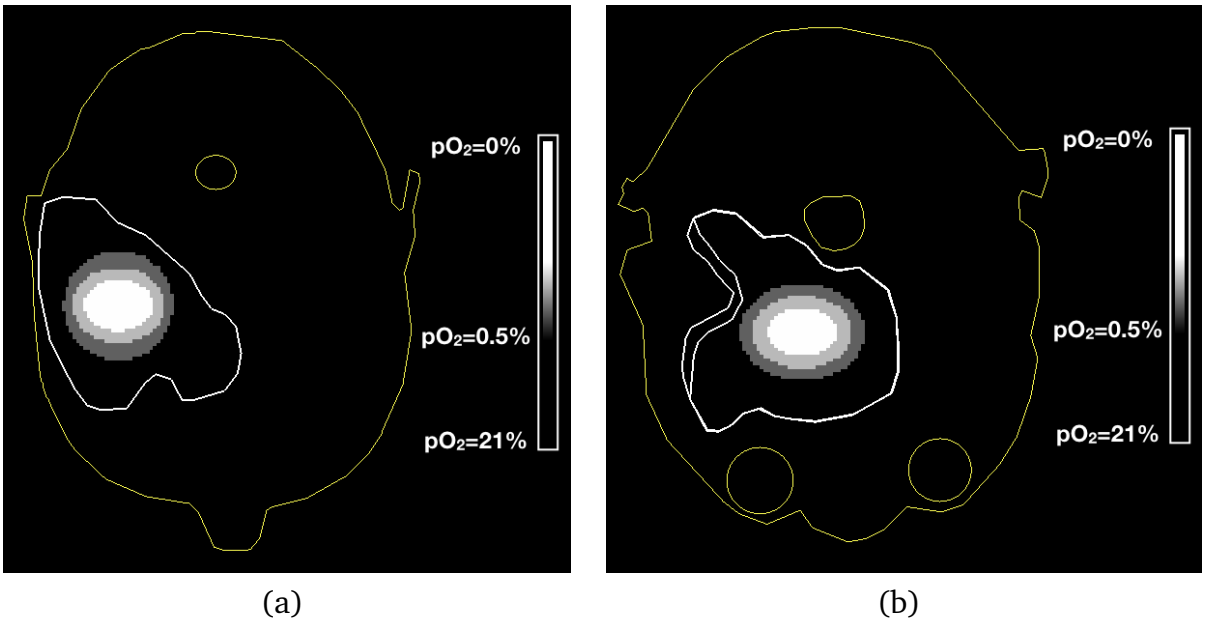

Figure 3.2.: An example of a generated hypoxia distribution inside an adenoid cystic carcinoma tumor. Two oval hypoxic regions consisting of an outer region with 0.5% pO_2 oxygenation level, medium region with 0.15% pO_2, and inner anoxic (0% pO_2) region were modeled inside the different parts of the tumor and are shown in gray colors. The rest of the volume is normally oxygenated (21% pO_2). The outer yellow line corresponds to patient's head contour, the inner yellow lines marks the brainstem (a) and additionally the eyes (b), and the white line marks the tumor contour. (a) Slice 46 out of 111. (b) Slice 55 out of 111.

dose allowed to the organ compared to the prescribed dose, was set 0.7. In case of the plan for the ACC, case A, apart from the brainstem, the right optical nerve was selected as well. The MDFs to both the brainstem and the nerve were set to 0.4. The weighting factors (WF), characterizing the 'importance' of this constraint were set to 0.9. For the case B, the original plan did not imply any constraints to OAR, but for the current study the MDF and WF for the brainstem were set to 0.5 and 0.9, respectively. For the prostate treatment plan, the rectum and the bladder were located very close to the tumor. In the original plan, the corresponding optimization constraints were set to 0.7 with a WF of 0.5. For the current tests, it was decided to emphasize these organs, and the WF was reset to 1, however, to avoid sacrificing the tumor coverage quality, the maximum dose fraction was increased to 0.8. For the prostate case B both MDF and WF for the bladder and rectum were set to 0.8.

For performing the treatment planning tests with partially oxygenated tumors, artificial FMISO-PET uptake data cubes were created using the external plug-in (courtesy of Prof. C. Bert). The details on the pO_2 handling procedure are given in Appendix F and are also relevant for the next chapter. It was assumed the modeled hypoxia to be chronic, thus more likely occurring in the central parts of the tumor. For each patient, the ellipsoidal hypoxic regions with isocentric hypoxic parts with three or four levels of oxygenation were generated approximately

in the center of the investigated tumor. For the tests with chordoma and prostate tumor, having rather a regular shape between the different CT slices, one hypoxic region per tumor was modeled. The both cases of ACC case had quite irregular shapes dramatically varying between the slices. Thus, to simulate a higher contribution of hypoxia to the plan, it was decided to model two regions in the different areas of the tumor for each of the geometries. An example of the generated ellipsoidal hypoxia distribution and the tumor, OAR (brainstem) and eyes contours for ACC case A are shown in Figure 3.2. Here, two slices of the patients' head geometry in axial view (outer yellow contour) at $z = 16.5$ and $z = 14.1$ cm are shown with the ACC tumor contour outlined in white. For a given slice, the four-level pO_2 distribution (21%, 0.5%, 0.15% and 0%) is shown in greyscale. The tumor sizes and the information about the modeled oxygenation distribution for each of the six analyzed cases are given in Table 3.2.

Tumor type		Total volume, cm^3	pO_2 %	Volume, cm^3	% of the total volume
Skull base chordoma	Case A	102.37	0	16.02	16
			0.15	24.53	24
			21	61.82	60
	Case B	126.48	0	10.73	8
			0.15	8.41	7
			0.5	16.87	13
			21	90.46	72
Adenoid cystic carcinoma	Case A	213.19	0	6.48	3
			0.15	15.08	7
			0.5	28.83	14
			21	162.80	76
	Case B	115.75	0	4.85	4
			0.15	5.49	5
			0.5	11.60	10
			21	93.8	81
Prostate tumor	Case A	148.99	0	30.06	20
			0.15	15.18	10
			0.5	18.10	12
			21	85.66	58
	Case B	52.43	0	5.66	11
			0.15	7.54	14
			0.5	12.87	25
			21	26.36	50

Table 3.2.: Parameters of the hypoxia maps generated for the GSI pilot project patients plans. Total volume stands for the total volume of the target. Two or three isocentric regions with oxygenation decreasing towards its centers were created for every tumor. The sum volumes of equally oxygenated tumor subvolumes and their ratio to the total tumor volume are given in the last two columns.

3.3 Results and discussion

3.3.1 Basic analysis accounting for target hypoxia

Despite the value of the ratio $\alpha_X/\beta_X \approx 2$ being more common in clinics, characterizing the late toxicity in the CNS [Karger et al., 2006], it was decided to stick to the CHO cell line parameters with $\alpha_X/\beta_X \approx 11$ to rather analyze the 'boundaries' of the survival experiment described in the previous chapter, than to get closer to clinical conditions in this study. The investigation of the treatment plans with $\alpha_X/\beta_X \approx 2$ was left for the next step implying the analysis with realistic patient geometries.

For this particular case of equal target and normal tissue radiosensitivities, there is no high impact of RBE and the final survival effect is mainly modulated by the value of prescribed dose and the impact of tumor hypoxia. In normoxic cases the calculated RBE- and OER-weighted dose and resulting cell damage in the EC is justified to be the lowest for ^{4}He ions, that deliver the lowest physical dose and produce fewer fragments, compared to ^{12}C and ^{16}O; this is in agreement with a recent study by Grün et al. [2015]. The result of the optimization for three ions for a normally oxygenated target for a prescribed RBE-weighted dose is given in Figure 3.3.1.

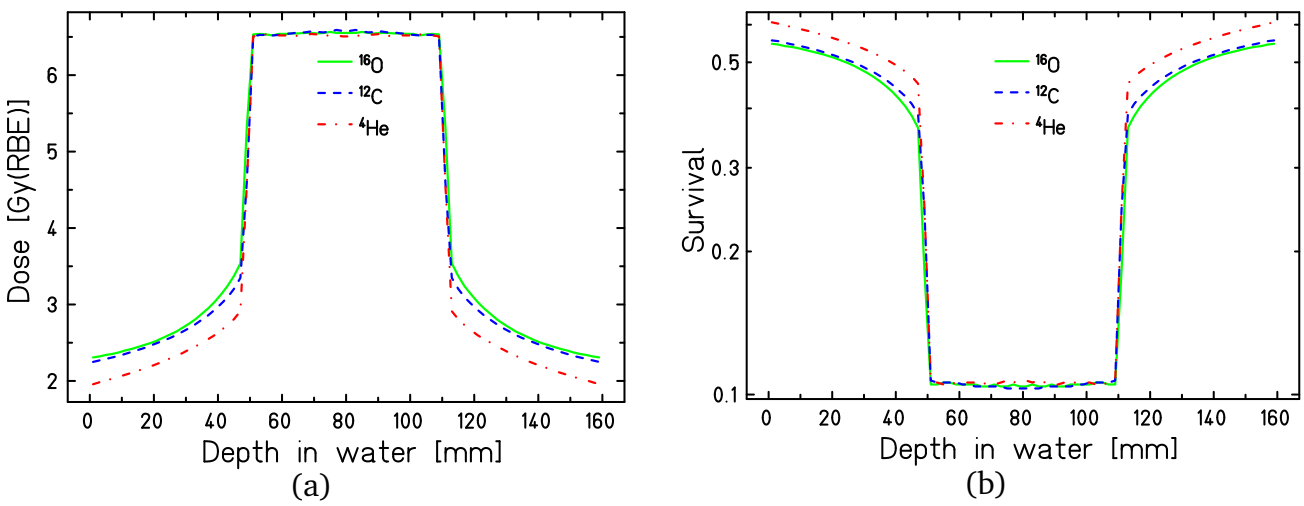

Figure 3.3.: Depth-dose profiles for oxygen (solid green line), carbon (dashed blue line), and helium (dot-dashed red line) ions plans optimized for a unform RBE-weighted dose of 6.5 Gy in the 60 mm target for the CHO-K1 cell line with $\alpha_X/\beta_X \approx 11$. (a) RBE-weighted dose profile. (b) Survival profile.

The survival levels for each plan were extracted in the region of the entrance channel at 5 mm depth and are given in Appendix G. For several calculated data points the general survival decrease trend is broken, and for the slightly higher hypoxic contribution, the calculated EC survival can be lower than for the smaller hypoxic region size. This might happen because of the different relative locations of the voxels borders or centers and the borders of hypoxic

regions. Additionally, there is generally some 'freedom' for the optimization since no additional constraints for the planning were introduced. However, despite these fluctuations, the clear trend in the survival decreases for each ion, prescribed survival and oxygenations can be distinguished.

The resulting trends of the survival decrease at 5 mm depth in the entrance channel for each combination of expected target survival and the pO_2 level in the hypoxic region are shown in Figure 3.4. In case of a smaller contribution of hypoxia ($\lessapprox$ 1-2 cm region) the effect is similar to the one in absence of hypoxia, when ^{4}He generally demonstrate the lowest cell kill in the entrance channel, while ^{16}O behaves similar or only slightly worse than ^{12}C ions. With the further increase of the size of the hypoxic region, the trend lines start to cross. The first crossing point normally occurs for the ^{16}O and ^{12}C lines', meaning that sparing of healthy tissue by using ^{16}O ions becomes more efficient. The crossing with the ^{4}He line occurs later or, as can be noticed from Figures 3.4(a) and 3.4(b), these two lines can cross only at the very high values of hypoxic region size (Figure 3.4(a)) or become indistinguishable within the confidence interval. In this case, the prescribed dose is the highest among the analyzed cases, and in normoxic case, the difference between ^{4}He and the heavier ions is the largest. Thus, this initial benefit seems to outweigh the effect of hypoxia with further decrease of oxygenation, even for a relatively large region. Thus, when one aims at a higher cell killing after a single irradiation (cell survival $<$ 10%) in the target, switching to heavier ions seems to be not justified: compared to lighter ions, the use of ^{16}O increases the survival in the EC by less than 4% and only when the significant part of tumor is hypoxic. However, applying such high doses is not very common in clinics, and the analysis of the plans with a lower prescribed biological doses deserves more attention.

Figures 3.4(c) and 3.4(d) represent the results obtained for the treatment plans for the same prescribed dose as in the experiment described in the previous chapter. While for the less hypoxic tumors (pO_2 = 0.5%) switching to the heavier modalities remain questionable, for the lower levels of oxygenation the improvement in the entrance channel survival can reach up to $\approx$ 10-12% but only when the major part of the target is hypoxic.

The most pronounced effect can be observed for the lowest of the prescribed doses that were tested (4 Gy, figures 3.4(e) and 3.4(f)). In this case, the difference between the ions in the normoxic case is less significant. With increasing size of the central hypoxic region and decreasing its oxygenation, the benefit of ^{16}O ions over lighter ions becomes more pronounced since the effect of lower OER is more likely to outweigh the initial negative effect of nuclear fragmentation. For higher (0.5%) oxygenation levels, the usage of heavier modalities is still not justified unless a significant part of the tumor is hypoxic. In this case, according to the model of Scifoni et al. [2013], the maximal possible OER values will not exceed $\approx$ 1.7. However, for the lower (0.10 - 0.2%) pO_2 values the OER may increase up to $\approx$ 2.5. With ^{16}O demonstrating the dose-averaged LET of $\approx$ 100 keV/μm in the hypoxic region, one should expect the reduction of the OER by approximately a factor of two. That may lead to a relative increase of survival in the entrance channel by up to $\approx$ 13-15% and its pronounced benefit when already less than a half of the target is hypoxic.

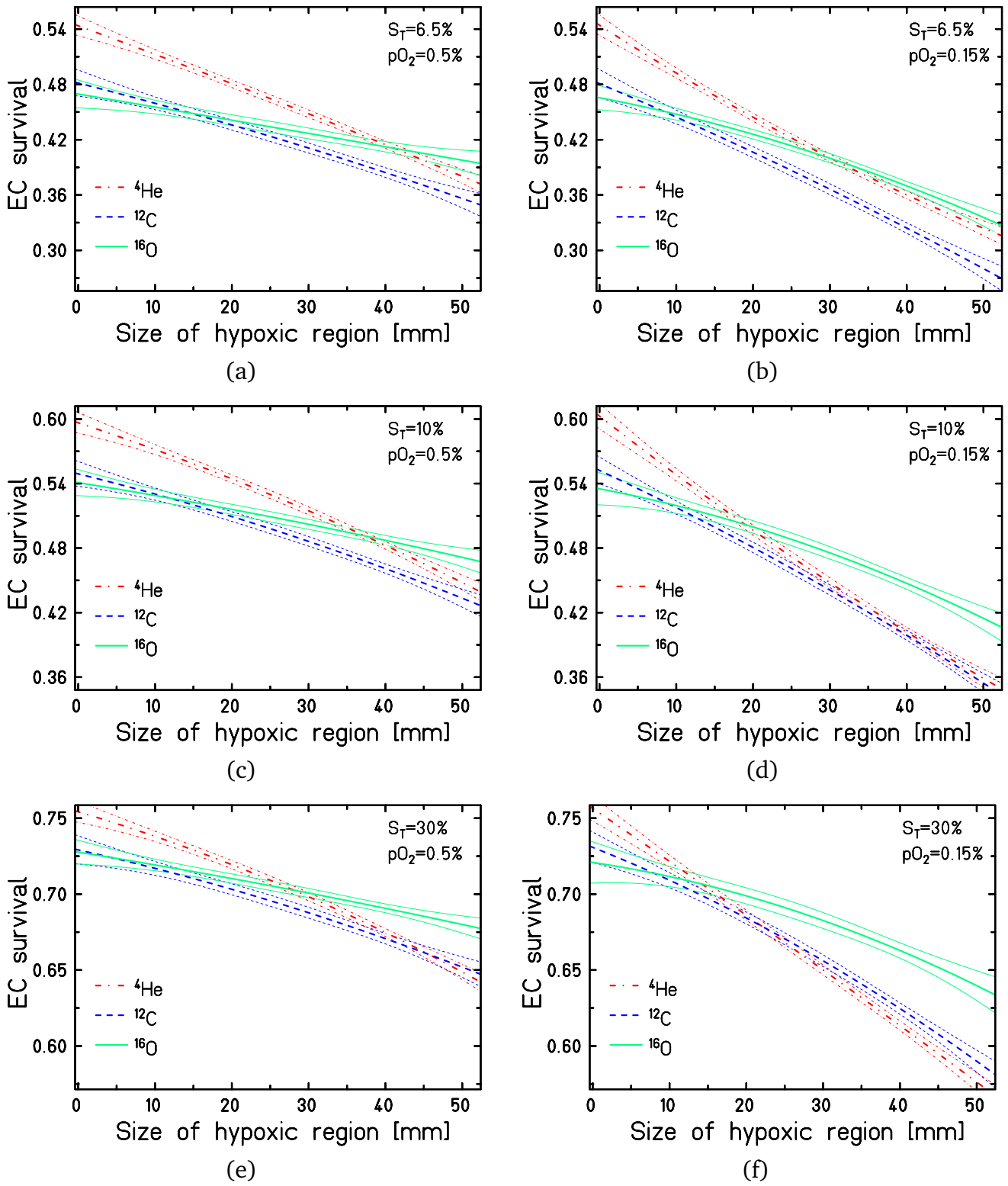

Figure 3.4.: Dependency of the survival rate calculated by TRiP98 at a depth of 5 mm (entrance channel) on the size of the central hypoxic target region for ^{4}He (red dash-dot line), ^{12}C (blue dashed line) and ^{16}O (green solid line) ions for a fixed target survival rate. The corresponding couples of thin lines of the same style enclose the 95% confidence intervals for each dependency. (a) S_T = 6.5%, pO_2 = 0.5%, (b) S_T = 6.5%, pO_2 = 0.15%, (c) S_T = 10%, pO_2 = 0.5%, (d) S_T = 10%, pO_2 = 0.15%, (e) S_T = 30%, pO_2 = 0.5%, (f) S_T = 30%, pO_2 = 0.15%. The target of 60 mm is centered at a depth of 80 mm.

3.3.2 Tumor control probability analysis

In order to achieve a better therapeutic outcome, the treatment is often divided into several fractions, so the dose to the patient is delivered in smaller portions during the period of several weeks. This allows better sparing of normal tissue through repair and repopulation of its cells during the time between fractions. In this section, the parameters, related to the fractionated treatment, are analyzed based on the results presented in the previous section.

Another level of the quantitative assessment of the treatment plan is the estimation of the tumor control probability (TCP), which describes the probability that a given dose of radiation will provide tumor control or eradication of specific tumor cells [Brady and Yaeger, 2013]. In this section, based on the EC survival data from the previous section, a TCP analysis, comparing OER-optimized plans for the different ions with the normoxic plan, was performed.

In the case of inhomogeneous cell survival in a voxelized target, the Poissonial model of TCP

$$\mathrm{TCP} = e^{-NS(D)} \tag{3.1}$$

with N denoting the initial number of clonogenically active cells and S - the survival fraction after the dose D, can be rewritten as

$$\mathrm{TCP} = \prod_{i=1}^{N} e^{-(\mathrm{S}_i)^n \nu_i \rho_i} \tag{3.2}$$

where n is the number of fractions, S_i is the survival in each voxel i of volume ν_i, ρ_i is the density of cells per unit volume, and N is the total number of voxels. Applying the 'normoxic' plan for a partially hypoxic tumor will lead to the presence of different survival regions in it after the irradiation. For this case, assuming the two regions of different oxygenation in the tumor as in the treatment planning tests in previous section, and voxels equal in terms of size ν and cells contained ρ, the equation can be simplified to the following:

$$\mathrm{TCP}_{\mathrm{non-opt}} = e^{-\rho\,\nu\left(S_1^n \frac{V_{normox}}{V_t} + S_2^n \frac{V_{hypox}}{V_t}\right)} \tag{3.3}$$

$$V_{normox} + V_{hypox} = V_t \tag{3.4}$$

where S_1 is the planned survival and $S_2 > S_1$ is the resulting increased survival ('underkill'). The example of such an optimization resulting in an uneven survival for two different values of $p\mathrm{O}_2$ in the hypoxic region is shown in Figure 3.5. At the same time, for the OER-optimized plan the resulting survival is expected to be uniform and the equation 3.2 can be rewritten as

$$\mathrm{TCP}_{\mathrm{oer-opt}} = e^{-\rho\,\nu S_1^n}. \tag{3.5}$$

At this point is should be mentioned that for the calculations in this sections the small fluctuations in the cell survival at the different regions interfaces, caused by the drastic changes of target oxygenation, were neglected. Thus, for the further calculation in this section, only one survival level inside the target is assumed for an OER-optimized plan.

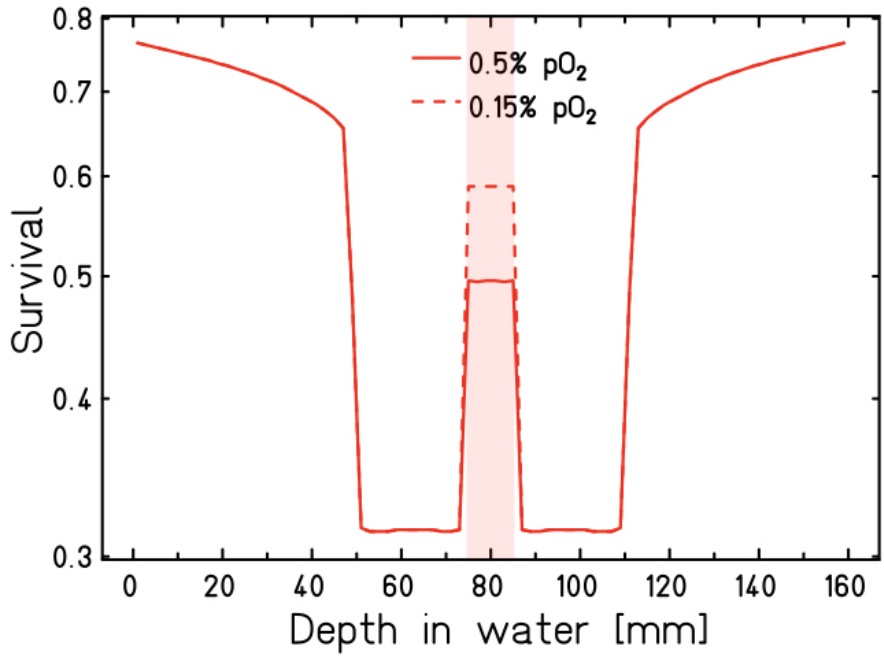

Figure 3.5.: Depth-dose survival profiles for ^{4}He ions plans optimized for a unform RBE-weighted dose of 4 Gy in the 60 mm target for the CHO-K1 cell line with $\alpha_{\mathrm{X-ray}}/\beta_{\mathrm{X-ray}} \approx 11$, not accounting for the presence of hypoxia in the center of the target (the region shaded with light red color). Depending on its oxygenation, with the same survival in the entrance channel, this results in the different peaks in the survival distribution in the target (solid line - 0.5% $p\mathrm{O}_2$, dashed line - 0.15% $p\mathrm{O}_2$).

For the planning tests in the previous section, the voxel volume was 8 mm^3 and the target is 20 × 20 × 30 voxels, thus ν = 96000 mm^3. The cell density per voxel was taken as 10^4 as in [Tinganelli et al., 2015]. Using a similar approach, the comparison of normoxic and OER-optimized plans for different ions can be made using the concept of the biologically effective dose (BED) in the entrance channel [Hall and Giaccia, 2006]. This quantity is commonly used in radiotherapy for comparison of different fractionation regimes.

The biological effect after n fractions, delivering the total dose D can be calculated using the LQ approach as

$$E = -\ln S = \alpha D + \beta D^2, \tag{3.6}$$

where S is the cell survival, and α and β are the radiobiological parameters for a reference survival curve for the analyzed cell line. At the same time, the equation 3.6 can we written as

$$E = n\left(\alpha d + \beta d^2\right) = \alpha\, n\, d\left(1 + \frac{d}{\alpha/\beta}\right), \tag{3.7}$$

where d stands for the dose per single fraction and $D = nd$. The quantity E/α is called the biologically effective dose:

$$BED = nd\left(1 + \frac{d}{\alpha/\beta}\right). \tag{3.8}$$

Thus, with the same dose per fraction, the relation between the numbers of fractions that are required to get the same survival in the entrance channel for the non-OER optimized (normoxic) plan (n_{normox}) and the plan accounting for oxygenation ($n_{OER-opt}$) can be expressed as

$$n_{non-opt}S_{non-opt} = n_{OER-opt}S_{OER-opt} \tag{3.9}$$

For the comparative analysis of the TCP, the data from the previous section for a prescribed biological 'normoxic' dose of 4 Gy was taken, since it is the lowest and closest to the clinical conditions. Since ^{4}He demonstrates the lowest cell kill in the entrance channel in case of the normoxic tumor or a plan optimized not accounting for tumor hypoxia, the corresponding plan was chosen as a reference for the comparison with all the following OER-optimized plans. The TCP analysis was performed with two pO_2 values of 0.5% and 0.15% for two sizes of hypoxic regions: 1 cm where the impact of hypoxia is very low and 5 cm when the observed effect is significant. Thus, the values of S_1 and S_2 were set to 0.31 and 0.49 for pO_2=0.5% and 0.31 and 0.59 for pO_2=0.15%, accordingly. The results of the BED calculations at 5 mm depth in the entrance channel are given in Figure 3.6.

From all the four analyzed cases can be expected an improvement in the local control using an OER-optimized plan instead of the normoxic one. However, for small sizes of the hypoxic regions this improvement is not strongly dependent on the ion type, as seen from the Figures 3.6(a) and 3.6(c). In particular, the ratio of the BED leading to the TCP of 50% for the tumor with the 1 cm of pO_2=0.5% region for the normoxic and OER-optimized plans is 1.36, 1.26, and 1.20 for ^{4}He, ^{12}C and ^{16}O, respectively (Figure 3.6(a)). For the same region size but with the decreased oxygenation of 0.15% the corresponding values change to 1.68, 1.63, and 1.59 (Figure 3.6(c)), accordingly. Here one should keep in mind the above-mentioned fluctuation in the entrance survival levels, which might add a ≈10% uncertainty to these values. With the increase of OER contribution to the optimization, the ratio of BED for the normoxic and the OER-optimized plans is decreasing, but its values become well distinguished between the lighter and heavier ions (Figures 3.6(b) and 3.6(d)). The corresponding ratio of the BED leading to the TCP of 50% is 1.02, 1.04, and 1.14 for ^{4}He, ^{12}C and ^{16}O ions, respectively, for the tumor with a 5 cm of pO_2=0.5% region and 1.11, 1.12, and 1.3, respectively, for the tumor with the 5 cm of pO_2=0.15% region.

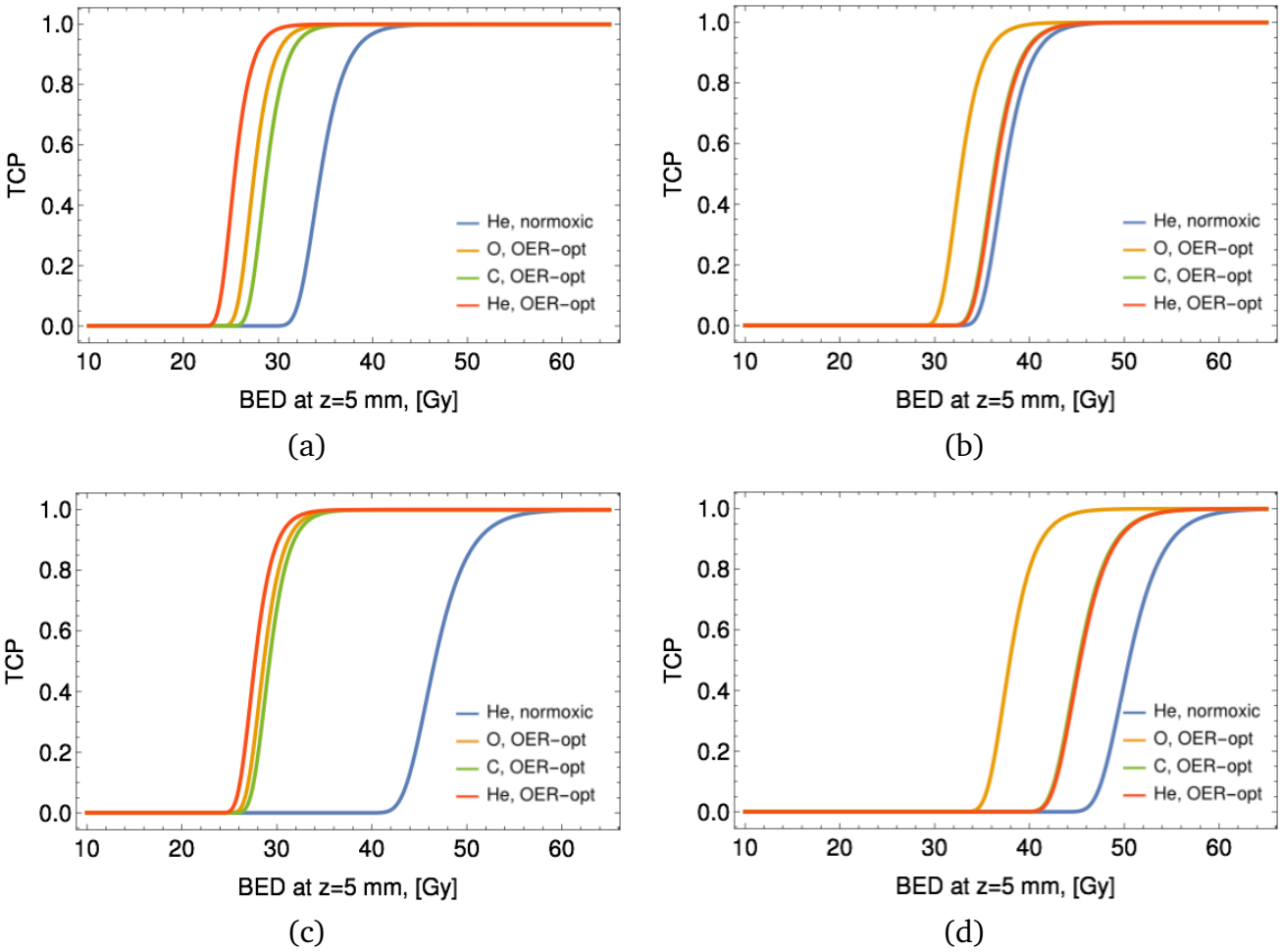

Figure 3.6.: Comparison of the tumor control probability (TCP) as a function of a biologically effective dose (BED) in the entrance channel for the ^{4}He ion plan not accounting for the presence of hypoxia (normoxic) and the OER-optimized plans for ^{4}He, ^{12}C and ^{16}O ions for different contributions of tumor hypoxia. The prescribed uniform biological dose per fraction to a rectangular partially hypoxic target of 6 cm was 4 Gy. The calculations were performed based on the calculated cell survival data provided in Appendix F. The BED was calculated at 5 mm depth and indicates the similar damage to the residual tissue after applying several fractions of each plan to the target. (a) 1 cm central target region with 0.5% pO_2. (b) 5 cm central target region with 0.5% pO_2. (c) 1 cm central target region with 0.15% pO_2. (d) 5 cm central target region with 0.15% pO_2.

3.3.3 Analysis of patient plans from GSI pilot project

In the previous section the geometry of the target region was not varying between the CT slices, thus not leading to sharp dose changes, neither in proximal nor in lateral directions. In reality, the tumor is irregular and never has a similar shape for every two neighboring cuts. This might affect the outcome of the treatment planning. For example, if the size of the tumor is decreasing from one CT slice to the next one, the dose to the residual tissue in the smaller cut will be increased due to the fragmentation or scattering of ions in the target region in the previous slice.

The previous analysis aimed at the estimation of the effect in the beam entrance channel. Knowledge of the damage to the tissue and structures in this region is important, however, in the realistic treatment plans more attention, apart from the tumor coverage, is paid to the damage caused to the critical structures (OAR). The clinicians select the field configuration in order to avoid these structures being located in the beam entrance channel. Thus, the structures marked OARs tend to receive the dose arising mainly from the lateral scattering of the primary beam and its fragments. Accessing the damage to such structures was a part of the presented analysis.

This section describes the additional treatment plan analysis involving real patient geometries. The result of the optimization was assessed by means of dose-volume histograms (DVH), that included the information about the target dose, the dose to the OARs (brainstem in case of chordoma and ACC tumors or rectum and bladder in case of the prostate cancer) and the residual tissue. Additionally, the maximal, minimum and mean dose values received by these volumes, were assessed. In case of prostate cancer, the additional analysis of the dose received by one of the two hip joints was performed. This way, the dose received by the OARs and by residual tissue was analyzed together with the quality of the target coverage.

The resulting two-dimensional RBE- and OER-weighted dose distributions at three central CT cuts (axial, coronal and sagittal) and the corresponding dose-volume histograms for the two cases of medium-sized skull base chordomas are shown in Figures 3.7 (case A) and 3.8 (case B), respectively. There the contours of the emulated isocentric hypoxic regions are additionally outlined with the dotted lines. The tumors in the two analyzed cases are of comparable sizes and shapes. However, the ratio of volumes with the decreased oxygenation to the normoxic volumes is different. The first tumor is more hypoxic, as can be seen from the Table 3.2: apart from the smaller normally oxygenated part, only the regions with $pO_2 = 0.15\%$ and 0% are present, while in the case B there is a region with an increased pO_2 value of 0.5%.

As can be seen from the DVHs for the targets, in normoxic case all the four modalities demonstrate similar tumor coverage for both cases. Heavier ions (^{12}C and ^{16}O), however, can be more beneficial regarding the lowest standard deviation from the corresponding target dose mean values. In the first case they are 0.04 and 0.03 Gy compared to 0.05 and 0.06 Gy for ^{4}He and ^{1}H, respectively. For the second tumor the deviations are 0.04, 0.05, 0.06, and 0.09 for ^{16}O, ^{12}C, ^{4}He, and ^{16}H, respectively. The presence of the hypoxia significantly affects the tumor coverage

by the lighter ions, especially protons. For them, the standard deviation increases up to 0.28 and 0.19 Gy in cases A and B, respectively, which is almost 10% and 20% of the prescribed dose. In contrast, ^{16}O ion plan is least affected by the presence of hypoxia.

From the Figures 3.7(a) and 3.8(a) can be observed that, considering the field configuration and the relative positions of the tumor and the brainstem, the dose to the latter will be a result of the particle scattering and fragmentation. Since protons demonstrate the highest lateral scattering, this can be the explanation for the dose delivered to the brainstem being the highest for them in normoxic case. On the other hand, the other explanation for the highest dose for protons can be the initial beam spot size, which is the largest for them. The intermediate mean dose delivered by ^{16}O ions (0.264 Gy (case A) and 0.304 Gy (case B), respectively) compared to the doses delivered by ^{12}C and ^{4}He (0.181 and 0.354 Gy in case A, 0.238 and 0.426 Gy in case B, respectively), might be explained by the lowest lateral scattering, however, the highest contribution of nuclear fragmentation among the four ions.

The DVHs demonstrate that the mean dose to the brainstem is almost independent on the oxygenation status of the tumor for both cases. This statement should be addressed with caution for protons, since with the observed inadequate tumor coverage the overall suitability of the plan is questionable.

Table 3.3 summarizes the minimal, maximal, and mean relative doses delivered to the target, brainstem and residual tissue for each ion, compared to the prescribed RBE- and OER-weighted target dose of 2 Gy. While the numbers for the average brainstem doses confirm the trend observed from the DVH, another important trend can be observed for the values of the maximal doses to both the brainstem and residual tissue. In case of the brainstem, this dose might be received by its parts situated in the proximity to the tumor and which can be considered as the 'hotspots'. Since the total volume that received this very high dose is significantly lower than the total volume of the brainstem, these hotspots have almost no impact on the value of the mean dose. However, at the same time, this parameter should be considered for accessing the risk of damaging serial organs [Brady and Yaeger, 2013].

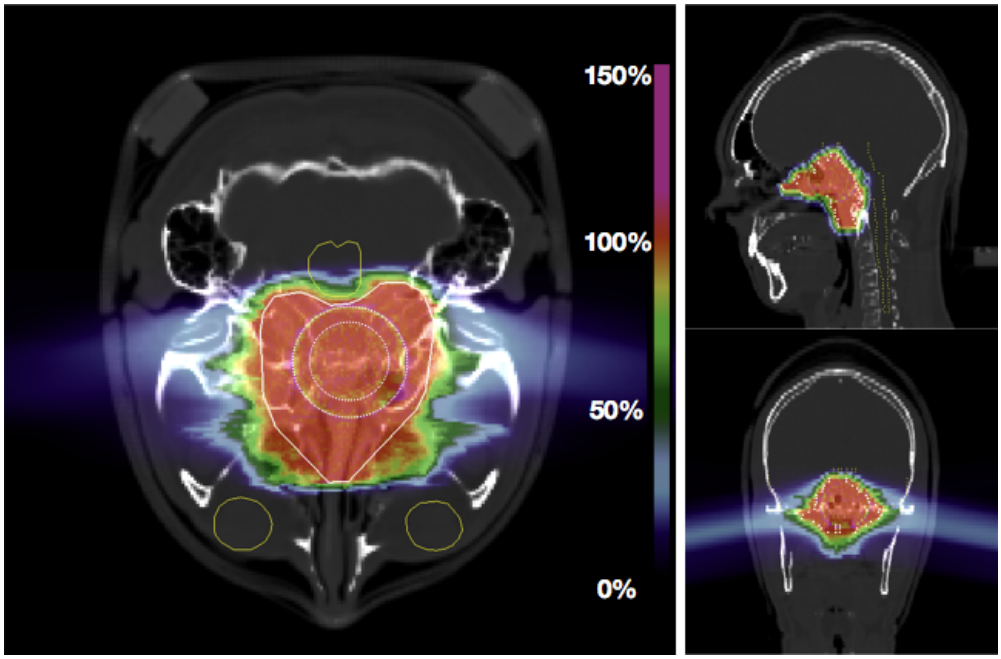

(a)

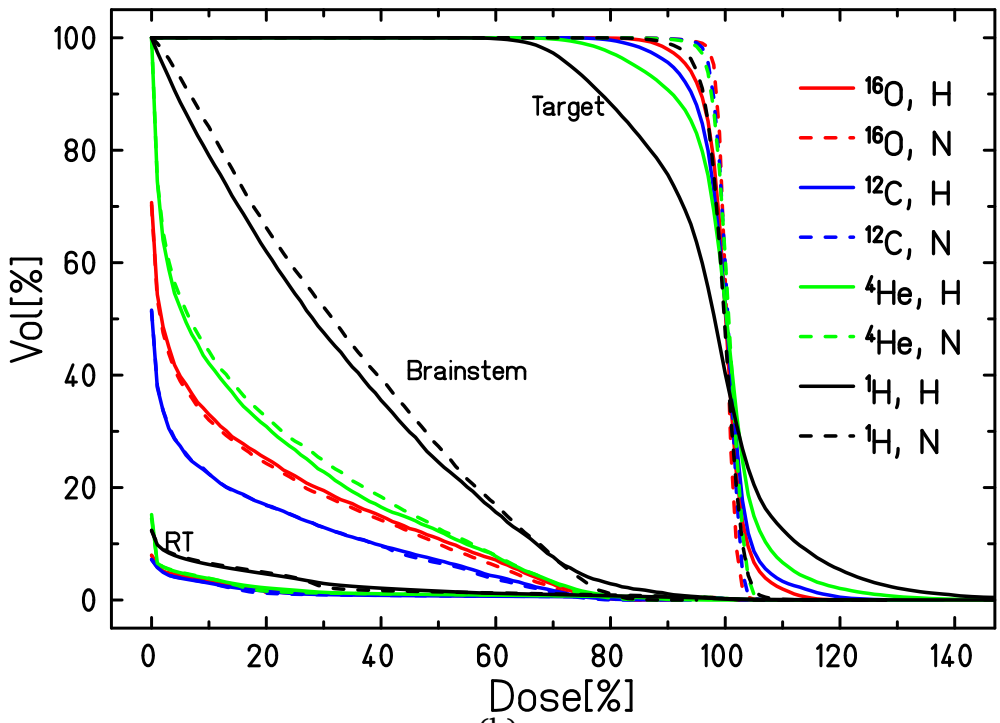

(b)

Figure 3.7.: Biologically optimized two-field plan for a partially hypoxic skull base chordoma, case A. (a) RBE- and OER-optimized biological dose distributions in axial, coronal and sagittal planes. The solid white line marks the tumor, yellow lines - brainstem (OAR) and eyes (on the first cut). The two isocentric hypoxic regions with 0% and 0.15% pO_2 are marked with dotted white lines. The scale represents the relative dose received by the tissue, compared to the prescribed biological dose of 2 Gy. (b) DVHs for the target, brainstem and residual tissue (RT) for the plans with ^{16}O (red), ^{12}C (blue), ^{4}He (green), and ^{1}H (black) for the cases of hypoxic (solid line) and normoxic (dashed line) chordoma.

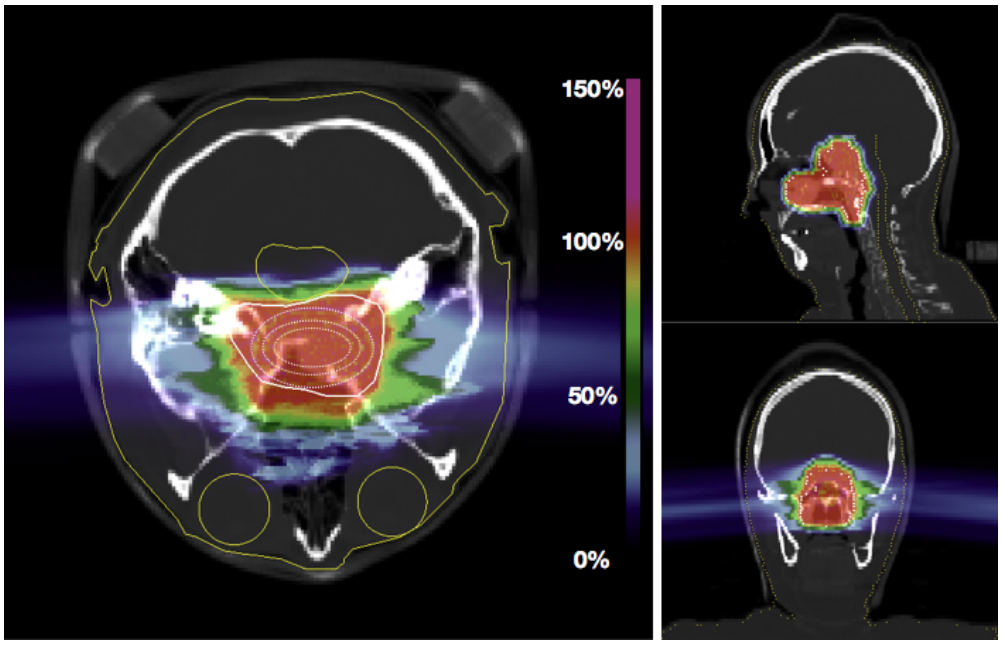

(a)

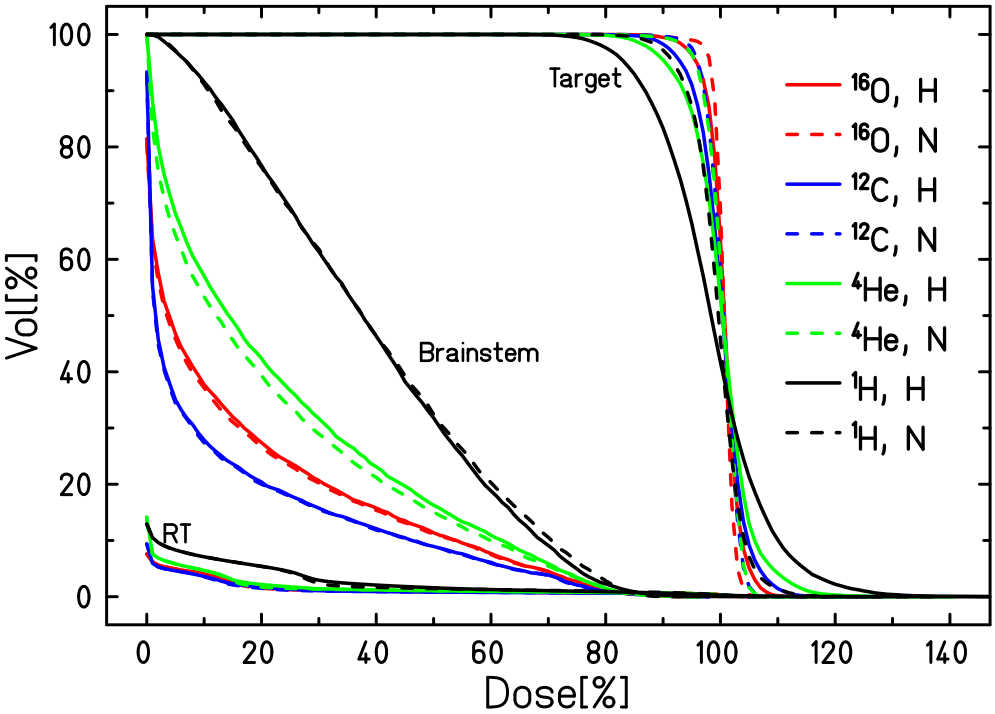

(b)

Figure 3.8.: Biologically optimized two-field plan for a partially hypoxic skull base chordoma, case B. (a) RBE- and OER-optimized biological dose distributions in axial, coronal and sagittal planes. The solid white line marks the tumor, yellow lines - brainstem (OAR) and eyes (on the first cut). The two isocentric hypoxic regions with 0% and 0.15% pO_2 are marked with dotted white lines. The scale represents the relative dose received by the tissue, compared to the prescribed biological dose of 2 Gy. (b) DVHs for the target, brainstem and residual tissue (RT) for the plans with ^{16}O (red), ^{12}C (blue), ^{4}He (green), and ^{1}H (black) for the cases of hypoxic (solid line) and normoxic (dashed line) chordoma.

Ion	VOI	Case A						Case B					
		Normoxic tumor			Hypoxic tumor			Normoxic tumor			Hypoxic tumor		
		D_{min}/D_p	D_{max}/D_p	D_{mean}/D_p	D_{min}/D_p	D_{max}/D_p	D_{mean}/D_p	D_{min}/D_p	D_{max}/D_p	D_{mean}/D_p	D_{min}/D_p	D_{max}/D_p	D_{mean}/D_p
^{16}O	Target	0.80	1.11	1	0.76	1.23	0.99	0.65	1.12	1.01	0.65	1.17	1.01
	Brainstem	0	0.84	0.13	0	0.87	0.14	0	0.93	0.15	0	0.92	0.16
	Residual	0	1.15	0.013	0	1.22	0.013	0	1.15	0.015	0	1.17	0.015
^{12}C	Target	0.81	1.13	1	0.67	1.35	0.99	0.67	1.13	1	0.66	1.24	1
	Brainstem	0	0.83	0.09	0	0.91	0.09	0	0.96	0.12	0	0.95	0.12
	Residual	0	1.19	0.012	0	1.35	0.012	0	1.19	0.013	0	1.24	0.014
^{4}He	Target	0.65	1.15	1	0.58	1.54	0.99	0.72	1.12	1	0.69	1.39	1
	Brainstem	0	0.86	0.18	0	0.96	0.18	0	0.95	0.21	0	0.93	0.23
	Residual	0	1.16	0.015	0	1.57	0.016	0	1.19	0.017	0	1.39	0.018
^{1}H	Target	0.72	1.19	0.99	0.54	1.80	0.97	0.60	1.26	0.99	0.61	1.60	0.99
	Brainstem	0	0.88	0.34	0	1.08	0.32	0	0.92	0.39	0	1.05	0.39
	Residual	0	1.19	0.026	0	1.80	0.026	0	1.34	0.028	0	1.60	0.028

Table 3.3.: Minimal (D_{min}), maximal (D_{max}) and average (D_{mean}) relative doses, compared to the planned dose of 2 Gy(RBE,OER) (D_p), received by the target, brainstem and residual tissue in case of irradiating normoxic or partially hypoxic skull base chordoma with ^{16}O, ^{12}C, ^{4}He and ^{1}H ions.

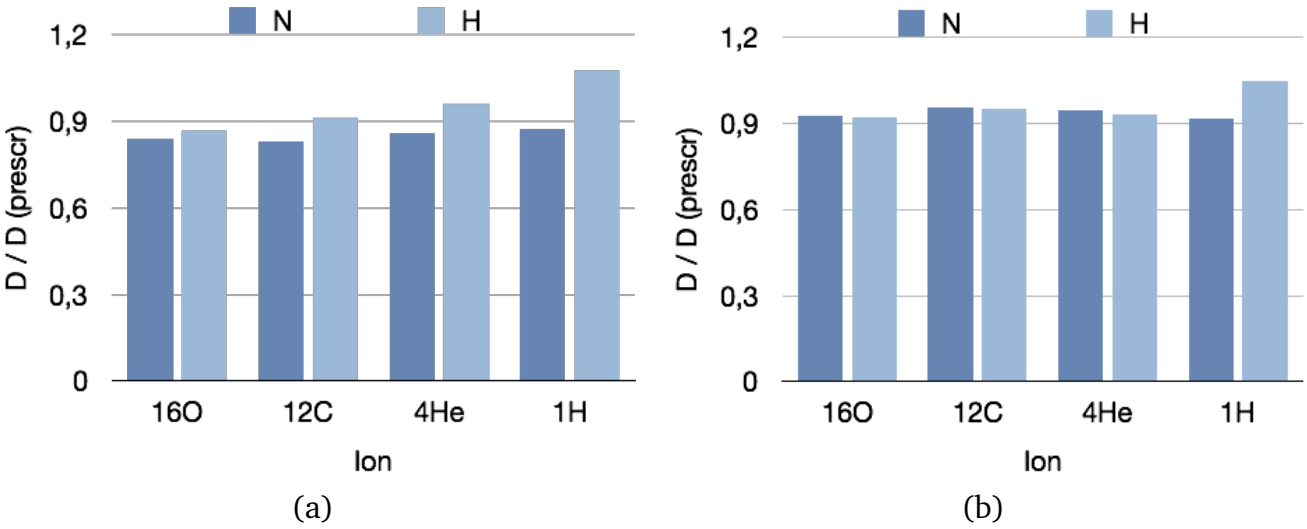

Figure 3.9.: Maximal relative dose received by the brainstem for the plans optimized for a 2 Gy RBE- and OER-weighted dose for a normoxic (N) or partially hypoxic (H) skull base chordoma irradiated with ^{16}O, ^{12}C, ^{4}He, or ^{1}H. (a) - case A, (b) - case B.

The histograms, comparing the maximal doses received by the brainstem in hypoxic in normoxic conditions for the four ions for cases A and B, are shown in Figures 3.9(a) and 3.9(b), respectively. In the case A, while in normoxia this parameter is not noticeably varying between the ions, with the decrease of target oxygenation the heaviest ions demonstrate a clear benefit in the form of the lowest values. The maximal dose delivered by ^{16}O is 5.5% and 16.6% lower than the maximal dose for ^{12}C and ^{4}He, accordingly. The similar trend for the maximal dose can also be observed for the residual tissue (Table 3.3). The corresponding improvement from using ^{16}O is 9.3% and 23% compared to ^{12}C and ^{4}He, accordingly. For the second tumor, there is no such significant difference in the values of the maximal dose to the brainstem (Figure 3.9(b)) between ^{16}O, ^{12}C and ^{4}He plans. Moreover, one can also notice almost no difference between the respective doses in normoxia in hypoxia.

The similar analysis was carried out for the ACC tumors. The two analyzed cases of ACC tumors had an almost two-fold difference in sizes (≈213 and ≈116 cm^3) but similar level of oxygenation (≈80% of the total volume was assumed to be normoxic, the rest had four levels of decreased oxygenation). Compared to chordoma, both tumors were located closer to the head surface and were irradiated at similar angles with two fields at 50 and 104 or -50 and -104 degrees, respectively. The RBE- and OER-weighted dose distributions at three central orthogonal CT cuts and the dose-volume histograms for cases A and B are displayed in Figures 3.10 and 3.11, respectively. Compared to both chordoma cases, these tumors had more irregular shapes and thus there were regions of the residual tissue inbetween that received the increased dose according to the optimization results. In both cases, the mean dose to the residual tissue appears to be slightly higher than in case of chordomas. Regarding the tumor coverage, the trend is the same as in case of chordomas: ^{16}O ion demonstrate the best tumor coverage and the least dependence on the presence of hypoxia. The numerical values of the relative doses

to the tumor, brainstem and residual tissue for the ACC case are given below in the Table 3.4. Since protons demonstrate the similar scenario for the tumor coverage in hypoxia as for the chordoma plan, they are not mentioned in the further comparison.

For this plan, the higher constraints to the OAR were applied (the maximal allowed dose fraction to the brainstem was set to 0.4 for case A and 0.5 for case B). Thus, as can be seen from the Figures 3.10(b) 3.11(b) and Table 3.4, the respective average doses are relatively low. For both cases, ^{12}C ions deliver the lowest mean dose for both normoxic and hypoxic conditions. The analysis of the maximal doses summarized in Figure 3.12 also leave ^{12}C as a best choice for both cases of oxygenation. It is also possible to note that the trends for the doses to the OAR remain independent on the target size, when the other plan parameters remain similar.

A possible explanation to the difference in the trend for the maximal doses for the two analyzed tumor types can be the relative position of the target and the OAR. In case of chordoma for the given fields configuration, the brainstem is a lateral OAR, which implies that one should expect it to receive the dose produced mainly by the scattered particles and initial beam width. Since at these depths ^{16}O and ^{12}C experience comparable scattering Schardt et al. [2010], the lower required dose of ^{16}O might lead to the decrease of the maximal dose in the brainstem. For the given cases of ACC, the brainstem is located partially in the fragmentation tail of one of the two fields. Since ^{16}O ions generate more fragments than ^{12}C, even the decreased required dose in hypoxia might not overweight this effect, leaving ^{12}C ions the best option for this particular case of ACC. As follows from the numerical values of maximal doses for the brainstem, this parameter is almost not affected by this level of tumor hypoxia, disregarding the tumor size. At this step, only one out of the four analyzed tumor cases (chordoma, case A) with the smallest ratio of the normally oxygenated tissue to the total tumor volume ($\approx$60%) demonstrated the distinguishable difference in the maximal dose to the brainstem between the plans for normoxic and hypoxic tumors. Also, in this case the plan with ^{16}O has demonstrated an appreciable lowest maximal doses to the target and residual tissue compared to the lighter ions in case of a hypoxic tumor. For the other three cases of hypoxic tumors the plans with ^{16}O perform very similar to the ones with ^{12}C.

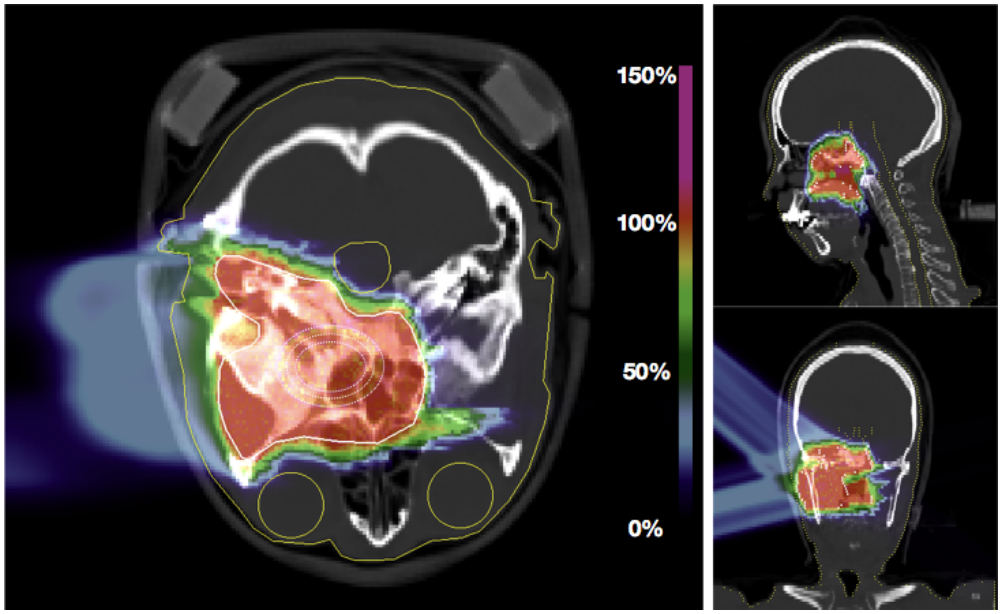

(a)

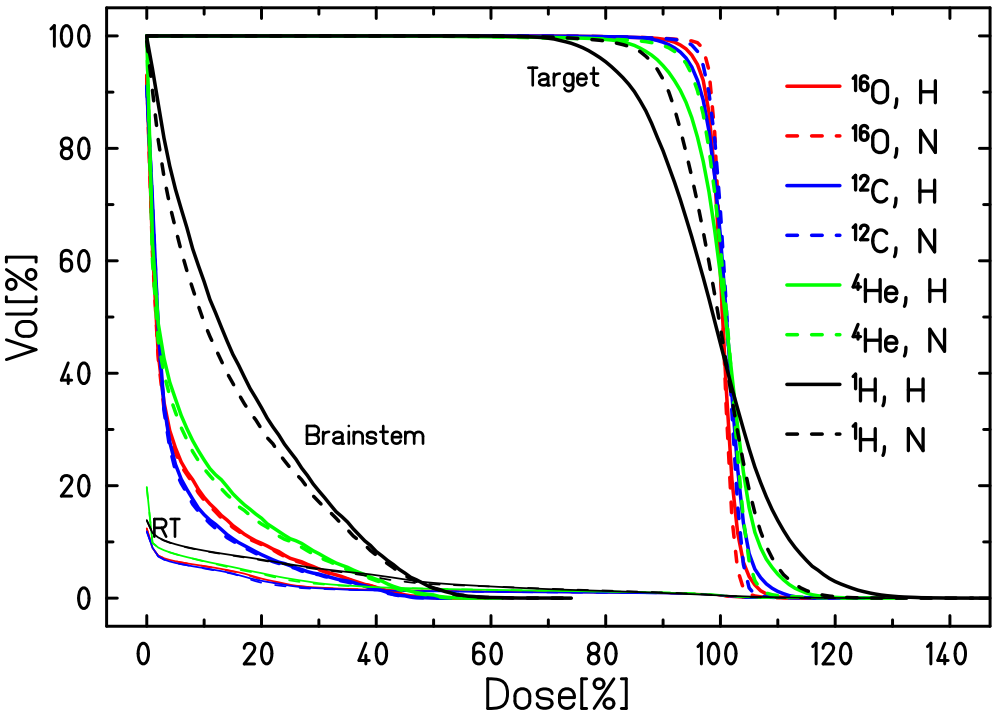

(b)

Figure 3.10.: Biologically optimized two-field plan for a partially hypoxic adenoid cystic carcinoma, case A. (a) RBE- and OER-optimized biological dose distributions in axial, coronal and sagittal planes. The solid white line marks the tumor, yellow lines - brainstem (OAR) and eyes. The scale represents the relative dose received by the tissue, compared to the prescribed biological dose of 2 Gy. The three isocentric hypoxic regions with 0%, 0.15%, and 0.5% pO_2 are marked with dotted white lines. More detailed configuration of the hypoxic regions are given in Figure 3.2. (b) DVHs for the target, brainstem and residual tissue (RT) for the plans with ^{16}O (red), ^{12}C (blue), ^{4}He (green), and ^{1}H (black) for the cases of hypoxic (solid line) and normoxic (dashed line) ACCs.

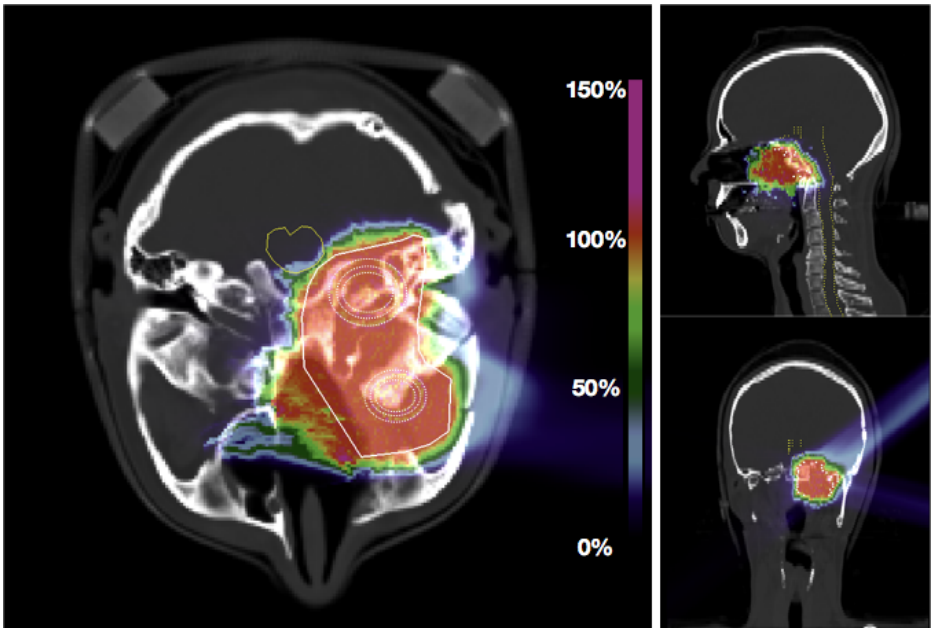

(a)

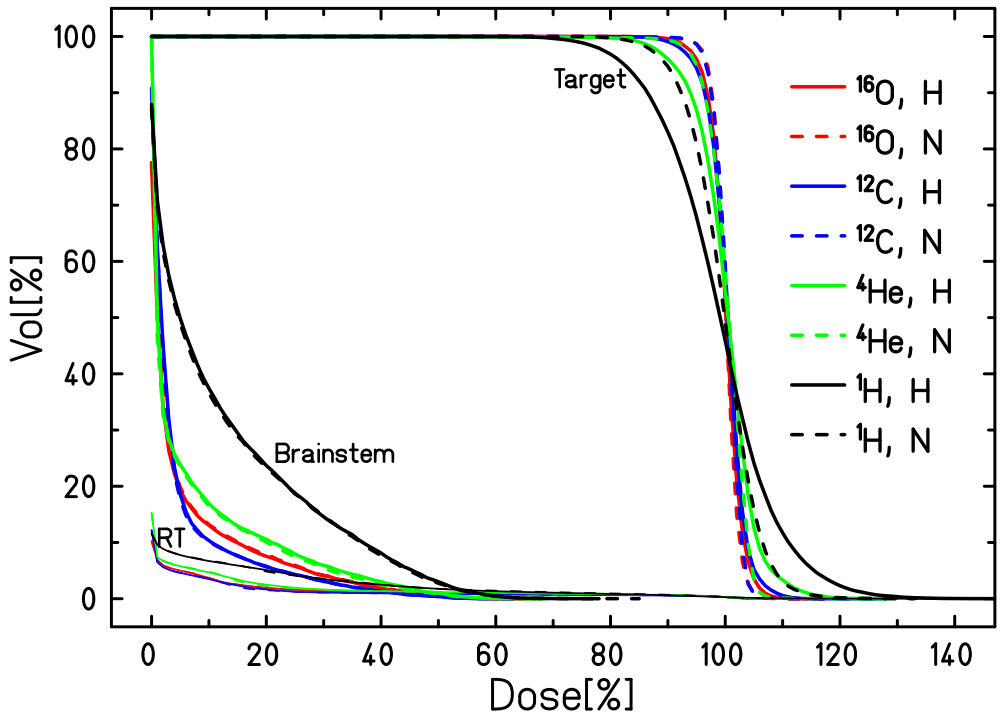

(b)

Figure 3.11.: Biologically optimized two-field plan for a partially hypoxic adenoid cystic carcinoma, case B. (a) RBE- and OER-optimized biological dose distributions in axial, coronal and sagittal planes. The solid white line marks the tumor, yellow line - the brainstem. The scale represents the relative dose received by the tissue, compared to the prescribed biological dose of 2 Gy. The isocentric hypoxic regions with 0%, 0.15%, and 0.5% pO_2 are marked with dotted white lines. More detailed configuration of the hypoxic regions are given in Figure 3.2. (b) DVHs for the target, brainstem and residual tissue (RT) for the plans with ^{16}O (red), ^{12}C (blue), ^{4}He (green), and ^{1}H (black) for the cases of hypoxic (solid line) and normoxic (dashed line) ACCs.

Ion	VOI	Case A						Case B					
		Normoxic tumor			Hypoxic tumor			Normoxic tumor			Hypoxic tumor		
		D_{min}/D_p	D_{max}/D_p	D_{mean}/D_p	D_{min}/D_p	D_{max}/D_p	D_{mean}/D_p	D_{min}/D_p	D_{max}/D_p	D_{mean}/D_p	D_{min}/D_p	D_{max}/D_p	D_{mean}/D_p
^{16}O	Target	0.61	1.22	1	0.60	1.23	1	0.66	1.13	1	0.66	1.15	1
	Brainstem	0	0.55	0.06	0	0.56	0.06	0	0.64	0.05	0	0.64	0.05
	Residual	0	1.22	0.022	0	1.23	0.022	0	1.21	0.015	0	1.21	0.015
^{12}C	Target	0.51	1.23	1.01	0.49	1.23	1.01	0.14	1.14	1	0.14	1.16	1
	Brainstem	0	0.49	0.05	0	0.51	0.05	0	0.62	0.04	0	0.63	0.04
	Residual	0	1.23	0.021	0	1.3	0.021	0	1.23	0.014	0	1.22	0.014
^{4}He	Target	0.42	1.29	1	0.38	1.30	1	0.46	1.18	1	0.41	1.27	1
	Brainstem	0	0.58	0.07	0	0.59	0.08	0	0.67	0.06	0	0.67	0.06
	Residual	0	1.29	0.027	0	1.46	0.028	0	1.18	0.018	0	1.27	0.019
^{1}H	Target	0.55	1.42	0.99	0.54	1.46	0.98	0.64	1.34	0.99	0.57	1.48	0.99
	Brainstem	0	0.72	0.15	0	0.7	0.16	0	0.83	0.12	0	0.78	0.12
	Residual	0	1.47	0.039	0	1.55	0.039	0	1.44	0.029	0	1.48	0.028

Table 3.4.: Minimal (D_{min}), maximal (D_{max}) and average (D_{mean}) relative doses, compared to the planned dose of 2 Gy(RBE,OER) (D_p), received by the target, brainstem and residual tissue in case of irradiating normoxic or partially hypoxic adenoid cystic carcinoma with ^{16}O, ^{12}C, ^{4}He and ^{1}H ions.

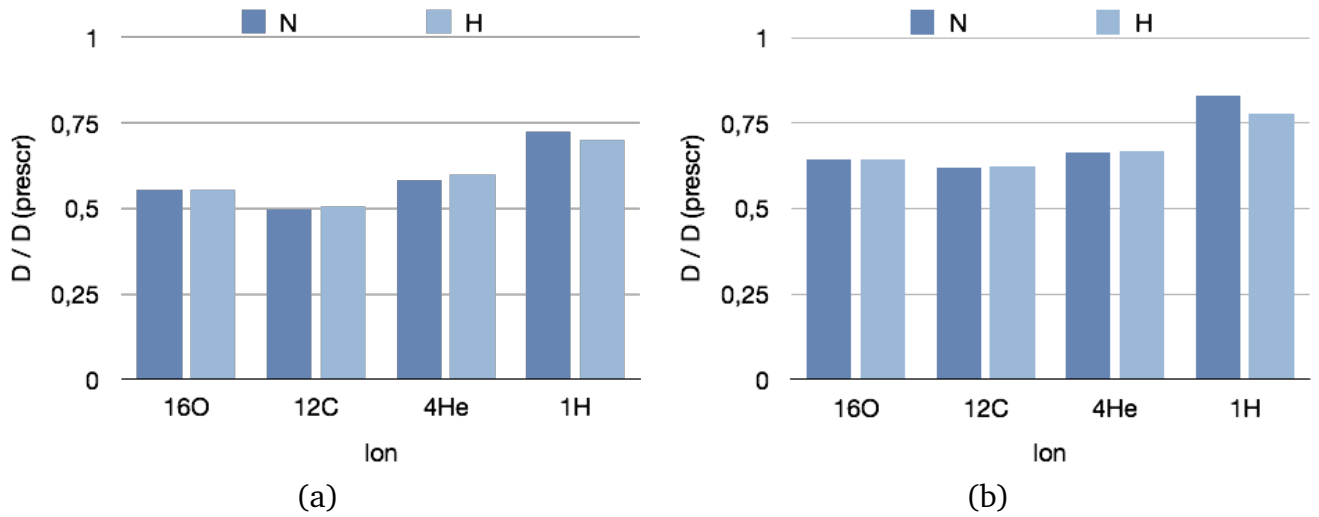

Figure 3.12.: Maximal relative dose received by the brainstem (a) and residual tissue (b) for the plan optimized for a 2 Gy RBE- and OER-weighted dose for a normoxic (N) or partially hypoxic (H) adenoid cystic carcinoma irradiated with ^{16}O, ^{12}C, ^{4}He, or ^{1}H.

The previous section with a model target aimed at estimating the damage to the residual tissue and analyzing the potential benefit of oxygen ions only in the entrance channel of the beam. As mentioned above, not for all the patient plans this information is of a high importance when most of the organs at risk normally do not lie in the beam path. In the analyzed cases of chordoma and ACC the most vital organs were avoided in the beam path. However, for some tumors excluding of OAR or other important structures from the beam path is not possible and the results of the model volume test mentioned above become relevant.

An example of such treatment plan containing the structures also in the beam entrance channel is the prostate cancer. To minimize the damage to the bladder and rectum, the fields are usually selected in the way that the beams do not pass through them. However, this field configuration makes the damage to the hip joints unavoidable. Two examples are given in Figures 3.13(a) (case A) and 3.14(a) (case B). There the geometries, contours of hypoxic regions, and the RBE- and OER-weighted dose distributions in three orthogonal central CT planes are shown. Despite the geometries looking very similar at a first glance, the tumor in case B is almost three times smaller that in case A (52 cm^3 compared to 149 cm^3). It is also slightly more hypoxic (the relative size of normally oxygenated area is 8% smaller than in case A). As can be seen from the axial and coronal planes, for both plans the hip joints are placed exactly in the entrance channels of each of the two beams, and one can expect them to receive a relatively high dose. However, these doses are expected to be different due to the relative position of the hip joints and the tumors. In case B, according to the coronal plane CT image, the geometrical centers of the hip joints are located lower than the one of tumor. Thus, with a given field configuration only few slices of the hip joint are expected to lay in the beam entrance channel, leading to a reduction of the mean dose to the organ. The resulting DVHs for the target, rectum and bladder data for cases A and B for normoxic and hypoxic targets for the prescribed RBE- and OER-weighted target dose of 2 Gy are given in Figures 3.13(b) and 3.14(b), respectively.

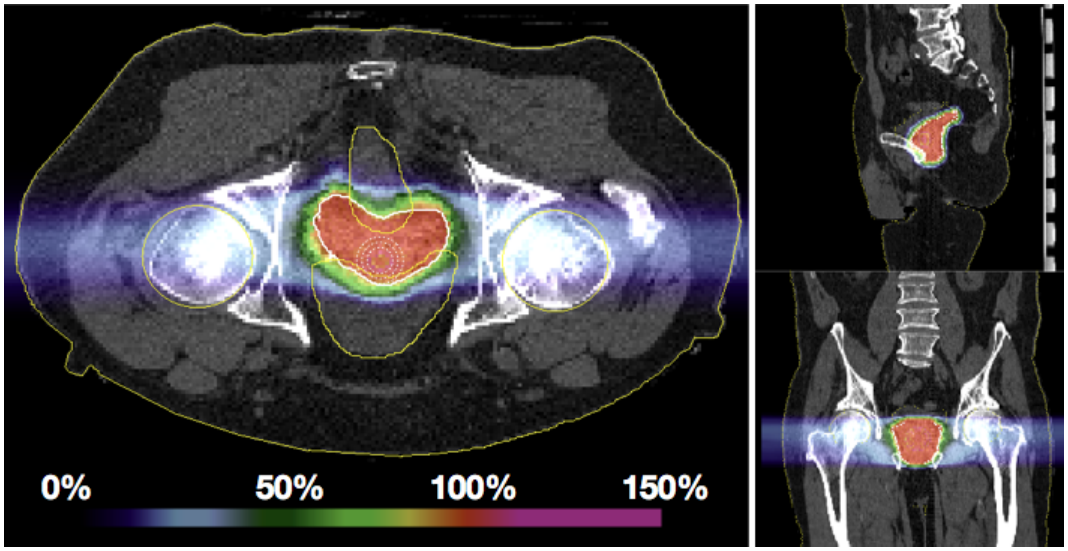

(a)

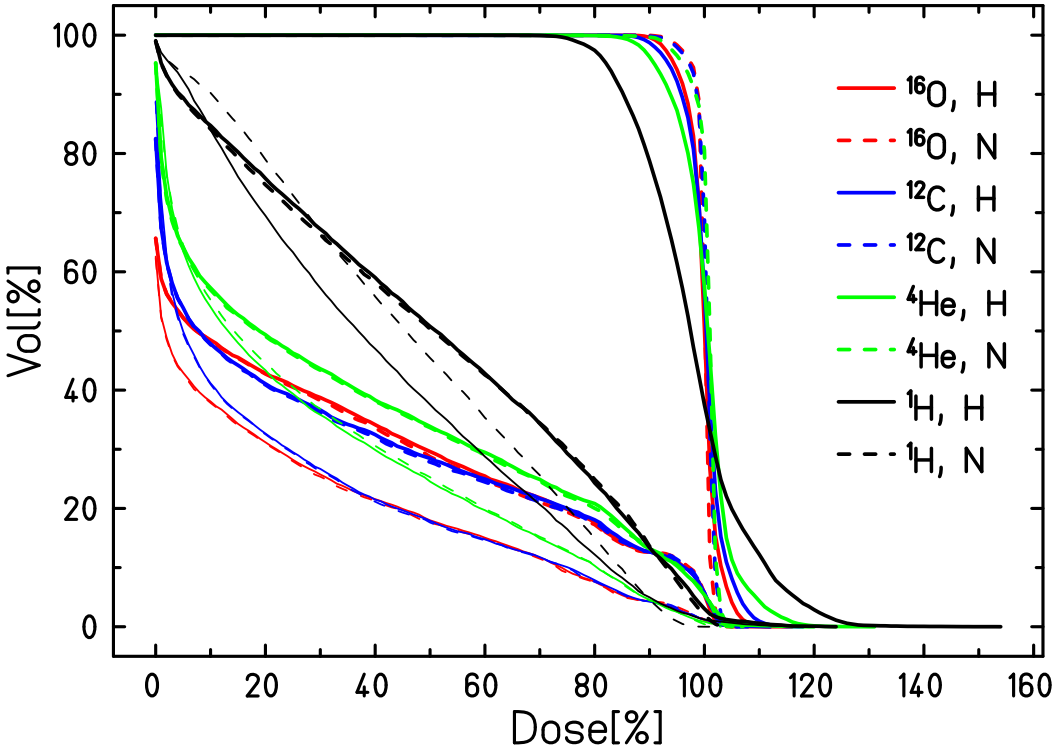

(b)

Figure 3.13.: (a) RBE- and OER-weighted dose distribution for the biologically optimized two-field plan for a partially hypoxic prostate tumor, case A, in axial, sagittal and coronal planes. The tumor is marked with a solid white line, the yellow contours below and above mark the bladder and the rectum, respectively. The two yellow circles on the right and on the left to the tumor outline the hip joints. The three isocentric hypoxic regions in the tumor with 0%, 0.15% and 0.5%pO_2 are marked with dashed white lines. The scale represents the relative dose received by the tissue, compared to the prescribed biological dose of 2 Gy. (b) DVHs for the treatment plan for ^{16}O (red), ^{12}C (blue), ^{4}He (green), and ^{1}H (black) for normoxic (dashed line) and hypoxic (solid line) for a prescribed uniform RBE- and OER-weighted dose of 2 Gy. The data is presented for the target, rectum (bold lines), and bladder (thin line).

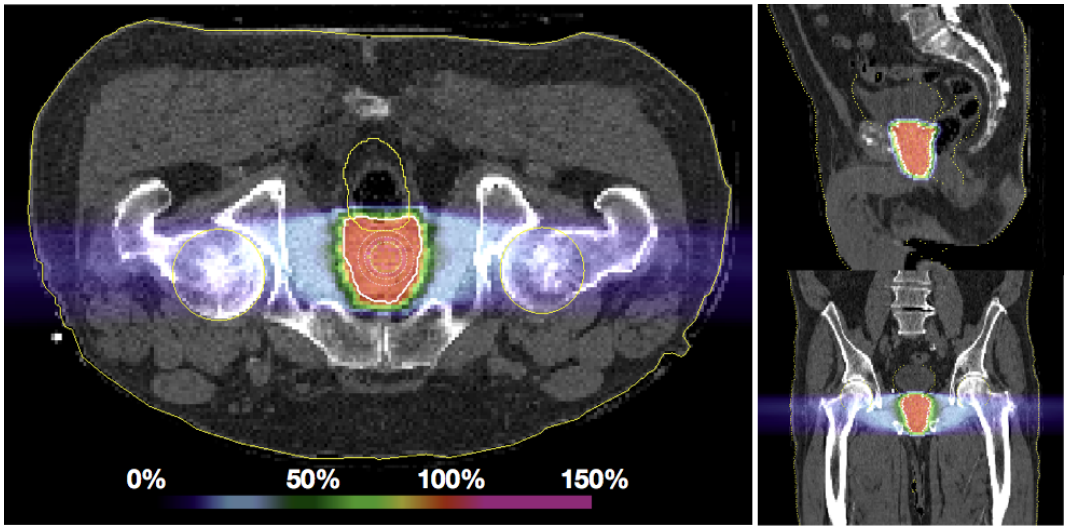

(a)

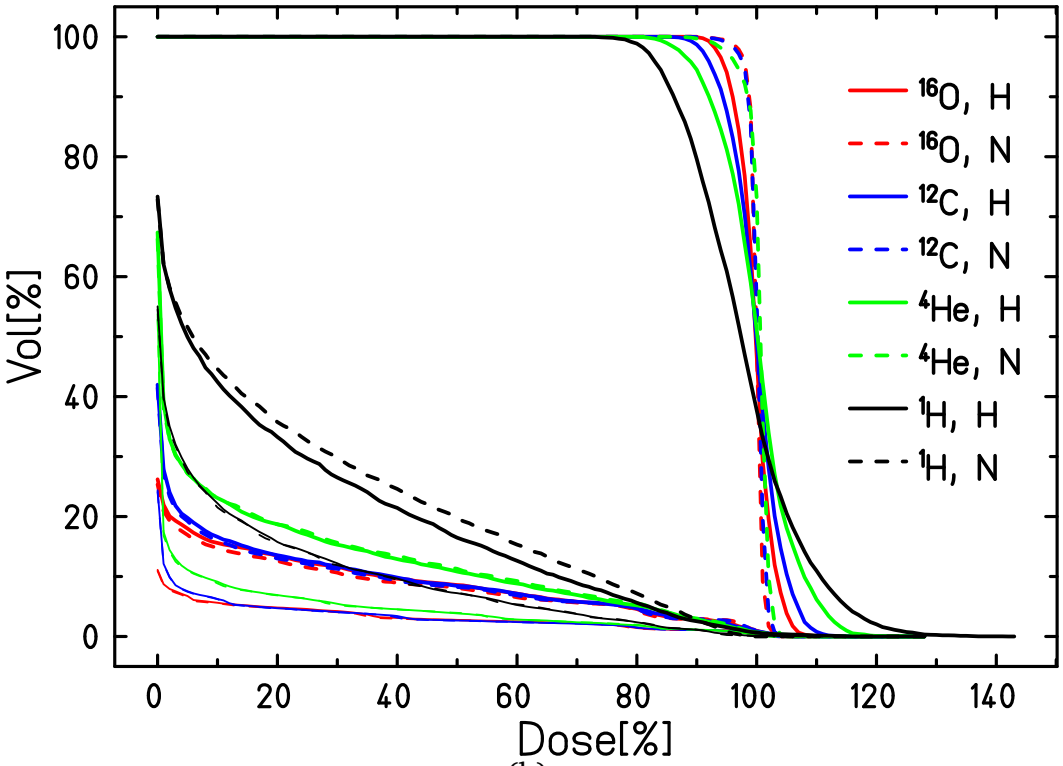

(b)

Figure 3.14.: (a) RBE- and OER-weighted dose distribution for the biologically optimized two-field plan for a partially hypoxic prostate tumor, case B, in axial, sagittal and coronal planes. The tumor is marked with a solid white line, the yellow contours below and above mark the bladder and the rectum, respectively. The two yellow circles on the right and on the left to the tumor outline the hip joints. The three isocentric hypoxic regions in the tumor with 0%, 0.15% and 0.5%pO_2 are marked with dashed white lines. The scale represents the relative dose received by the tissue, compared to the prescribed biological dose of 2 Gy. (b) DVHs for the treatment plan for ^{16}O (red), ^{12}C (blue), ^{4}He (green), and ^{1}H (black) for normoxic (dashed line) and hypoxic (solid line) for a prescribed uniform RBE- and OER-weighted dose of 2 Gy. The data is presented for the target, rectum (bold lines), and bladder (thin line).

To avoid overloading the DVHs with information, the data for the hip joints was excluded from them. Instead, the separate DVH for the left hip joint for case A is given below in Figure 3.15. For the case B the general trend is similar, and thus not given in order to not to overload the chapter with figures. The corresponding numerical values of minimal, maximal, and mean doses to the target and all the mentioned structures for both cases are provided in Tables 3.5.

The trend for the dose coverage of the target remains similar to the cases of the chordoma and the ACC: the plan quality in the presence of hypoxia is least affected in case of heavier ions such as ^{12}C and ^{16}O. As in the previous treatment plans, the standard deviation of the hypoxic target dose coverage remains the lowest for ^{16}O and is 0.05 Gy in case A and 0.06 Gy in case B. The average dose to the rectum and bladder, which were selected for the analysis as the lateral OARs, was not significantly varying between the two oxygenation cases as well. However, the values of the mean doses to these structures vary significantly between the two cases. This can be explained by the different geometries: in case A, there is a large overlap of the tumor with rectum and bladder. Thus, large areas of these structures will receive the dose of an order of the prescribed dose to the target. This leads to the mean doses of ≈0.6 and 0.4 Gy, respectively, for the plans with the heavier ions. In contrast, for the case B this values are ≈0.2 and 0.06 Gy. For both plans there is a very small difference in the mean doses to the OAR, delivered by ^{12}C and ^{16}O. Moreover, in contrast to the plans for chordomas and ACC, this difference is in favor of plans using ^{16}O. However, to draw the final conclusions about the benefit of the latter ion, at this step one should also consider the accuracy of the dose calculation of about 3%, as was concluded from the dose measurements in the previous chapter.

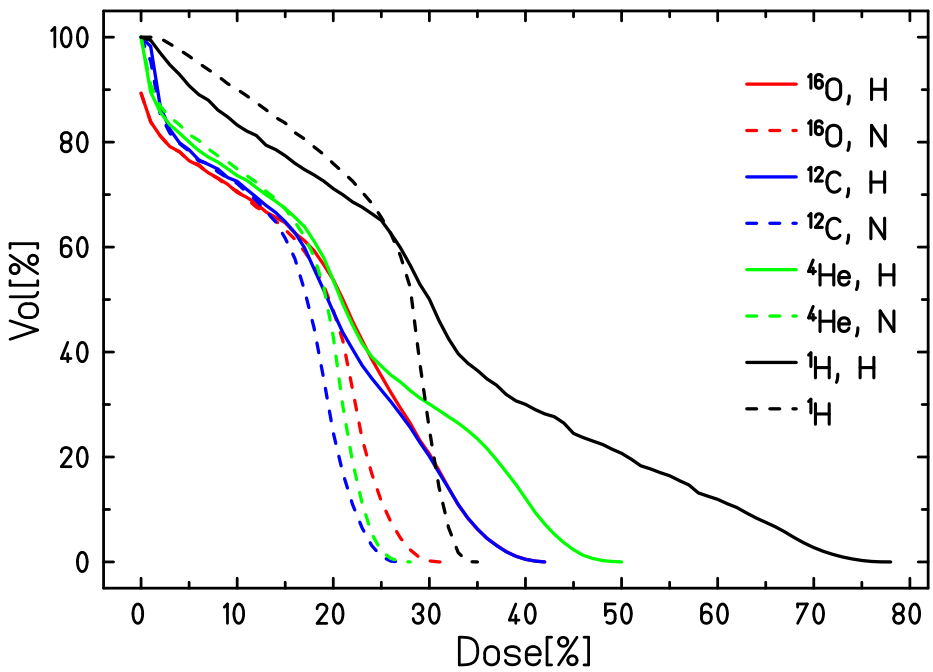

Figure 3.15.: Dose-volume histogram for the treatment plan for ^{16}O (red), ^{12}C (blue), ^{4}He (green), and ^{1}H (black) for normoxic (dashed line) and hypoxic (solid line) prostate tumor for a prescribed uniform biological dose of 2 Gy. The data is presented for the left hip joint laying in the beam path.

Ion	VOI	Case A						Case B					
		Normoxic tumor			Hypoxic tumor			Normoxic tumor			Hypoxic tumor		
		D_{min}/D_p	D_{max}/D_p	D_{mean}/D_p	D_{min}/D_p	D_{max}/D_p	D_{mean}/D_p	D_{min}/D_p	D_{max}/D_p	D_{mean}/D_p	D_{min}/D_p	D_{max}/D_p	D_{mean}/D_p
	Target	0.62	1.05	0.99	0.59	1.13	0.99	0.90	1.05	0.99	0.89	1.12	0.99
^{16}O	Rectum	0	1.04	0.30	0	1.09	0.30	0	1.05	0.09	0	1.09	0.09
	Bladder	0	1.05	0.19	0	1.07	0.20	0	1.04	0.03	0	1.04	0.03
	Hip Joint	0	0.31	0.16	0	0.42	0.19	0	0.21	0.06	0	0.24	0.06
	Residual	0	1.11	0.005	0	1.2	0.006	0	1.09	0.003	0	1.12	0.003
	Target	0.49	1.08	1	0.46	1.17	1	0.89	1.05	1	0.86	1.16	0.99
^{12}C	Rectum	0	1.05	0.29	0	1.12	0.3	0	1.05	0.09	0	1.11	0.09
	Bladder	0	1.06	0.21	0	1.11	0.21	0	1.05	0.03	0	1.05	0.03
	Hip Joint	0	0.26	0.14	0	0.42	0.19	0	0.19	0.05	0	0.24	0.06
	Residual	0	1.12	0.005	0	1.22	0.006	0	1.07	0.002	0	1.16	0.003
	Target	0.60	1.07	1	0.59	1.29	1	0.86	1.06	1	0.79	1.25	1
^{4}He	Rectum	0	1.05	0.35	0	1.18	0.35	0	1.04	0.13	0	1.14	0.13
	Bladder	0	1.03	0.28	0	1.16	0.27	0	1.04	0.05	0	1.04	0.05
	Hip Joint	0	0.28	0.16	0	0.49	0.21	0	0.19	0.06	0	0.30	0.07
	Residual	0	1.07	0.006	0	1.30	0.007	0	1.06	0.003	0	1.27	0.003
	Target	0.74	1.06	0.99	0.66	1.53	0.98	0.85	1.03	0.99	0.74	1.41	0.98
^{1}H	Rectum	0	1.04	0.50	0	1.23	0.50	0	0.99	0.22	0	1.15	0.2
	Bladder	0	0.99	0.47	0	1.19	0.41	0	1.00	0.09	0	1.07	0.10
	Hip Joint	0.01	0.34	0.24	0.01	0.77	0.32	0	0.29	0.13	0	0.40	0.13
	Residual	0	1.06	0.009	0	1.53	0.010	0	1.04	0.005	0	1.41	0.005

Table 3.5.: Minimal (D_{min}), maximal (D_{max}) and average (D_{mean}) relative doses, compared to the planned dose of 2 Gy(RBE,OER) (D_p), in case of irradiating normoxic or partially hypoxic prostate tumor with ^{16}O, ^{12}C, ^{4}He and ^{1}H ions.

The maximal doses received by these rectum and bladder remain the lowest in case of hypoxic tumor when the ^{16}O or ^{12}C ions are used; the difference between these two ions is hard to distinguish within the potential dose calculation uncertainty. For example, in case A the difference between ^{16}O and ^{12}C for the maximal doses is only 1.6% and 3% for the rectum and bladder, respectively. Same trend is relevant for the maximal dose to residual tissue.

Regarding the impact of hypoxia on the dose delivered to the hip joints, a trend somehow similar to the study shown in the previous section, can be distinguished. An example for the case A is illustrated in Figure 3.15. While with normoxic tumors ^{4}He, ^{12}C and ^{16}O deliver the comparable low doses in the the entrance channel and thus perform similarly in terms of the mean dose to the left hip joint (16, 14, and 16% from the prescribed dose of 2Gy, respectively), the picture changes in presence of hypoxia. The difference in the dose between the different ions is shifting the other way around (21, 19 and 19% for ^{4}He, ^{12}C, and ^{16}O, respectively). The effect can be easily noted in the Figure 3.15. Similar trend, but even more pronounced (Table 3.5) is also valid for the maximal dose. According to the tests in the previous section, one can expect the further increase of the difference between the ^{12}C and ^{16}O with increasing size of the hypoxic region. The study with the model target showed the largest effect when more than 80% of the tumor is hypoxic. In this case, however, it is less than 50% and, moreover, the oxygenation is varying inside the region.

3.3.4 Summary

As can be generally concluded from this study, it is impossible to make a general selection of the cases where one can benefit from using ^{16}O ions instead of the lighter modalities. One always has to account for the tissues radiosensitivity, geometry and field configuration to make a proper choice of the ion. As can be seen from the analysis in normoxia for both the idealized geometry and real tumor cases, the use of ^{16}O for normoxic targets is not justified, since it results in increased doses in the entrance channel and the doses to the OARs, both lateral and those in the beam path.

As follows from the idealized geometry tests, the general argument in favor of considering ^{16}O are the relatively low prescribed doses and the presence of large hypoxic parts in the tumor. This can be beneficial in the moderate hypofractionated therapy, when the slightly higher doses of 2.4-4 Gy are given per treatment fraction, in contrast to conventional fractionation with doses of 1.8-2 Gy per fraction [Benjamin et al., 2017].

The high level of hypoxia is often the case for the real tumors, as the recent studies on tumor oxygenation show. The review study of [Janssen et al., 2005] demonstrates that different visualization methods prove the presence of hypoxia in a large number of head and neck cancers; same refers to the prostate tumors [Marignol et al., 2008; Fraga et al., 2015; Rupp et al., 2016]. Another tumor proven to be significantly hypoxic is pancreatic cancer [Erickson et al., 2015; Erkan et al., 2016]. Regarding the examples of numerical data, the study of [Cheney et al., 2014a] investigated the chordoma of the mobile or sacrococcygeal spine patients and revealed

the presence of hypoxic subvolumes of noticeable sizes (≥ 5 cm^3 for regular-sized and ≥ 8 cm^3 for the T2 stage tumors) in 60% of investigated patients. These data underline the relevance of the studies presented here.

However, on the one hand, these studies were limited by the amount of patient data available for calculations, but, on the other hand, they allow outlining another circle for oxygen beam application limitations.

The first conclusion that can be drawn, based on all six analyzed patient cases, is that the main benefit of treatment plans with ^{16}O is mainly the resistance of the plan quality to the presence of different levels of hypoxia. This is an essential argument in fractionated therapy since the locations and sizes of hypoxic volumes are proven to vary between and during the subsequent treatment sessions.

Regarding the mean dose to the lateral OARs, it remains somewhat intermediate, due to the increased portion of fragmentation compared to ^{12}C and reduced scattering, compared to ^{4}He ions. The best result in terms of the mean dose was demonstrated by ^{16}O for both analyzed cases of prostate tumor, where the mean dose was similar or even slightly lower than for ^{12}C plans.

Delivering the lowest possible maximal dose can be crucial in case of serial organs, such as brainstem. The analysis of the maximal dose for all the hypoxic tumors has demonstrated the decrease of this parameter with the increase of ion mass. The significance of the resulting difference is expected to be dependent on the level of target location and oxygenation level. In the analysis with chordoma tumors more pronounced benefit of ^{16}O ions was observed for a more hypoxic tumor.

The study with two cases of ACC did not show a significant difference between ^{16}O and ^{12}C. The reason for a slightly better results achieved with ^{12}C plans can be the field configuration due to which the brainstem is located in the fragmentation tail of one of them. Additionally, according to the analysis presented by [Inaniwa et al., 2017], use of orthogonal fields (which is close to be the case for the analyzed ACC treatment plans) does not allow the most favorable LET distribution inside the target.

Switching to the geometries with more deep-seated targets, such as the prostate cancer, further smears the difference between ^{16}O and ^{12}C. The mean dose to the organs at risk becomes similar for these two ions, while in terms of the maximal doses ^{16}O might be still beneficial, however the corresponding difference is only of order of few percent. This analysis shows that for this particular case the only benefit from using the ^{16}O fields is a slightly better target coverage (2.8% vs. 3.7% for ^{12}C). This is far from being a striking argument in favor of ^{16}O beams. However, for the structures laying in the entrance channel one can expect the slight further decrease of the dose with the further growth of hypoxia contribution, similarly to the effect observed during the studies with idealized target. It should be additionally mentioned, that in both the prostate and ACC cases analyses the respective tumors were significantly different in sizes. However, all the analyzed effects remain similar. To further conclude whether there is a

strong dependency of the doses received by OARs on the tumor size, more treatment planning studies are needed.

Since the real PET data on hypoxia distribution is still not achievable with the needed accuracy, this study remains an assumption. Apart from that, the treatment planning studies, presented in this section, were partially limited by the capabilities of the tool to transfer the realistic, measured hypoxia maps to the studied cases. Despite the modeled hypoxic regions occupying the significant parts of the tumors slices to which they belong, the ratio of the total size of the emulated hypoxic parts to the total volumes of the tumors was not very high. As mentioned above, in reality the hypoxic regions may occupy a drastic central part of the tumor, at the same time having a complicated internal pO_2 distribution. Modeling a more realistic oxygenation distribution that shapes better to the tumor contours requires an updated tool. The development of such tool together with the further tests is beyond the scope of the current work and is left for the further research.

4 Multiple ion treatment planning involving oxygen beams

4.1 Introduction

The treatment planning study in the previous chapter revealed that in the idealized symmetric geometry oxygen ions are the most advantageous in terms of sparing the healthy tissue in the beam entrance channel when the tumor is highly hypoxic. To get the lowest dose to the residual tissue and OAR with the same tumor dose coverage in normoxia carbon or helium ions remain the optimal choice.

The idea of combining different ions to overcome hypoxia is demonstrated in Figure 4.1.

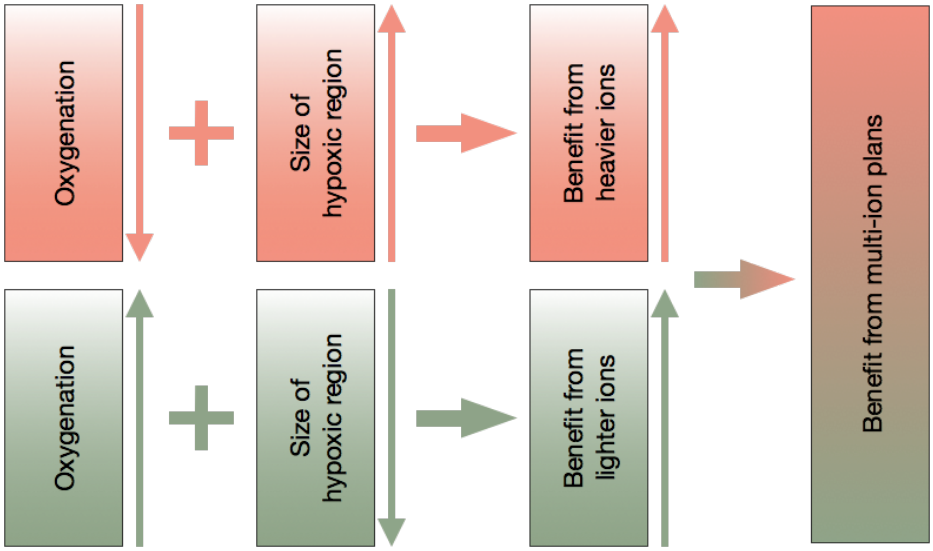

Figure 4.1.: The main idea behind using the multiple-ion treatment planning for overcoming tumor hypoxia: reducing the dose to residual tissue by forwarding the high-LET heavier ions to the hypoxic regions, while covering the remaining normoxic target parts with lighter ions.

The hypoxic parts of the tumor can be irradiated with heavier ions with a higher LET depth distribution: the high ionization density results in a lower OER values and therefore in an increased total biological effect compared to the lighter ionic species. On the other hand, the remaining dose in the normoxic regions can be covered by the lighter ions, which results in less fragmentation and lower RBE values, thus allowing better protection of the surrounding residual tissue and OAR. The simultaneous optimization of several ion fields, considering the physical and radiobiological benefits and disadvantages of each modality, is expected to increase

the quality and flexibility of treatment planning, and would allow exploiting the given ion fields with the optimal plan beyond a pure empirical boost. As previously mentioned, despite several ongoing studies of other groups, this approach specifically for hypoxic tumors was never realized by anybody before.

The immediate rationale for applying a combined plan is the behavior of the single ions in normoxic and hypoxic conditions. For example, if ^{4}He ions deliver the higher dose to the brainstem in case of the two-field irradiation of normoxic chordoma due to their increased lateral scattering as compared to ^{16}O, one should not expect a further improvement of the treatment plan when the tumor hypoxia information added to the optimization. Thus, ^{16}O will remain the better choice for both cases and mixing it with a lighter ion beam will worsen the quality of the plan.

4.2 Materials and methods

4.2.1 TRiP98-multiion-OER

To enable the multiple-ion optimization accounting for hypoxia with TRiP98, two current advanced versions of the TPS were merged. The current production version is capable of carrying out the optimization with multiple-ion fields [Krämer et al., 2014]. The inclusion of hypoxia effect into TRiP98-OER [Scifoni et al., 2013] was done in parallel to the implementation of the multiple-ion species approach and at the moment of the beginning of the current study study TRiP98-OER was able to handle only one ion modality per treatment plan.

Thus, the calculation algorithms related to the OER importing, handling and interpolation, and biological dose calculations were transferred and partially expanded or improved from TRiP98-OER to the production version. This implies:

- modifications of the biological effect calculation to include the OER;
- improvement of the calculation of the dose gradient, driving the optimization by including OER as a driving force for the optimization;
- import of the pO_2 data (the new method is explained in Appendix C; not part of the work presented here).

4.2.2 RBE- and OER-weighted dose calculation

The difference in the biological dose calculation, compared to the algorithm used in [Scifoni et al., 2013] is accounting for the mixed radiation field created by not only one, but several primary ions for each raster spot and depth bin. In the recent version the additional summation through all the primaries was introduced in the biological dose calculation step.

For a set of primary particle beams traveling in water, the equation 1.2 for the absorbed dose can be rewritten as

$$D(Gy) = C \times F_{\eta}(\mathrm{mm}^{-2}) \times \overline{LET}\left(\frac{\mathrm{MeV}}{\mathrm{g\ cm}^{-2}}\right) \tag{4.1}$$

where F_{η} is a particle fluence, $C = 1.602189 \times 10^{8}$, and $\overline{LET}$ is the dose-averaged linear transfer resulting from the contributions of all the primary beams, defined as in Equation 2.4.

According to the low-dose approximation, introduced in [Krämer and Scholz, 2006], the biological response (cell survival) can be obtained as

$$-\ln S = \begin{cases} D\,(\beta D + \alpha), & D \leq D_{cut} \\ D_{cut}\,(\beta D_{cut} + \alpha) + (D - D_{cut})S_{max}, & D > D_{cut} \end{cases} \tag{4.2}$$

where D_{cut}, S_{cut} are the LQL parameters controlling in LEM the transition to exponential dose-effect relation at high doses, and $s_{max} = 2\beta \cdot D_{cut} + \alpha$ is the corresponding slope. In this equation, α and β represent the dose-weighted averages for radiobiological coefficients for the mixed field calculated based on the knowledge of α_l and β_l of each of the mixed field components.

Considering the effect of hypoxia by introducing the OER as a dose-modifying factor [Scifoni et al., 2013; Tinganelli et al., 2015], i.e.

$$D' = \frac{D}{OER}, \tag{4.3}$$

with the oxygen enhancement ratio OER defined as in equation 2.8, but considering the contributions from all the primary beams in the dose-averaged LET calculation, the equation 4.2 for the biological effect can be rewritten as

$$-\ln(S) = \begin{cases} \dfrac{D}{OER}\left(\beta\,\dfrac{D}{OER} + \alpha\right), & D \leq D_{cut} \\ \dfrac{D_{cut}}{OER}\left(\beta\,\dfrac{D_{cut}}{OER} + \alpha\right) + (D - D_{cut}) \cdot s_{max} & D > D_{cut} \end{cases} \tag{4.4}$$

and the biological dose can be calculated as

$$D_{bio} = \begin{cases} \sqrt{-\ln S\ /\ \beta_X + (\alpha_X\ /\ 2\beta_X)^2} - (\alpha_X\ /\ 2\beta_X), & D \leq D_{cut} \\ (-\ln S + \ln S_{cut})\ /\ S_{max} + D_{cut} & D > D_{cut} \end{cases} \tag{4.5}$$

with α_X and β_X being the photon response parameters.

The biological dose optimization in TRiP98 is usually done using gradient-based methods, so when accounting for the OER effect, the gradients have to be be modified accordingly [Tinganelli et al., 2015]:

$$\nabla\alpha'\left(\overline{\mathrm{LET}}, pO_2\right) = \frac{\nabla\alpha}{\overline{\mathrm{OER}}\left(\overline{\mathrm{LET}}, pO_{2,i}\right)} - \alpha\frac{\nabla\overline{\mathrm{OER}}\left(\overline{\mathrm{LET}}, pO_2\right)}{\overline{\mathrm{OER}}^2} \tag{4.6}$$

$$\nabla\sqrt{\beta'}\left(\overline{\mathrm{LET}}, pO_2\right) = \frac{\nabla\sqrt{\beta}}{\overline{\mathrm{OER}}\left(\overline{\mathrm{LET}}, pO_2\right)} - \sqrt{\beta}\frac{\nabla\overline{\mathrm{OER}}\left(\overline{\mathrm{LET}}, pO_2\right)}{\overline{\mathrm{OER}}^2} \tag{4.7}$$

In the TRiP98-OER version the calculation of the second term was omitted as considered negligible. In the updated multiple-ion version the second term was added, with $\nabla\overline{\mathrm{OER}}$ calculated based on its definition as in equation 2.8.

4.3 Results and discussion

4.3.1 Dose redistribution for unevenly oxygenated tumors

This subsection describes the basic test of the multi-ion optimization method for hypoxic target. For this study, a geometry similar to the one used in the previous chapter in the study with hypoxic tumors was emulated. A cubic water target volume of 40 × 40 × 60 mm was placed in the center of a water CT cube of 200 × 200 × 160 mm (CT voxel size was chosen as 2 mm in x- and y-directions and the slice distance as 2 mm as well). The central target region of 28 mm ($66 \leq z < 94$ mm) was chosen to have the oxygenation level of 0.5% pO_2. The RBE tables for the CHO cell line (Appendix A) were used for the biological optimization. The optimization was performed for the two pairs of opposite fields (^{16}O + ^{16}O and ^{4}He + ^{4}He, couch angles 180 and -180 degrees for each pair of fields). The plan was optimized for a uniform RBE- and OER-weighted dose of 6.5 Gy that would correspond to the target survival of 10% for the given cell line. No additional constraints were applied. In total, 19 energies of ^{16}O beams, varying from 280.29 MeV/u to 188.27 MeV/u, and 19 energies of ^{4}He beams, varying from 124.78 to 85.64 MeV/u, were used.

The results of the kill-painting optimization with multiple fields are presented in Figure 4.2. Here, the central cuts of the dose and dose-averaged LET cubes in XZ plane are given, including the resulting distributions and the dose contributions from each ion. ^{16}O ions dominate in the central hypoxic part while the contribution of ^{4}He is more significant in the peripheral regions of the target. From the 4.2(a) one can immediately note the difference in the lateral scattering of the beams: the lateral dose fall-off caused by the higher portion of ^{16}O beams to the central part is lower than the lateral fall-off generated in the side areas of the target, where the contribution of ^{4}He ions is more significant.

For providing more quantitative information, the one-dimensional cuts from the survival, dose and dose-averaged LET cubes along the central line are given in Figures 4.3. Figures 4.3a and

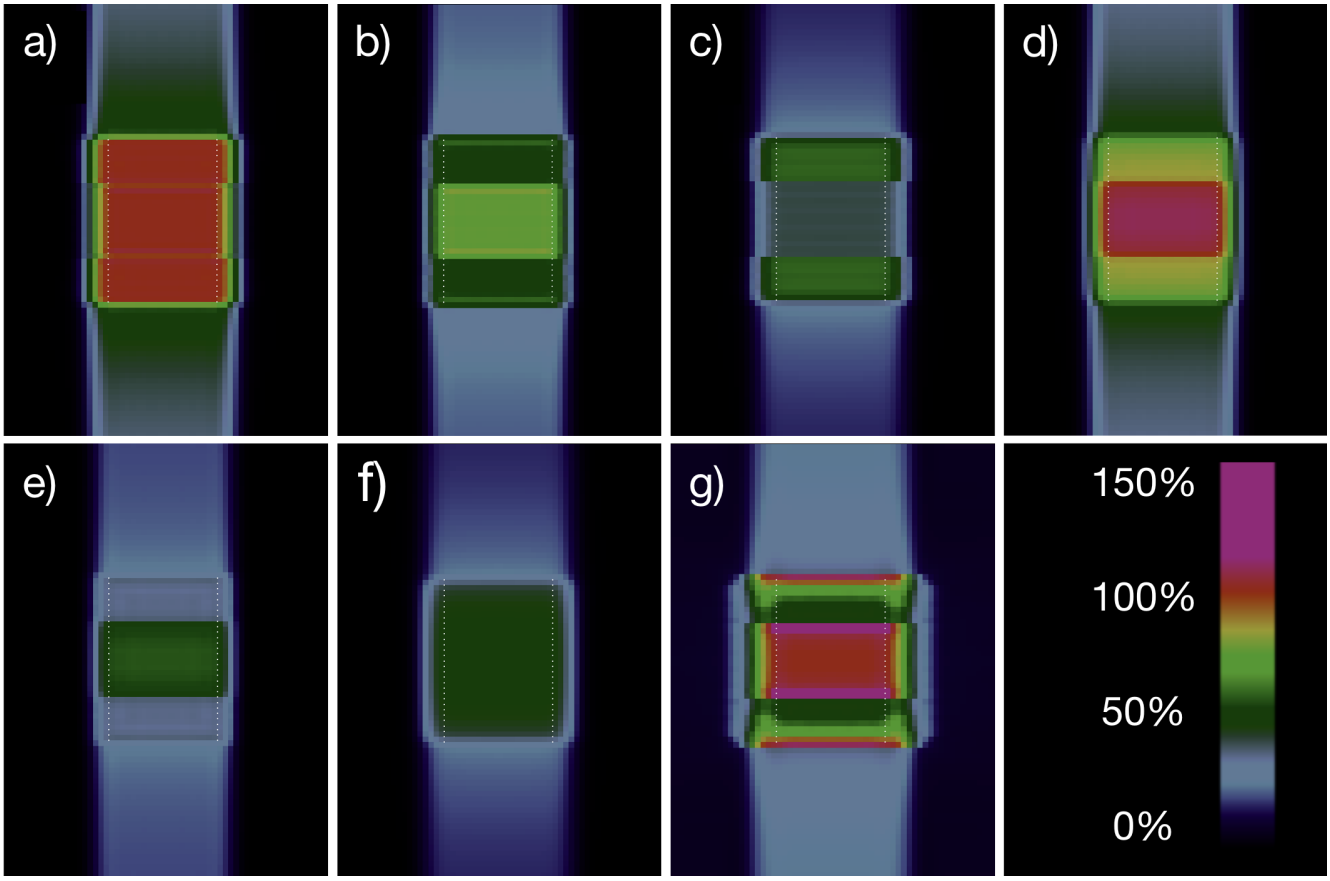

Figure 4.2.: Results of the plan optimization with four opposite fields (^{16}O+^{16}O and ^{4}He+^{4}He for a uniform survival of 10% in the target. The oxygenation distribution was modeled as follows: for $66 \leq z < 94$ mm pO_2 = 0.5% and 21% for the rest of the volume. (a) 2D RBE- and OER- weighted total dose distribution in XZ plane, (b), (c) - contributions of ^{16}O and ^{4}He fields, (d) 2D total absorbed dose distribution in XZ plane, (e), (f) - contributions of ^{16}O (b) and ^{4}He fields, respectively, (g) - the resulting dose-averaged LET distribution. The 100% of the color scale correspond to the dose value of 6.5 Gy for Figures (a)-(f) and 60 keV/μm for (g).

4.3b demonstrate the resulting total survival in the target of 10% and the corresponding RBE- and OER-weighted (6.5 Gy) and absorbed doses at the central line of the emulated geometry along the beam direction. Similar to the single-ion plans, mentioned in the previous chapter, the inhomogeneities arise due to the drastic decrease in oxygenation between the neighboring voxels; however, these fluctuations do not exceed the values of 9.5% of the absolute values, and the overall quality of optimization is acceptable.

The separate contributions of each ion to the physical and biological doses are shown in Figures 4.3(c) and 4.3(d), respectively. As can be seen from Figure 4.3(c), in the normoxic part of the target the contribution of ^{4}He is more significant than for ^{16}O (up to $\approx$ 3.25 Gy compared to $\approx$ 2.5 Gy), while in the central hypoxic part the preference is given to ^{16}O ($\approx$ 4 Gy compared to $\approx$ 3.25 Gy).

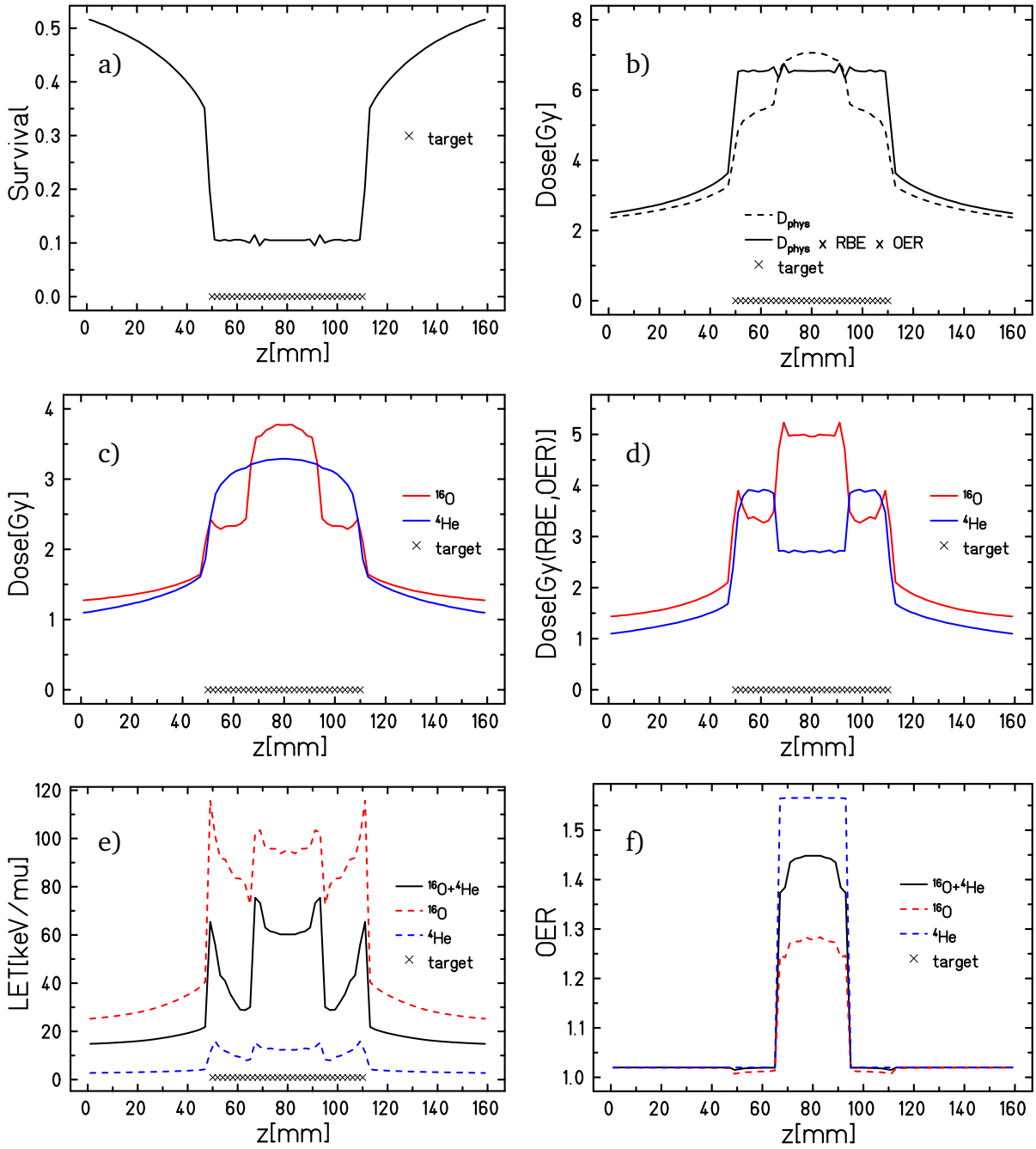

Figure 4.3.: Results of the plan optimization with four opposite fields (^{16}O+^{16}O and ^{4}He+^{4}He) for a uniform target survival of 10%. The oxygenation distribution was modeled as follows: for 66 $\leq z <$ 94 mm pO_2 = 0.5% and 21% for the rest of the volume. The profiles are extracted from the corresponding calculated cubes at the central lines (x = 100, y = 100) along z direction. (a) Total cell survival. (b) Total absorbed (dotted line) and RBE-weighted (solid line) dose profiles. (c) Absorbed dose contributions from pairs of fields: red - ^{16}O+^{16}O, blue - ^{4}He+^{4}He. (d) RBE- and OER-weighted contributions from pairs of fields: red - ^{16}O+^{16}O, blue - ^{4}He+^{4}He. (e) Dose-averaged LET profile in comparison with similar plans optimized for two opposite fields either of ^{16}O (dashed red line) or ^{4}He (dashed blue line). (f) Corresponding comparison of OER distributions calculated according to the model approach of [Tinganelli et al., 2015]. For all the figures the target area is marked with crosses.

This will result in a well-pronounced ^{16}O boost in the biological dose to the hypoxic region (Figure 4.3d), while the contributions to the dose distribution in the normoxic parts will become almost equal with a slight preference given to ^{4}He ions. This optimization yields a dose-averaged LET profile shown in Figure 4.3e. Here, an additional comparison with the dose-averaged LET profiles of the single-ion ^{16}O and ^{4}He plans is given. As can be seen, the multiple-ion optimization allows one to noticeably increase the $\overline{\text{LET}}$ up to 60-75 keV/μm in the hypoxic part, compared to the planning performed only with light ions (^{4}He) where the $\overline{\text{LET}}$ distribution is almost uniform and does not exceed 15 keV/μm. At the same time, the unnecessarily high $\overline{\text{LET}}$ in the normoxic regions is avoided, compared to the ^{16}O plan. Thus, the combined plan allows achieving the $\overline{\text{LET}}$ distribution better shaped to the oxygenation distribution.

As can be seen from the Figure 4.3f, the corresponding OER values in the central hypoxic part are 1.55, 1.28 and 1.45 for ^{16}O, ^{4}He and their combination, respectively. In contrast to the slightly rounded OER distribution for the ^{16}O and combined plans, the OER distribution for the ^{4}He beams plan has a rectangular shape. This means that the OER values in this region reach their maximum predicted by the model for this particular level of oxygenation and no reduction in the dose due to the LET effect occurs at all. Here one should keep in mind, that in the model of [Scifoni et al., 2013; Tinganelli et al., 2015] the OER-LET dependency on the particle type was not discussed, but found negligible. The model study proposed by [Strigari et al., 2017] demonstrated that for the lighter particles such as ^{4}He the OER decrease might occur at the lower LET values; thus, updating of the current OER look-up tables in TRiP98 according to their model might slightly affect the shape of the OER-z distribution. However, this study is beyond the scope of the presented work.

When no constraints except the prescribed target dose for the planning are imposed, the optimization aims only at achieving the desired uniform dose distribution in the target. Thus, when no additional driving forces in the optimization and no planning constraints are introduced, the system is expected to calculate the plan giving similar preferences to each primary beam that is included. No actual field redistribution occurs, but the delivered dose is instead split between the beams. Thus, as mentioned before, it might worsen the dose distribution in residual tissues or organ at risk, if one of the included ions performs noticeably better than the other. However, if the geometry is more complex and implies organs at risk or just the irregular target shape, different ions might perform differently in neighboring target regions, the quality of the combined plan might be better compared to the corresponding single-ion plans.

4.3.2 Comparison with single-ion optimized plans

The patient study presented in this section aims at the comparison of the planning performed with the combination of ^{16}O with ^{4}He with their corresponding single-ion plans. For this study, a medium-sized skull base chordoma with the volume of $\approx$ 133 cm^3 was chosen. In contrast to the chordoma plan analyzed in the previous chapter, for this case, the tumor is slightly more wrapped around the brainstem. The field configuration, preserved from the original plan (couch

angles were set to 100 and -100 degrees) makes the brainstem lay partially in the fragmentation tail of one of the two almost opposite fields. For the treatment planning tests, the values of FWHM were selected as 5 mm for ^{16}O beams and 7 mm for ^{4}He beams. The distance between the subsequent peak positions was kept 3 mm for all the fields in all plans. The raster scanner steps in *x*- and *y*-directions were set to 2 mm for the ^{16}O plans, 3 mm for the ^{4}He plans and 4 mm for each ion field in the combined plans. The OAR constraint was transferred from the original plan, where the maximal dose fraction for the spinal cord was set to 0.55 with a weighting factor of 0.8. Apart from that, there were no differences in other plans parameters and optimization algorithms, compared to the patients' study from the previous chapter.

4.3.2.1 Normoxic target

The central axial, coronal and sagittal planes of the resulting RBE-weighted dose cube for the two-fields ^{16}O plan optimized for a normally oxygenated skull base chordoma are given in Figure 4.4.

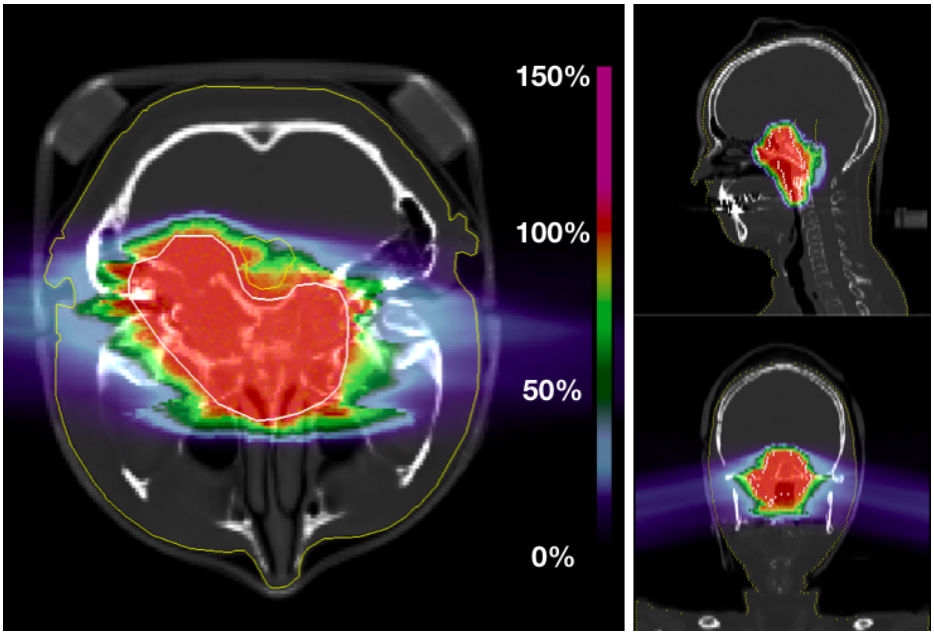

Figure 4.4.: Biologically optimized two-field ^{16}O plan for a normally oxygenated skull base crordoma. The three corresponding orthogonal central CT cuts are are shown. The tumor is marked with a solid white line, the inner yellow line outlines the brainstem, the outer yellow line - the contour of the patient's head. The color scale represents the relative dose received by the tissue, compared to the prescribed RBE-weighted dose of 2 Gy.

The dose cube cuts for the ^{4}He plan are not presented here since the visual difference is not significant between them and the ones for the ^{16}O plan on this scale. However, it is important to note that from the geometry of the tumor it follows that in case of the ^{16}O plan, one part of the brainstem receives a noticeably higher dose compared to the ^{4}He plan due to the significant portion of fragmentation. However, in case of ^{4}He, another part of the brainstem might be at

risk when the higher doses are applied, due to the scattering of the beam coming from another direction.

For the same target, the multiple-ion optimization was performed with two pairs of ^{16}O and ^{4}He ion fields coming from the same angles. The resulting total RBE-weighted and physical dose distributions at the axial plane together with the corresponding contributions from each of the ions are given in Figure 4.5. Both ^{16}O and ^{4}He deliver the RBE-weighted dose of ≈1.2 Gy (60% from the prescribed dose), which corresponds to the physical doses of ≈0.2 and ≈0.4 Gy, accordingly, resulting in a uniform total RBE-weighted dose of 2 Gy in the target. This result is consistent with the multiple ion tests with a C-shaped target 'wrapping' the OAR demonstrated by [Krämer et al., 2014], where the partial doses contributions from each ion inside the target were similar.

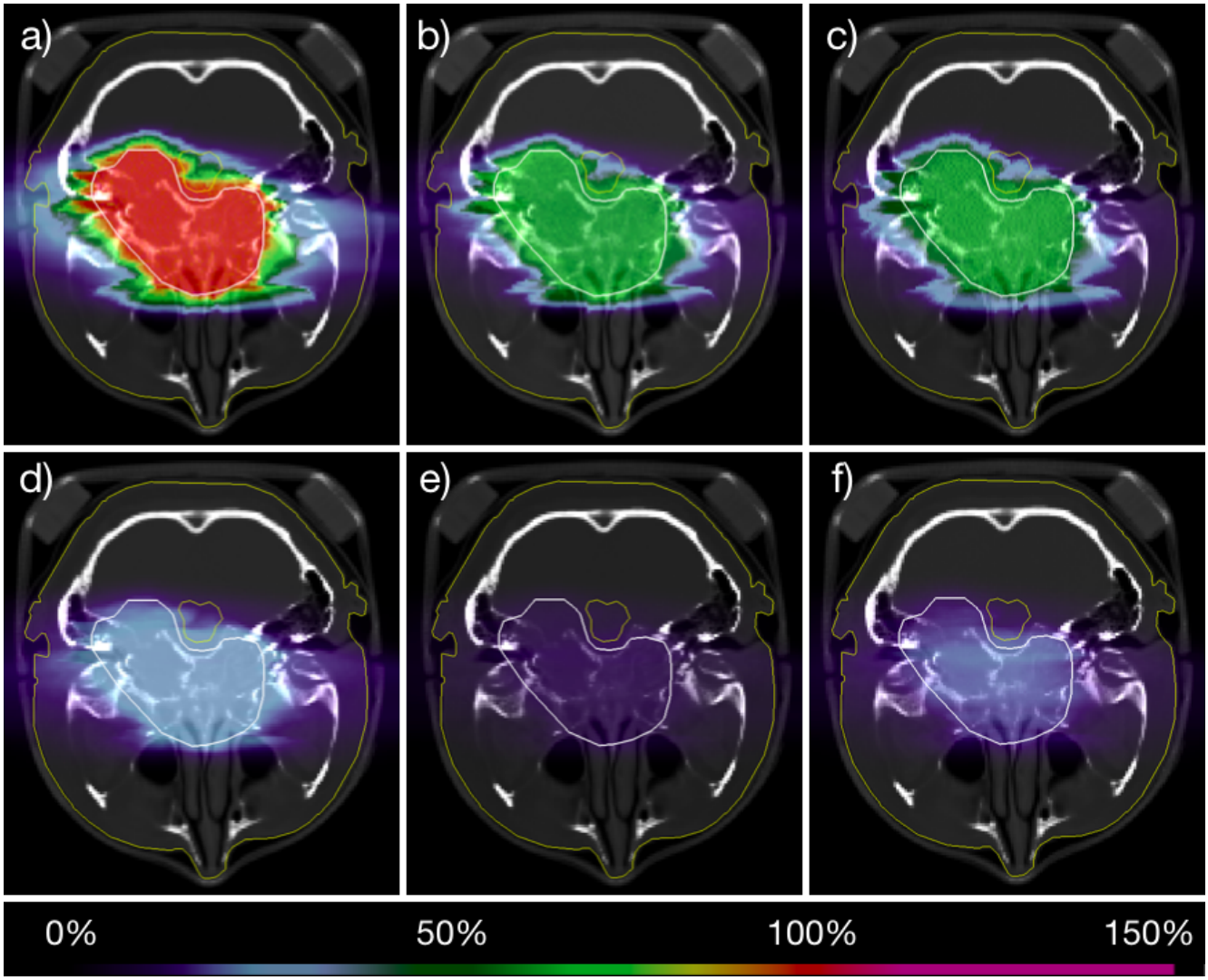

Figure 4.5.: Biologically optimized four-field ^{16}O+^{4}He plan. The chordoma and brainstem are marked with white and yellow lines, respectively. The scale represents the relative dose received by the tissue, compared to the prescribed RBE-weighted dose of 2 Gy. (a) - total RBE-weighted dose, (b) and (c) - ^{16}O and ^{4}He contributions, (d) - total absorbed dose, (e) and (f) - ^{16}O and ^{4}He contributions.

The zoom-in of the dose distribution in the brainstem for two single-ion plans of ^{16}O (Figure 4.4), ^{4}He and the multi-ion plan (Figure 4.5) are given in Figures 4.6(a), (b), and (c), respectively. One can notice that applying the mixed modality field leads to the decrease of the dose received by the brainstem compared to the pure ^{16}O plan: the ratio of the 'red' high dose areas to the 'green' and 'blue' low dose areas becomes less due to the 'dilution' of one field with another. Thus, the fragmentation in the upper part of the brainstem is reduced by partial irradiation with ^{4}He field, while the potential effect of scattering in the lower part might be decreased by the presence of ^{16}O ions.

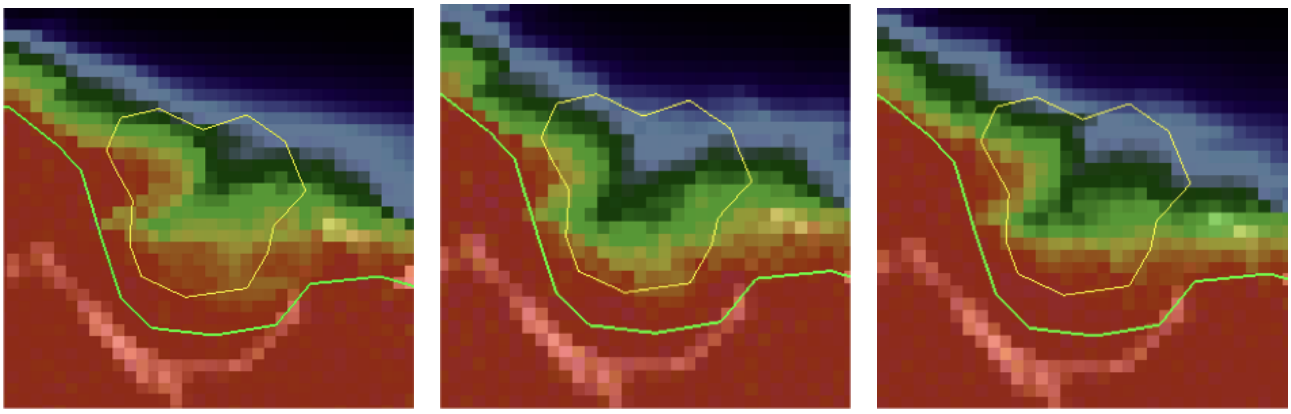

(a) (b) (c)

Figure 4.6.: RBE-weighted dose distribution at the central CT cut inside the brainstem (yellow contour) for the (a) ^{16}O plan, (b) ^{4}He plan, and (c) combined four-field ^{16}O + ^{4}He plan. The color scale is the same as in Figure 4.5.

The outcome of the three tests is summarized in Figure 4.7 showing the DVHs for the target, brainstem and residual tissue for each of the three plans. The corresponding numerical values of the minimal, maximal and mean relative doses received by the target, brainstem, and residual tissue are given in Table 4.1. According to the DVH, the dose coverage of the target is similar for all the three plans. Despite the differences in the minimal and maximal doses to the target, the standard deviation of mean dose values is less than 2% (not given in the Table). This means that only a few voxels out of the total tumor volume would receive the decreased or increased dose; thus, this difference between the plans is not sufficient. At the same time, as can be seen from the values presented in Table 4.1, applying the mixed field leads to the reduction of the mean dose to the brainstem by 4.9% and by 12.7% compared to the single-ion ^{4}He and ^{16}O plans, respectively. The dose to the residual tissue is generally very low since for its calculation all the CT voxels are taken into account; however, it is also reduced by 4.3% compared to both single-ion plans. The maximal doses to the brainstem and residual tissue remain intermediate. Applying the combined field reduces the maximal dose to the brainstem by 2.6% compared to the plan with ^{16}O ions, but worsens it for 2% compared to the ^{4}He plan. Regarding the residual tissue, the maximal dose is reduced for 11.6% compared to the ^{16}O plan and is 3.7% higher compared to the plan optimized for ^{4}He ions. These 'negative' differences in the maximal doses

are both less than 5% and are lower than in another case of chordoma, analyzed in the previous chapter; however, the decrease of the mean dose to the brainstem is noticeable.

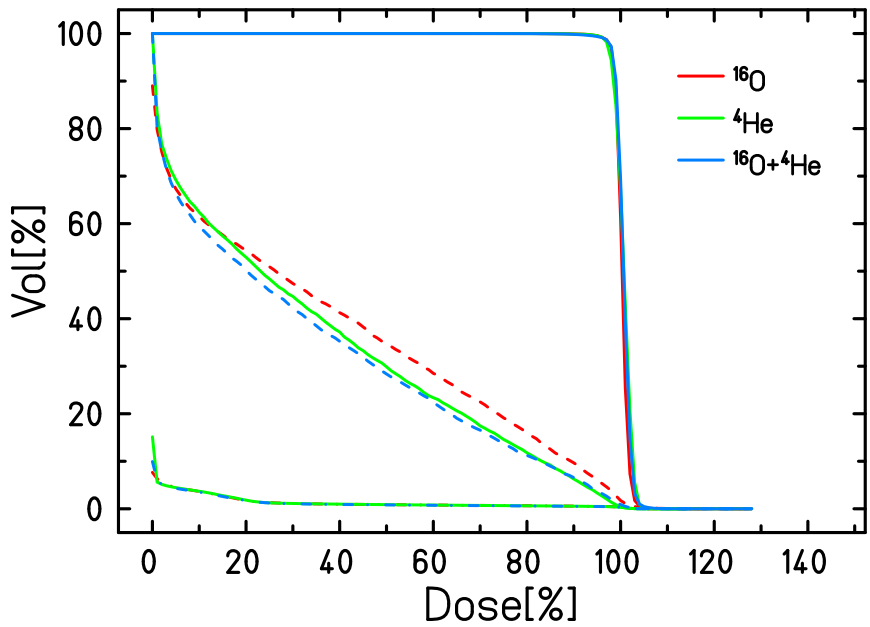

Figure 4.7.: Dose-volume histogram comparison for the two-fields plans of ^{16}O (red), ^{4}He (green) and a four-field combined plan ^{16}O + ^{4}He (light blue), optimized for a uniform RBE-weighted dose of 2 Gy in a normally oxygenated skull base chordoma. Solid lines correspond to the DVHs for the target, dashed lines - for the brainstem, dot-dashed - for the residual tissue.

Ion type	VOI	$D_{\mathrm{min}}/D_{\mathrm{p}}$	$D_{\mathrm{max}}/D_{\mathrm{p}}$	$D_{\mathrm{mean}}/D_{\mathrm{p}}$
^{16}O	Target	0.81	1.15	1
	Brainstem	0	1.10	0.36
	Residual	0	1.29	0.014
^{4}He	Target	0.69	1.10	1.01
	Brainstem	0	1.07	0.33
	Residual	0	1.10	0.014
^{16}O + ^{4}He	Target	0.58	1.12	1.01
	Brainstem	0	1.07	0.31
	Residual	0	1.14	0.013

Table 4.1.: Minimal (D_{min}), maximal (D_{max}) and average (D_{mean}) relative doses, compared to the planned target dose of 2 Gy(RBE) (D_{p}), received by the target, brainstem and residual tissue in case of irradiating the normally oxygenated skull base chordoma with two fields of ^{16}O, ^{4}He, or their four-field combination.

4.3.2.2 Hypoxic target

For the estimation of the impact of the location and/or the size of the hypoxic area on the quality of the multi-ion plan, two tests assuming the different oxygenation distributions inside the target were carried out.

For the first test, one relatively small localized ellipsoid hypoxic region, occupying about 11% of the total target volume, was emulated, as shown in Figure 4.8(a), where the CT slice 58 out of 114 is demonstrated. In total, four oxygenation levels, concentrically decreasing in spherical shells, were modeled inside the target: 21%, 0.5%, 0.15%, and 0% pO_2. For the second test, a noticeably larger (approximately 31% of the target) and a more extended region was emulated. In this case, the target also had in total four levels of oxygenation. Figures 4.8(b) and 4.8(c) demonstrate the corresponding pO_2 distributions at the CT slices 56 and 59 out of 114. For each test, the total sizes of each oxygenation region and their ratios to the total target volume are summarized in Table 4.2.

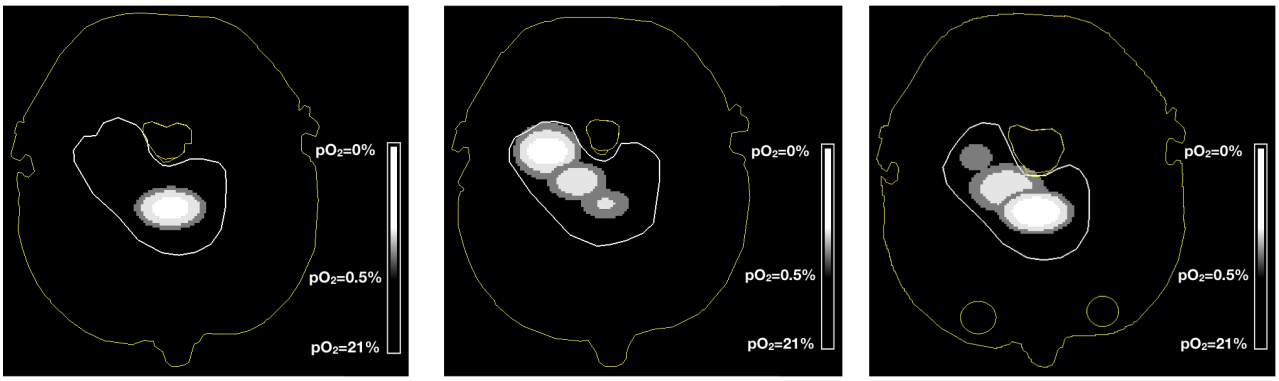

(a) (b) (c)

Figure 4.8.: Emulated hypoxia distributions for the tests with skull base chordoma. The outer yellow line corresponds to patient's head contour, the inner yellow lines marks the brainstem, and the white line marks the tumor contour. (a) First test - a relatively small ellipsoid region with three levels of oxygenation: 0%, 0.15% and 0.5% pO_2. Slice 58 out of 114 is shown. (b), (c) Second test - a larger spread region with three levels of oxygenation: 0%, 0.15% and 0.5% pO_2. Slices 56 and 59 out of 114 are shown, respectively.

The results of the multi-ion optimization for each of the two cases of target oxygenation (further denoted as scenario 1 and scenario 2, respectively) are given in Figures 4.9 and 4.10, respectively. Together with the total RBE- and OER-weighted and absorbed dose distributions at the central CT slice, the corresponding contributions of each ion are given. In both cases of oxygenation, the optimization does not worsen the uniformity of the RBE- and OER-weighted dose distributions in the target (Figures 4.9(a) and 4.10(a)) compared to the single-ion plans. The mean dose to the target remains 2 Gy with a standard deviation of 2.9% and 4.1% for scenarios 1 and 2, respectively, while the deviations for the ^{16}O plans are 2% and 2.8%, and for

Table 4.2.: Parameters of the hypoxia maps generated for the multi-ion tests. Total volume stands for the total volume of the target. The sum volumes of equally oxygenated tumor subvolumes and their ratio to the total tumor volume are given in the last two columns.

Test	Total volume, cm^3	pO_2. %	Volume, cm^3	% of the total volume
1	133.33	0	3.49	2.6
		0.15	5.03	3.8
		0.5	6.53	4.9
		21	118.27	88.7
2	133.33	0	7.55	5.7
		0.15	14.76	11.1
		0.5	19.40	14.6
		21	91.61	68.6

^{4}He plans are 3.6% and 5.4%, respectively. The small inhomogeneities in the tumor coverage are the results of the drastic pO_2 changes and should be not the case for the treatment plans with realistic hypoxia maps, where pO_2 distribution is expected to be smoother.

For both scenarios, the trend in the biological dose delivered by different primaries is similar to the test with the idealized geometry. The ^{16}O ions dominate in the hypoxic parts of the tumor (Figures 4.9(b) and 4.10(b)) by delivering the RBE- and OER-weighted dose boosts in the rage of 1.8-2 Gy depending on the position inside the hypoxic region. At the same time, the contribution from ^{4}He fields is almost negligible there (Figures 4.9(c) and 4.10(c)). As can be seen from the partial contributions to the absorbed dose, the dose distributions produced by ^{4}He fields (Figures 4.9(f) and 4.10(f)) resemble the ^{4}He contribution to the normoxic multi-ion plan (Figure 4.5(f)) and are relatively uniform. Delivered to the hypoxic areas, such doses will lead to the cell 'underkill' depending on the level of OER, similar to the one shown in Figure 3.5. In contrast, the contributions of ^{16}O fields in both scenarios demonstrate the pronounced boost up to ≈0.5 Gy in the absorbed dose in the hypoxic areas (Figures 4.9(e) and 4.10(e), that will compensate the absence of the 'helium dose.' Thus, the TPS is 'excluding' the lighter ion (in this study, ^{4}He) and performs the kill-painting optimization with a heavier modality to achieve the higher LET and, consequently, lower OER values in hypoxic regions.

The dose-averaged LET distributions at the central CT slices for each of the two scenarios in hypoxia are given in Figures 4.11(a) and (b), respectively. As can be seen from both figures, the highest LET values up to 75 keV/μm are reached in the hypoxic regions, while the remaining values do not exceed 40 keV/μm. As follows from Figure 1.10, achieving this level of LET distribution will lead to the 1.3-, 1.2-, and 1.13-fold reduction of OER values in the regions with pO_2 = 0%, 0.15%, and 0.5%, respectively. There are few more regions, apart from the hypoxic areas, mainly in the tops of the cuts, where the LET exceeds its average values.

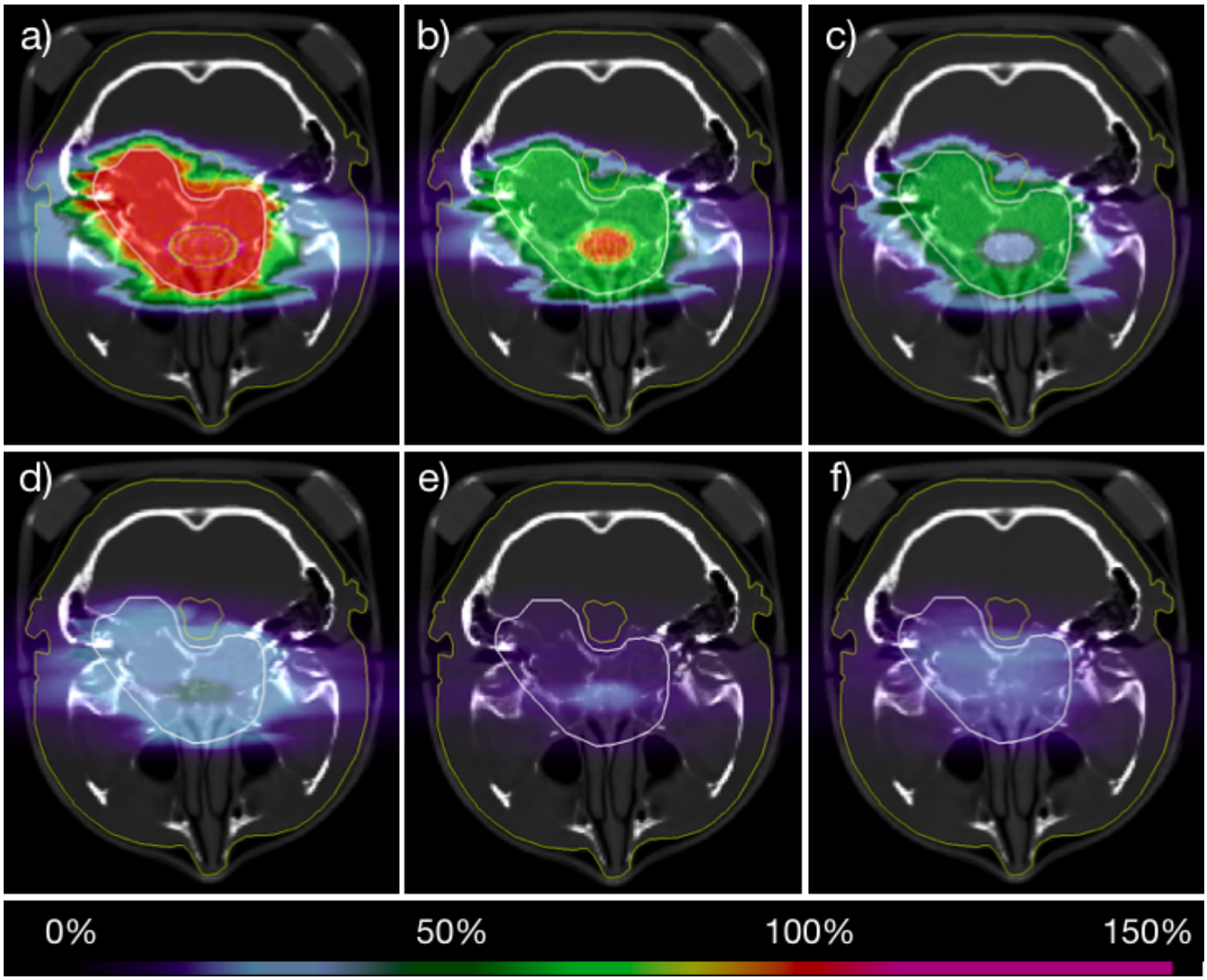

Figure 4.9.: Biologically optimized four-field ^{16}O + ^{4}He plan for a partially hypoxic skull base chordoma (scenario 1). The tumor and brainstem are marked with white and yellow lines, respectively. The scale represents the relative dose received by the tissue, compared to the prescribed biological dose of 2 Gy. (a) - total biological dose, (b) and (c) - contributions of ^{16}O and ^{4}He, (d) - total physical dose, (e) and (f) - contributions of ^{16}O and ^{4}He.

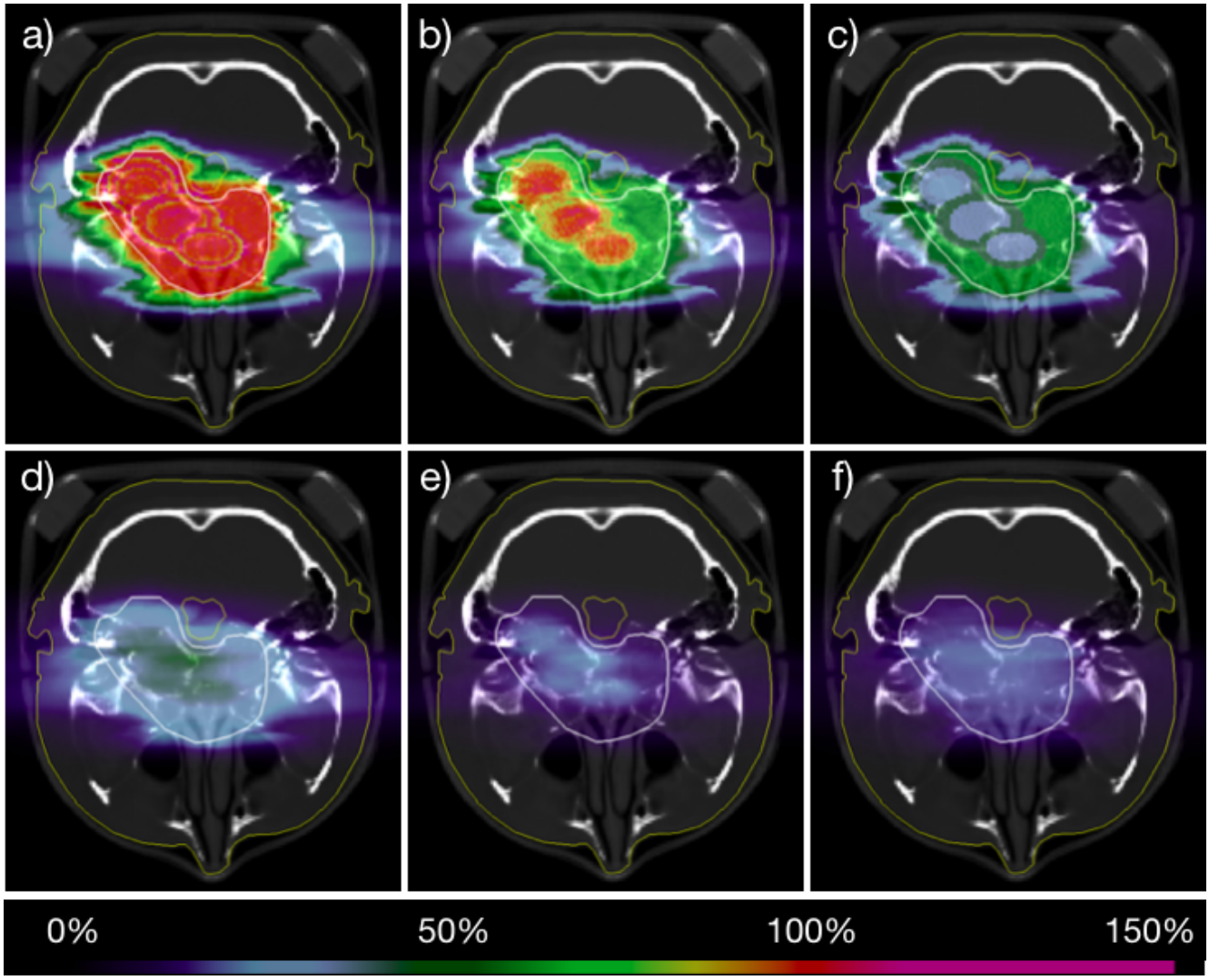

Figure 4.10.: Biologically optimized four-field ^{16}O + ^{4}He plan for a partially hypoxic skull base chordoma (scenario 2). The tumor and brainstem are marked with white and yellow lines, respectively. The scale represents the relative dose received by the tissue, compared to the prescribed biological dose of 2 Gy. (a) - total biological dose, (b) and (c) - contributions of ^{16}O and ^{4}He, (d) - total physical dose, (e) and (f) - contributions of ^{16}O and ^{4}He.

One of the possible explanations to this effect can the presence of the few high-LET particles in the distal regions delivering the very low doses. This will lead to the high values of the dose-averaged LET in these regions. The similar effect was observed in the work of [Bassler et al., 2014] presenting the results of the LET-painting optimization. However, in contrast to the LET-painting, the kill- painting, achieve automatically an optimal LET distribution in the target, without imposing a set of dose ramps, now demonstrated also in a 3D profile.

More information on the optimization results is given below. Figures 4.12 and 4.13 represent the dose-volume histograms for the single-ion and combined plans for each of the two tests, respectively. The following Table 4.3 contains the corresponding numerical values of minimal, maximal and average relative doses received by the target, brainstem and residual tissue. The final comparison of the mean and maximal relative doses delivered to the brainstem and residual tissue between the hypoxic plans and normoxic plan is given in Figure 4.14.

As follows from the Tables 4.1 and 4.3, for all of the plans the mean doses delivered to the brainstem are practically not affected by the presence of hypoxia, similarly to as what was shown in the Chapter 3. For both cases of oxygenation the combined plan shows the lowest value of this parameter, decreasing the dose by 10-12% compared to the pure ^{16}O plan and 3-5% - to the

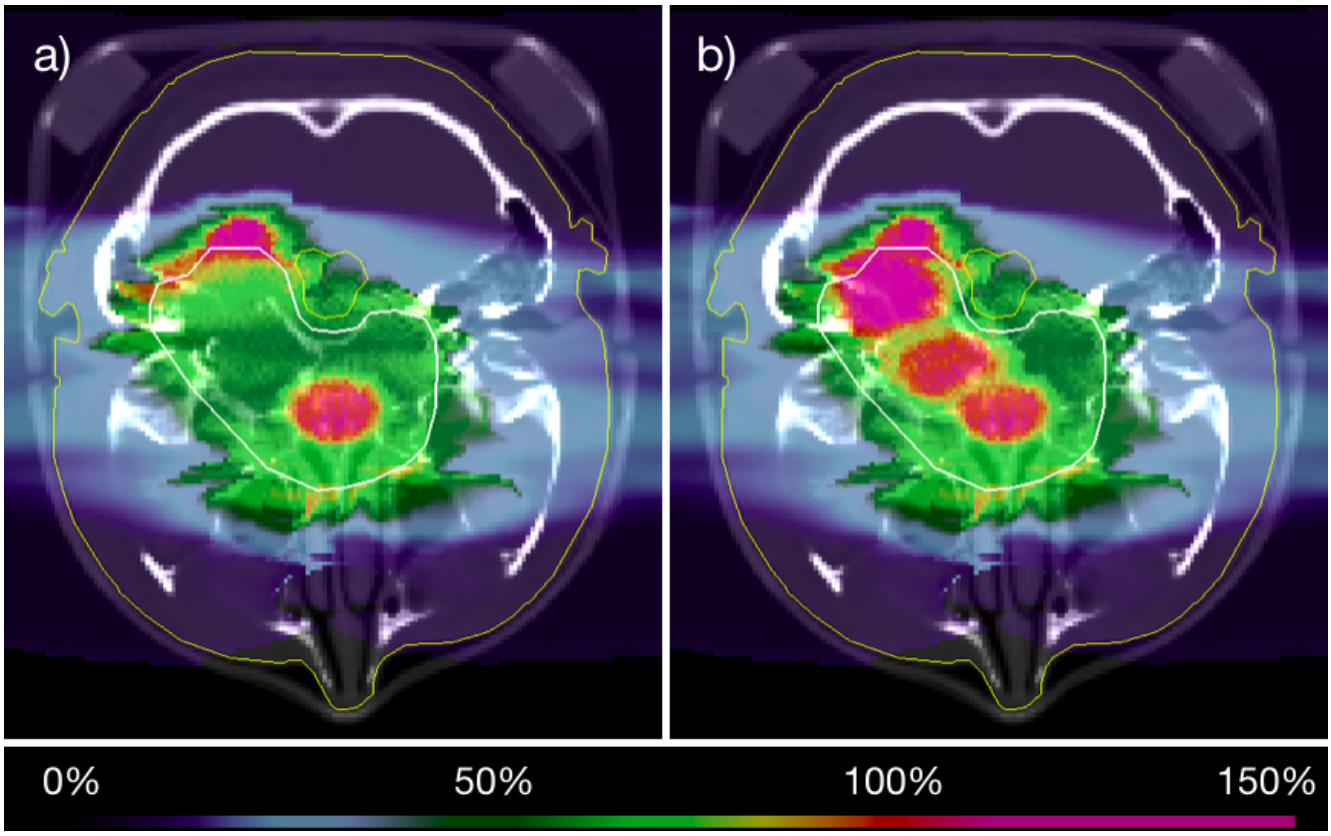

Figure 4.11.: Dose-averaged LET distribution at the central axial CT slice for the two biologically optimized four-field ^{16}O + ^{4}He plans for a partially hypoxic skull base chordoma. The tumor and brainstem are marked with green and yellow lines, accordingly. The 100% on the scale corresponds to the dose-mean LET of 60 keV/μm. (a) - test 1, one small hypoxic region, (b) - test 2, a larger extended hypoxic region.

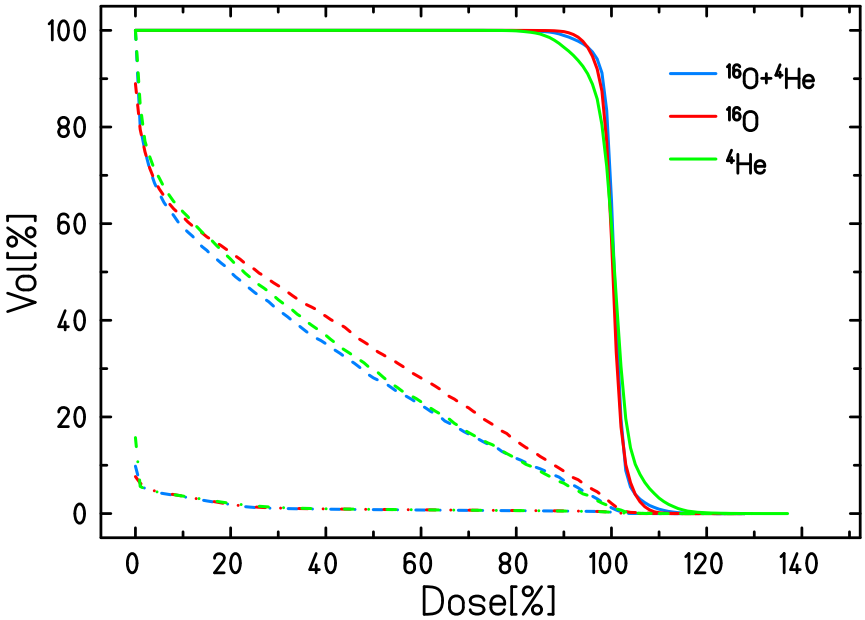

Figure 4.12.: Dose-volume histogram comparison for the two-fields plans of ^{16}O (red), ^{4}He (green) and a four-field combined plan ^{16}O + ^{4}He (light blue), optimized for a uniform OER- and RBE-weighted dose of 2 Gy in a partially normoxic skull base chordoma, scenario 1. Solid lines correspond to the DVHs for the target, dashed lines - for the brainstem, dot-dashed - for the residual tissue.

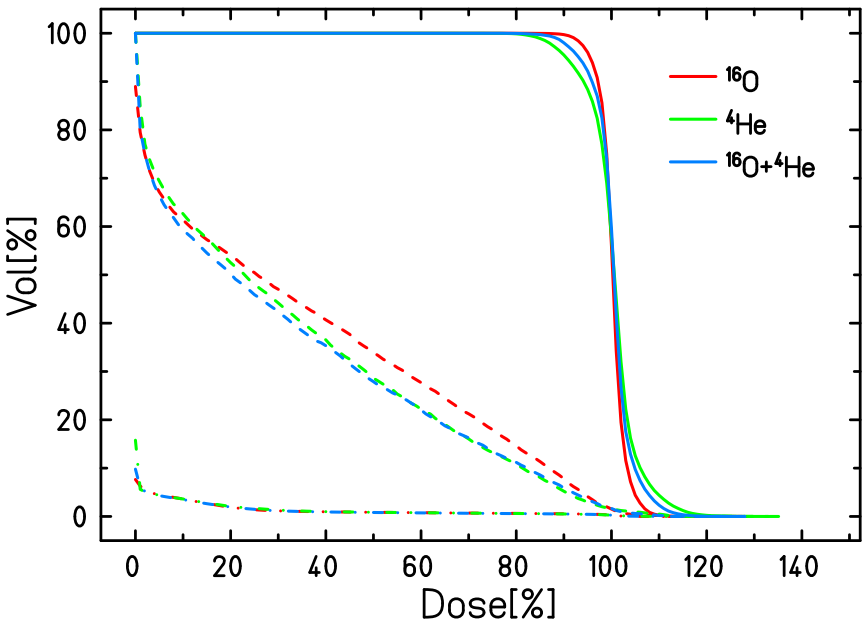

Figure 4.13.: Dose-volume histogram comparison for the two-fields plans of ^{16}O (red), ^{4}He (green) and a four-field combined plan ^{16}O + ^{4}He (light blue), optimized for a uniform OER- and RBE-weighted dose of 2 Gy in a partially normoxic skull base chordoma, scenario 2. Solid lines correspond to the DVHs for the target, dashed lines - for the brainstem, dot-dashed - for the residual tissue.

plan with ^{4}He beams. For the second scenario with a larger hypoxic area this dose decrease in case of the combined plan is slightly lower (≈10.7% and 3.1% compared to the single-ion plans). The explanation might be the larger presence of ^{16}O in the tumor regions in the proximity of brainstem, which leads to a larger production of secondary particles, compared to the cases with normoxic or another hypoxic target.

Similar to as in the tests presented in the previous chapter, the values of the maximal doses to the brainstem are sensitive to the oxygenation level of the tumor and also depend on its location. In particular, for the first scenario these values are almost not affected compared to the normoxic plan since the field redistribution difference between these two plans (oxygen boost in hypoxic region) occur in the area of the target laying relatively far away from the brainstem, while in the remaining parts of the target the biological dose contributions are almost equal. The maximal dose values remain approximately 2.21, 2.15 and 2.15 Gy for the ^{16}O, ^{4}He and the combined plan, respectively. In the second scenario an increase in the maximal dose compared to the normoxic plan is observed for all the three plans and is the most significant for the ^{4}He (21%). The most insensitive is the ^{16}O plan (an increase of 5%). The relative increase for the combined plan is intermediate (7.8%), however, the value it is reaching (2.15 Gy) is the same as the value for the ^{16}O plan.

Thus, for both scenarios, the combined plan tend to show the values similar to the better single-ion plan out of two for the maximal dose to the brainstem. This way, in normoxic case or for the targets with the small and deeply located hypoxic areas (scenario 1), the ^{16}O + ^{4}He plan leads to the same maximal doses as the pure ^{4}He plan, while with the spreading hypoxia (scenario 2) the corresponding result will become similar to the one with ^{16}O plan.

Ion type	VOI	Test 1			Test 2		
		D_{min}/D_p	D_{max}/D_p	D_{mean}/D_p	D_{min}/D_p	D_{max}/D_p	D_{mean}/D_p
^{16}O	Target	0.81	1.16	1	0.79	1.17	1
	Brainstem	0	1.10	0.35	0	1.16	0.35
	Residual	0	1.27	0.014	0	1.23	0.014
^{4}He	Target	0.68	1.31	1	0.67	1.31	1
	Brainstem	0	1.08	0.33	0	1.30	0.32
	Residual	0	1.31	0.014	0	1.37	0.015
^{16}O + ^{4}He	Target	0.58	1.23	1.01	0.57	1.23	1
	Brainstem	0	1.08	0.31	0	1.16	0.31
	Residual	0	1.23	0.013	0.001	1.27	0.014

Table 4.3.: Minimal (D_{min}), maximal (D_{max}) and average (D_{mean}) relative doses, compared to the planned dose of 2 Gy(RBE,OER) (D_p), received by the target, brainstem and residual tissue in case of irradiating two cases of partially hypoxic skull base chordoma with two fields of ^{16}O, ^{4}He, and their four-field combination.

With regards to the doses received by residual tissue, making the analysis based on the mean dose values from the Table 4.3 is difficult since, as was previously mentioned, the main part of the total number of CT voxels receive zero dose, making the mean value very low. The highest mean dose among all the 9 examined plans (0.029 Gy) was observed for the ^{4}He plan for the most hypoxic tumor. It can be still mentioned that for both cases of hypoxia distribution the value of the mean dose to the residual tissue is the lowest for the combined plan. However, the trend for the maximal dose appears to be dependent again on the location and/or position of the hypoxic region. For the scenario 1, the combined plan shows the best result too, providing the decrease of the maximal dose to residual tissue by 3.2% compared to the ^{16}O plan and 6.3% - to the pure ^{4}He plan. In scenario 2, adding the ^{4}He beams to the pure ^{16}O plan would, in contrast, increase the maximal dose to residual tissue by 3.2%.

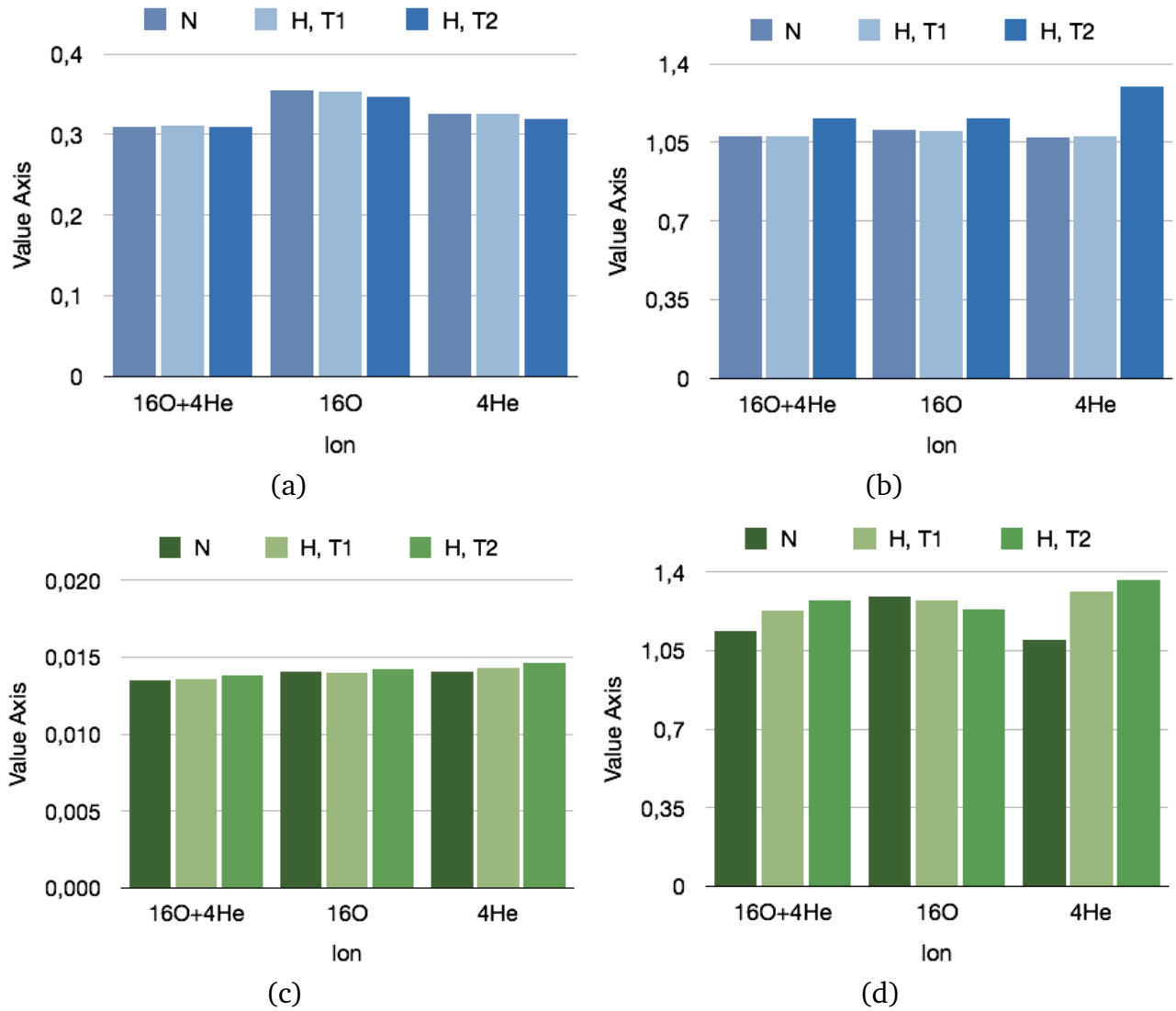

Figure 4.14.: Mean and maximal relative doses received by the brainstem (a, b) and residual tissue (c, d) for the plan optimized for a 2 Gy RBE- and OER-weighted dose for a normoxic (N) and two cases of partially hypoxic (H, T1 and T2) skull base chordoma irradiated with two fields of ^{16}O, ^{4}He, and their four-field combination.

4.3.3 Summary

The multi-ion optimization approach, presented here, allows performing the biological treatment planning with several ion modalities simultaneously. When no particular constraints are introduced, the contributions of each ion to the resulting biological dose are expected to be almost equal. On the other hand, when hypoxia is used as a driving force for the optimization, a redistribution of the fields occurs. The system forwards the heavier ions to the areas with decreased oxygenation, while the lighter modalities are avoided there. The residual normoxic areas receive the dose from both types of ions, with the slight preference given to the lighter ones.

The tests, demonstrated in this chapter, aimed at the improvement of the quality of hypoxic treatment plans with ^{16}O beams with ^{4}He ions chosen as a lighter alternative. The investigated geometry was chosen in a way that in normoxic conditions the brainstem was receiving the increased dose in case of the ^{16}O plan. At the same time, the studies in the previous chapter showed that the plans with ^{16}O are the most 'insensitive' to the presence of hypoxia, while ^{4}He performs noticeably worse in the same conditions. Applying the combined plan to the normoxic target demonstrated the decrease of the mean doses to the brainstem and residual tissues while keeping the corresponding maximal doses intermediate. When the multi-ion plan is applied to the hypoxic targets, the difference in the mean doses might slightly decrease depending on the size and location of hypoxic area, however, the maximal doses remain at the same levels as in case of pure ^{16}O plans. The study in the previous chapter demonstrated that ^{16}O plans might allow achieving the lowest maximal doses to the neighboring OARs when the hypoxic tumor is irradiated. Thus, the multi-ion optimization, used with the hypoxic targets, allows both to keep the maximal dose to the critical structures the lowest, while reducing the mean doses to them and the residual tissue by optimally operating with the benefits of each of the ion.

As mentioned in the beginning of this chapter, the decision whether multi-ion optimization is beneficial or not for the particular case of tumor, must be made based on the knowledge about the performance of the corresponding single-ion plans. If the heavy ion plan allows achieving the lower doses to OARs and residual tissue when applied to the normoxic target, it is expected to show also the best performance in hypoxia.

Summary and conclusion

In the past few years ^{16}O ions started to gain the attention of researchers and clinicians in the field of radiation therapy as an alternative to the already established ^{12}C ion beam. The main reason for that is the increased LET of the beam which was proven to be the key to overcome the problem of tumor hypoxia. However, the increased atomic number of the ion leads to several drawbacks as well. Among them are the increased nuclear fragmentation and potentially unnecessarily high RBE. Thus, an in-depth study of physical and radiobiological characteristics of the beam and further comparative treatment planning studies are essential to asses the beam's applicability for the clinical practice.

In this dissertation, the experimental verification of the clinically relevant physical and radiobiological properties of ^{16}O beams together with the following treatment plan analysis was carried out. The GSI in-house TPS TRiP98 was expanded in order to enable the optimization with multiple ion fields for hypoxic tumors and was tested with combined ^{16}O and ^{4}He plans. The aim of the whole study was assessing the quality of the current status of the ^{16}O beam description and defining the ranges of its potential clinical application.

The experiments, presented in Chapter 2, have demonstrated the reliability of the currently implemented physical beam model for ^{16}O beams. The water phantom measurements with pinpoint chambers demonstrated a good agreement with the TRiP98 prediction for the absorbed dose profiles in both beam eye view and lateral directions at different depths. The slight deviation between the measurements and the TPS calculation in the lateral profile in fragmentation tail region point the need for the further experimental investigation of ^{16}O beams fragmentation. At the moment, no experimental works on ^{16}O fragmentation are published and the TRiP98 beam model in based on the fragmentation data for the underlying ions.

The series of RBE measurements with the CHO-K1 cell line, triggered by the incomplete knowledge of radiobiological properties of ^{16}O ions, noticeably expanded the RBE-LET database of the beams for both low and high LET values. It was shown that ^{16}O RBE_{10} values for the low (below 25 keV/μm) or very high (above 600 keV/μm) LET values are almost equal to the photon efficiency, and reaches their maximum of $\geq$2.5 in the region of 200-300 keV/μm. A more precise estimation of the maximum values was not possible within the current work since the beams of the required energies are not available at HIT and GSI facilities. More measurements at ^{16}O with energies in the range of 20-100 MeV/u are already planned at other facilities.

Since the main idea behind the introduction of ^{16}O into clinical practice is the treatment of hypoxic tumors, the corresponding radiobiological experiments were performed. The survival measurements with GSI hypoxic chambers confirmed the TRiP98 predictions of the OER of ^{16}O beams with dose-averaged LET of 166 keV/μm. As a next step, the survival verification for the

unevenly oxygenated extended target using the 'hypoxic phantom' showed the applicability of the kill-painting approach, developed earlier at GSI, to the ions beyond ^{12}C. It was experimentally demonstrated for the first time, that ^{16}O might be more beneficial compared to the lighter ion beams regarding the cell survival in the entrance channel when irradiating hypoxic tumors.

All the cell survival experiments in Chapter 2 were conducted with the cell monolayers. Apart from potential differences between the cell growth and radiosensitivities when cultured in monolayers and 3D, the latter way of the cell culture opens more opportunities for the more sophisticated tests. For example, the resolution of the experiments could be increased and allow also the check of the cell survival in the lateral fall-off of the beam, or arranging the more complicated phantoms for more realistic verifications.

Treatment planning studies, demonstrated in Chapter 3, aimed at comparison of quality of optimization with ^{16}O beams and lighter modalities, such as ^{12}C, ^{4}He and protons for normoxic and hypoxic tumors. It implied the study for a box-shaped geometry used for the experiments with extended target irradiation, as well as the studies with GSI pilot project patients plans and artificially created complementary hypoxia maps. The study with the box target was inspired by the experimental results obtained with the extended target irradiation and implied the analysis of the survival in the entrance channel with the different impact of target hypoxia. The result can be summarized as follows: for the treatment of the normoxic (21% pO_2) or slightly hypoxic tumors ($\approx$ 20% or less of its volume has decreased pO_2) with high doses the irradiation with ^{16}O doses do not lead to any improvement of cell survival in the entrance channel. In contrast, for the highly hypoxic tumors (>50% of the total volume has $pO_2 \approx 0.5\%$ or lower) irradiation with ^{16}O is expected to lead to 10-15% survival increase in the entrance channel in a single fraction, compared to the lighter beams.

The following studies implying real patients plans assessed the tumor dose coverage and the damage to the OAR in its proximity. It was demonstrated, that the treatment plans with ^{16}O beams are least sensitive to the presence of hypoxic regions in the target, which is essential since the location and sizes of these regions can vary between the different treatment sessions. Apart from that, ^{16}O might deliver the lowest maximal doses to the OAR and residual tissue when the tumor is higly hypoxic. This is an important benefit when it comes to the damage of serial organs at risk. However, at the same time, ^{12}C or ^{4}He ions might still deliver the lower average doses to the OAR and residual tissue. Thus, the decision on the type of ion to be applied for the treatment of a particular tumor must always be based on its shape, level of hypoxia, relative position of the OAR and their type (serial or parallel).

Chapter 4 introduced the latest version of the GSI TRiP98 TPS which is so far the only TPS able to calculate the biological effect of several primary ions within one treatment plan for hypoxic tumors. The aim of this approach is taking benefit from several ions inside one treatment plan, such as the reduced nuclear fragmentation of the light ions or the high RBE and LET of the heavier ions. Uniform cell survival is achieved by forwarding the heavier ion modalities to the hypoxic regions of the target while covering the normoxic areas also with the lighter ions. This allows one to increase the dose-averaged LET distribution in hypoxic parts to reduce the OER

while avoiding the too high $\overline{\text{LET}}$ where it is not necessary. However, multiple-ion planning has to be chosen wisely, since, apart from the generally longer optimization times and slightly increased irradiation times, they can be worse than single-ion plans. In this chapter, the results of testing this approach are given for combined ^{16}O + ^{4}He plans since both are mostly discussed nowadays as the alternatives to the well-established ^{12}C and ^{1}H, respectively. In the study with the skull-base chordoma, it was shown that applying a four-field combined plan allows reducing the mean dose to the brainstem by 3-5% compared to the pure ^{4}He plan and by 10-12% compared to the pure ^{16}O plan. At the same time this plan is beneficial regarding the maximal dose to the OAR, since it always remains as low as possible, meaning it being the same as for the ^{4}He plan in normoxia and as for ^{16}O plan in hypoxia.

As already mentioned, the studies with the patients' plans presented in Chapters 3 and 4 were carried out with artificially created hypoxia maps. The tool that was used for generating them implies a set of limitations on the sizes and locations of hypoxic regions. In all the studies presented in this work, the hypoxic region was modeled as a rather regular-shaped area with the oxygenation decreasing towards its center. Even if similar images of real hypoxia maps can be found in literature, such as the ones for a head and neck squamous-cell carcinoma [Bassler et al., 2014] or for a renal cell carcinoma [Fleming et al., 2015], a more random distribution of smaller regions of more irregular shapes, varying in time, is expected to be found in many tumors. Future realistic tests should use real hypoxia maps obtained from the clinics. At the moment the problem of interpretation of FMISO-PET data remains not completely solved.

Another remaining task is performing the further multiple-ion studies involving other ions apart from ^{16}O and ^{4}He, primarily ^{12}C ions. As the study with the ACC patient plans in Chapter 3 revealed, ^{12}C might remain beneficial even when applied to hypoxic tumors.

The experimental biological verification of the multiple-ion treatment planning is essential and is one of the directions of the further work. Apart from the general estimation of the planning reliability, it is important to make sure the increased time of the irradiation session does not reflect the cellular effects. Another issue that is of a high importance for the combined planning, is the precision of the particle range determination. Since the redistribution of the fields is expected to occur in the different regions of the tumor, the positioning of the patient and the calculations of the ranges of all the primaries have to be done with a high degree of accuracy. However, this is not within the scope of the current work.

In general, the clinical application of the multi-ion approach is realistic. For example, at HIT the switching from one ion type to another one coming from the same source (from ^{16}O to ^{12}C, or vice versa) already takes not more than 10 minutes. Moreover, since the approach implies the usage of different ion combinations, e.g., ^{16}O + ^{4}He, no switch is required at all since there are different sources for these ions which run continuously. Recently, [Toshiba, 2017] reported that they managed to achieve the switching time between the two ions within one source to be less than a minute. Since the dose is split between more fields, the irradiation with each of them will be shorter. This way, the total irradiation time is expected to exceed the one in case of standard single-ion treatment only by the time required to rotate the patient. For the

tests, presented here, only the four-fields multi-ion plans were studied, however, in other cases, a reduced number of multiple-ion fields might be more beneficial.

The results of this work can be summarized as follows:

- The present status of ^{16}O physical and radiobiological beam models allows a reliable treatment plan optimization that has been confirmed experimentally;
- The knowledge of the radiobiological properties of the beam, in particular the pool of RBE and OER values, was expanded;
- The comparative analysis of the treatment plans with ^{16}O ions and lighter modalities revealed that ^{16}O allow the most uniform target coverage, decrease of the dose in the residual tissue entrance channel and avoiding local hotspots in the organs at risk when the tumor is hypoxic;
- TRiP98 TPS was upgraded to handle multiple primary beams for hypoxic tumors;
- The multiple-ion treatment planning might lead to the further improvement of the treatment plan quality.

This work is expected to contribute to the transition of hypoxic tumors treatment planning and irradiation with ^{16}O ions into clinical routine. The recent reports and the growing number of corresponding publications show the interest coming not from basic science, but also from the clinicians themselves. Since several of the currently operating particle therapy centers which offer the ^{12}C beams possess already the possibility to irradiate with ^{16}O beams at least for research purpose, it is highly probable that the therapy with the latter modality can start within the next decade.

A X-ray response of CHO-K1 cell line

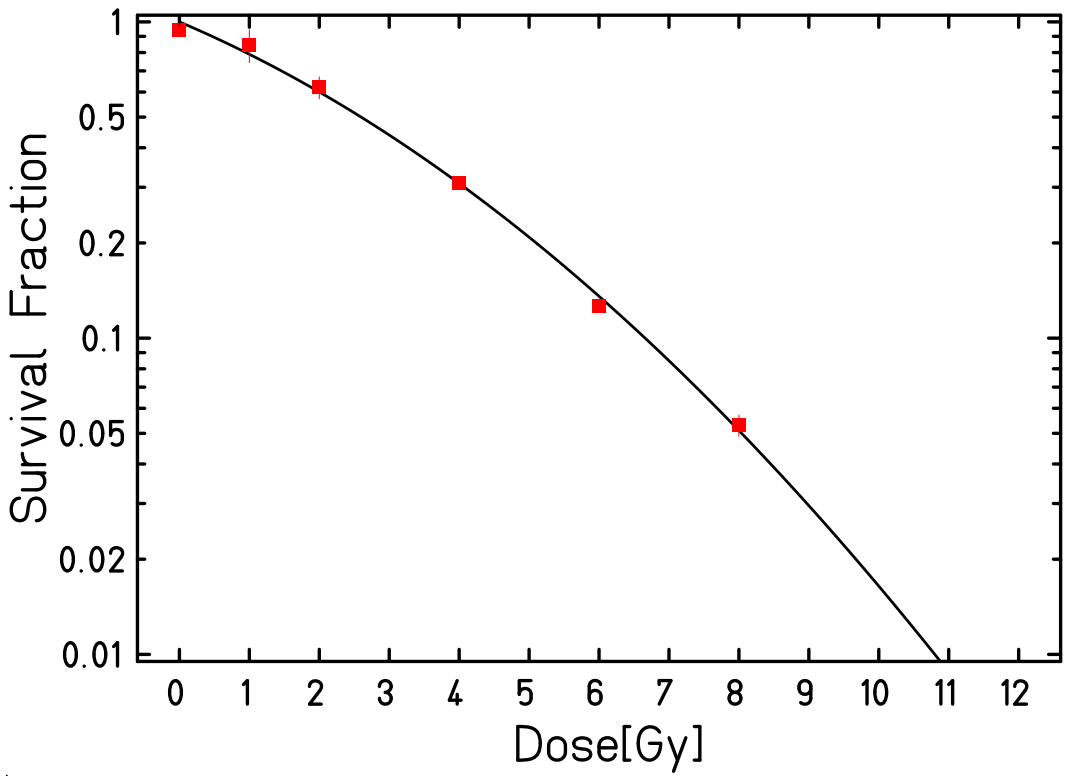

Figure A.1.: Caption.

Table A.1.: LQ parameters of the reference X-ray survival curve measured for the CHO-K1 cell line. The numerical values of the measured points are give in Appendix E.

$\alpha_{\mathrm{X-ray}}$ (Gy^{-1})	$\beta_{\mathrm{X-ray}}$ (Gy^{-2})	D_t, Gy
0.216±0.031	0.019±0.004	17

B Water equivalent ratio of materials used in cell irradiation setups

Material	Used at	WEQ	Source
Cell culture medium	Filling of the cell samples (rings, tissue culture flasks, Petri dishes)	1	[Grumezescu, 2016]
Polystyrene	Tissue culture flask wall, range shifting material in hypoxic phantom, Petri dishes material	1.042	[de Vera et al., 2014]
Biofolie 25	Cell growth surface of the rings	1.88	[Ma et al., 2013]
PEEK (Polyether ether ketone)	Hypoxic chamber walls	1.27	[Peter Steidl (Private communication)]

C Calibration for beam monitors in ^{16}O beam at HIT facility

The procedure of the calibration of the beam monitors for heavy ion beams delivered by means of scanning system, initially developed for the former ^{12}C treatment facility at GSI and later transferred to HIT, was developed and described by [Jäkel et al., 2004].

The calibration is energy-dependent and should be valid for all the available beam energies. It is performed in units of number of particles per monitor unit. The measurement of particle number is indirect through the measurement of absorbed dose to water with the Farmer chamber. The latter has a calibration factor in terms of absorbed dose to water (^{60}Co beam used as a reference beam).

The chamber is placed inside the phantom consisting of water-equivalent material that is irradiated with several (typically, five or six) fields of different fixed energies, corresponding to different penetration depths in water. The absorbed dose is defined as follows:

$$D_{abs} = M k_Q N_w, \tag{C.1}$$

where M is the reading of the dosimeter, N_w is a calibration factor in terms of absorbed dose to water in ^{60}Co field, and k_Q being the radiation beam quality factor accounting for the difference between the beam of interest and the calibration beam. Based on that, the calibration factor for a given energy E is defined as a number of particles N per monitor unit MU, assuming the homogeneous distribution of the delivered dose:

$$K(E) = \frac{N}{MU} = \frac{1}{MU} \frac{D_{abs} \Delta x \Delta y}{S_E(x)}, \tag{C.2}$$

where Δx and Δy are the raster scanner step sizes in x- and y-directions, respectively, and $S_E(x)$ is the mass stopping power of the ions with initial energy E measured at a depth x. After that, the calculated factors are interpolated, giving a calibration curve for the other energies.

The set of the measured calibration factors for ^{16}O beam monitor used for a part of the experiments presented in Chapter 2, is shown in Figure C.1. The precision of the dosimetry is very high and, despite the small fluctuations that can be observed, the reproducibility of the results is within less than 1%.

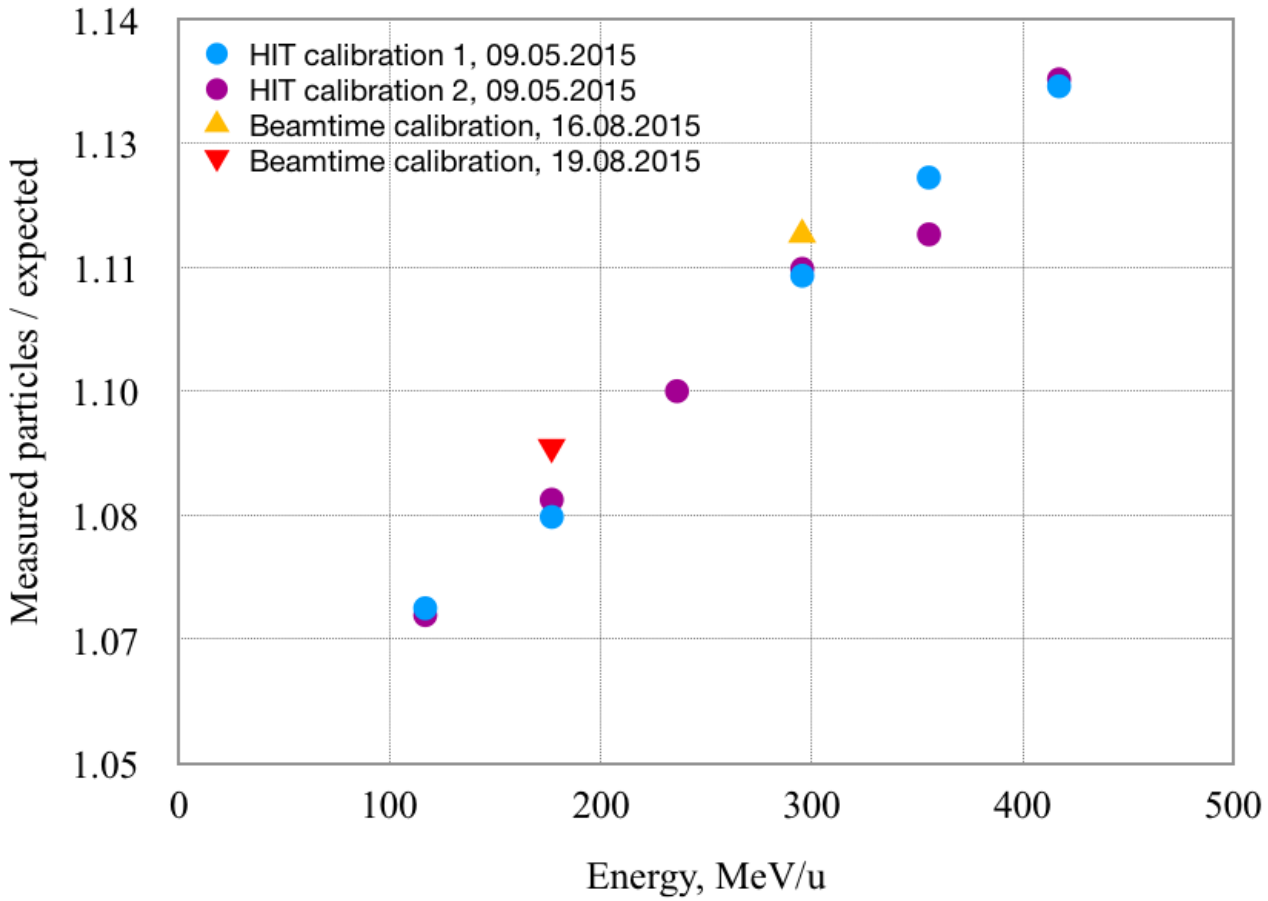

Figure C.1.: Relative measured number of particles dependency on their energies measured for the dose calibration for ^{16}O at the experimental cave of HIT, Heideilberg in 2015. Data are courtesy of Dr. Emanuele Scifoni.

D Measurements of the pinpoint chambers for the absorbed dose profiles verification

Table D.1.: Average doses and the standard error of the mean measured by the two central pinpoint chambers for a treatment plan optimized for a uniform RBE-weighted dose of 4 Gy in the target.

Position, mm	Dose, Gy	±SEM, Gy
61.7	2.802	0.007999
71.7	2.687	0.0015
81.7	2.523	0.007999
91.7	2.332	0.006499
101.7	2.123	0.014
111.7	1.8	0.004499
64.7	2.758	0.0009998
74.7	2.61	0.0015
84.7	2.489	0.0175
94.7	2.314	0.0004999
104.7	2.026	0.0025
114.7	0.8855	0.02885
16.7	2.159	0.006499
26.7	2.216	0.003499
36.7	2.325	0.003
46.7	2.538	0.003499
56.7	2.859	0.003
66.7	2.721	0.003999

Table D.2.: Average doses and the standard error of the mean measured by the two central pinpoint chambers for a treatment plan optimized for a uniform absorbed dose of 4 Gy in the target.

Position, mm	Dose, Gy	±SEM, Gy
74.7	4.072	0.009998
84.7	4.03	0.0025
94.7	4.03	0.0009998
104.7	4.023	0.005999
114.7	0.6838	0.005649
124.7	0.4536	0.004649
89.7	4.038	0.013
99.7	4.006	0.005999
119.7	0.5641	0.0005499
129.7	0.379	0.004999
139.7	0.2789	0.00325
19.7	3.261	0.004999
29.7	3.349	0
39.7	3.507	0.011
49.7	3.833	0.0025
59.7	4.014	0.013
77.7	3.905	0.0025
87.7	4.131	0.012
97.7	4.089	0.018
117.7	0.6607	0.0122
127.7	0.4426	0.004649
19.7	3.227	0.008999
29.7	3.32	0.005999
39.7	3.487	0.0025
49.7	3.741	0.009998
59.7	3.952	0.0004999
69.7	4.133	0.0135
129.7	0.4148	0.003649
139.7	0.2999	0.00235
149.7	0.2385	0.0021
159.7	0.2074	0.000099
169.7	0.1741	0.004049
179.7	0.1499	0.0019

Table D.3.: Measurements of the pinpoint chambers during the verification of the lateral dose profile at a depth of 19.7 mm for a plan optimized for a uniform absorbed dose of 4 Gy in the target.

Distance from the center, mm	Dose, Gy	Measurement error, Gy	Distance from the center, mm	Dose, Gy	Measurement error, Gy
-82	0.0002	0.00014	-10	3.236	0.01799
-70	0.0028	0.00053	-9	3.256	0.01804
-61	0.0006	0.00024	-6	3.238	0.01799
-58	0.0011	0.00033	-3	3.229	0.01797
-50	0.0002	0.00014	-3	3.225	0.01796
-49	0.0041	0.00064	3	3.266	0.01807
-48	0.0002	0.00014	9	3.221	0.01795
-46	0.0003	0.00017	15	3.224	0.01796
-46	0.0053	0.00073	19	3.231	0.01797
-42	0.0017	0.00041	21	2.966	0.01722
-39	0.0018	0.00042	25	1.92	0.01386
-38	0.0095	0.00097	31	0.1733	0.00416
-37	0.0153	0.00124	33	0.0353	0.00188
-36	0.0124	0.00111	37	0.0128	0.00113
-34	0.0261	0.00162	43	0.0053	0.00073
-30	0.2927	0.00541	46	0.0042	0.00065
-27	0.982	0.00991	49	0.003	0.00055
-26	1.248	0.01117	55	0.0043	0.00066
-25	1.457	0.01207	57	0.0009	0.00030
-24	1.945	0.01395	58	0.0036	0.00060
-22	2.619	0.01618	61	0.0036	0.00060
-21	2.836	0.01684	69	0.0015	0.00039
-18	3.234	0.01798	70	0.0011	0.00033
-15	3.204	0.01790	81	0.0003	0.00017
-14	3.222	0.01795	82	0.0015	0.00039
-12	3.218	0.01794	93	0.0013	0.00036

Table D.4.: Measurements of the pinpoint chambers during the verification of the lateral dose profile at a depth of 59.7 mm for a plan optimized for a uniform absorbed dose of 4 Gy in the target.

Distance from the center, mm	Dose, Gy	Measurement error, Gy	Distance from the center, mm	Dose, Gy	Measurement error, Gy
-82	0.0002	0.00014	-9	4.001	0.02000
-70	0.0004	0.0002	-9	3.953	0.01988
-61	0.002	0.00045	-6	3.937	0.01984
-58	0.0043	0.00066	-3	3.949	0.01987
-50	0.0047	0.00069	-3	3.98	0.01994
-49	0.0042	0.00065	3	4.027	0.02007
-48	0.0106	0.00103	3	3.952	0.01988
-46	0.0106	0.00103	9	3.973	0.01993
-46	0.0104	0.00102	15	3.985	0.01996
-42	0.0148	0.00122	15	3.91	0.01977
-39	0.0187	0.00137	19	3.964	0.01991
-38	0.0197	0.00140	21	3.554	0.01885
-37	0.0275	0.00166	25	2.414	0.01554
-36	0.0303	0.00174	31	0.2515	0.00501
-34	0.0495	0.00222	33	0.0702	0.00265
-30	0.3669	0.00606	37	0.0206	0.00144
-27	1.181	0.01087	43	0.012	0.00109
-26	1.687	0.01299	46	0.0083	0.00091
-25	1.692	0.01301	49	0.0076	0.00087
-24	2.55	0.01597	55	0.0083	0.00091
-22	3.338	0.01827	57	0.0037	0.00061
-21	3.539	0.01881	58	0.0005	0.00022
-21	3.497	0.01870	61	0.0062	0.00079
-18	3.975	0.01994	69	0.0003	0.00017
-15	3.924	0.01981	70	0.0012	0.00035
-14	3.879	0.01969	81	0.0008	0.00028
-12	3.899	0.01975	82	0.0026	0.00051
-10	3.956	0.01989	93	0.0032	0.00057

Table D.5.: Measurements of the pinpoint chambers during the verification of the lateral dose profile at a depth of 89.7 mm for a plan optimized for a uniform absorbed dose of 4 Gy in the target.

Distance from the center, mm	Dose, Gy	Measurement error, Gy
-21	3.7	0.01924
-9	4.025	0.02006
-3	4.032	0.02008
0	4.04	0.02009
2	4.042	0.02010
3	4.051	0.02013
4	4.046	0.02011
6	4.031	0.02008
8	4.028	0.02007
9	4.034	0.02008
12	4.003	0.02001
14	3.995	0.01999
15	4.007	0.02002
16	3.999	0.01999
18	3.983	0.01996
19	3.974	0.01993
20	3.92	0.01979
21	3.859	0.01964
24	3.197	0.01788
26	2.416	0.01554
28	1.529	0.01236
30	0.7588	0.00871
31	0.4379	0.00662
32	0.2947	0.00543
33	0.1728	0.00416
36	0.0505	0.00225
38	0.0284	0.00169
40	0.0255	0.00159
42	0.0199	0.00141
43	0.0184	0.00136
44	0.0174	0.00132
55	0.0075	0.00087

Table D.6.: Measurements of the pinpoint chambers during the verification of the lateral dose profile at a depth of 129.7 mm for a plan optimized for a uniform absorbed dose of 4 Gy in the target.

Distance from the center, mm	Dose, Gy	Measurement error, Gy
-21	0.288	0.00537
-9	0.374	0.00612
-3	0.3844	0.00620
0	0.3866	0.00622
2	0.4018	0.00634
3	0.384	0.00619
4	0.3874	0.00622
6	0.3894	0.00624
8	0.3887	0.00623
9	0.3774	0.00614
12	0.3748	0.00612
14	0.3781	0.00615
15	0.3666	0.00605
16	0.3664	0.00605
18	0.3566	0.00597
19	0.3583	0.00599
20	0.3362	0.00579
21	0.3138	0.00560
24	0.2471	0.00497
26	0.204	0.00452
28	0.141	0.00375
30	0.0996	0.00316
31	0.0962	0.00310
32	0.0707	0.00266
33	0.0604	0.00246
36	0.0394	0.00198
38	0.0415	0.0020 4
40	0.0257	0.00160
42	0.0241	0.00155
43	0.0298	0.00173
44	0.0214	0.00146
55	0.0185	0.00136

E Survival measurements for the data presented in Chapter 2

Table E.1.: X-ray

Dose, Gy	Survival	±SEM
0	0.9409	0.0450
1	0.8433	0.1002
2	0.6208	0.0492
4	0.3090	0.0013
6	0.1264	0.0005
8	0.0530	0.0040

Table E.2.: ^{16}O, 3 MeV/u (670 keV/mu)

Dose, Gy	Survival	±SEM
0	0.9738	0.1181
1	0.6553	0.0254
2	0.4529	0.0361
3	0.2529	0.0291
4	0.1107	0.0008
5	0.0605	0.0063
6	0.0476	0.0185
7	0.0415	0.0053
8	0.0196	0.0018

Table E.3.: ^{16}O, 19.6 MeV/u (166 keV/mu), normoxia

Dose, Gy	Survival	±SEM
0	0.9031	0.0948
0.5	0.8328	0.2088
1	0.5048	0.0486
2	0.2052	0.0301
3	0.0939	0.0030
4	0.0376	0.0068

Table E.4.: ^{16}O, 46.8 MeV/u (83 keV/mu)

Dose, Gy	Survival	±SEM
0	1.0987	0.1037
0.5	0.7072	0.0611
1	0.4855	0.1305
2	0.2342	0.0236
3	0.1139	0.0134
4	0.0405	0.0132

Table E.5.: ^{16}O, 146 MeV/u (38 keV/mu)

Dose, Gy	Survival	±SEM
0	0.8960	0.1477
1	0.7063	0.0825
2	0.3968	0.1085
3	0.2059	0.0214
5	0.0475	0.0029
7	0.0083	0.0021

Table E.6.: ^{16}O, 280 MeV/u (23 keV/mu)

Dose, Gy	Survival	±SEM
0	0.9581	0.1423
1	0.7323	0.0005
2	0.4034	0.0559
3	0.3896	0.0052
5	0.1355	0.0124
7	0.0270	0.0022

Table E.7.: ^{16}O, 19.6 MeV/u (166 keV/mu), anoxia

Dose, Gy	Survival	±SEM
0	0.9752	0.0080
0.5	0.7428	0.0911
1	0.6878	0.0127
2	0.2820	0.0390
3	0.1930	0.0073
4	0.0923	0.0001

Table E.8.: Extended normoxic target irradiation with ^{16}O

Position in depth, mm	Survival	±SEM
23.4	0.5191	0.0323
23.4	0.5293	0.0713
76.4	0.1147	0.0174
76.4	0.1048	0.0112
79.5	0.0838	0.0061
79.5	0.1069	0.0012
85.6	0.0993	0.0124
85.6	0.1116	0.0053
134.1	0.4950	0.0103
134.1	0.4826	0.0129
158.7	0.5574	0.0630
158.7	0.6281	0.1389

Table E.9.: Extended unevenly oxygenated target irradiation with ^{16}O

Position in depth, mm	Survival	±SEM
1.3	0.4609	0.0513
28.9	0.4464	0.0659
50.5	0.1299	0.0381
51.8	0.1331	0.0376
54.9	0.0953	0.0260
58.0	0.0884	0.0100
65.5	0.0880	0.0062
66.8	0.0895	0.0001
68.6	0.0927	0.0019
68.7	0.0809	0.0142
75.2	0.1191	0.0047
76.4	0.0929	0.0088
78.2	0.1085	0.0108
79.5	0.0944	0.0237
81.3	0.1210	0.0118
82.6	0.0982	0.0008
134.1	0.4355	0.0045
158.7	0.4772	0.0243

F Optimization accounting for a three-dimensional pO_2 distribution

In the older version of TRiP98-OER the tissue oxygenation values could be set only in one dimension along the beam path, which highly restricted the applicability of the TPS, making it useful for planning only the symmetrical fields configurations. As a part of the MoVe IT collaboration, the TRiP98-OER and the TRiP98-OER-multiion, updated in the frame of the current work, was improved by adding the option of reading the external oxygenation (hypoxia) maps. The structure of the hypoxia maps files and the procedure of its interpretation is similar to the ones for the CT data. Including the OER effect to the optimization requires the following:

- Functional PET (e.g. FMISO) uptake data cube with the same voxel number and size as the CT cube;
- A specific tracer (e.g. FMISO) uptake - pO_2 lookup table in a way similar to the typical Hounsfield look-up table used for CT numbers conversion. The planning tests in the current work are done using the table based on the model approach suggested by [Bowen et al., 2011] (Figure F.1);
- OER(pO_2, LET) tables containing the base data for the OER-LET interpolation.

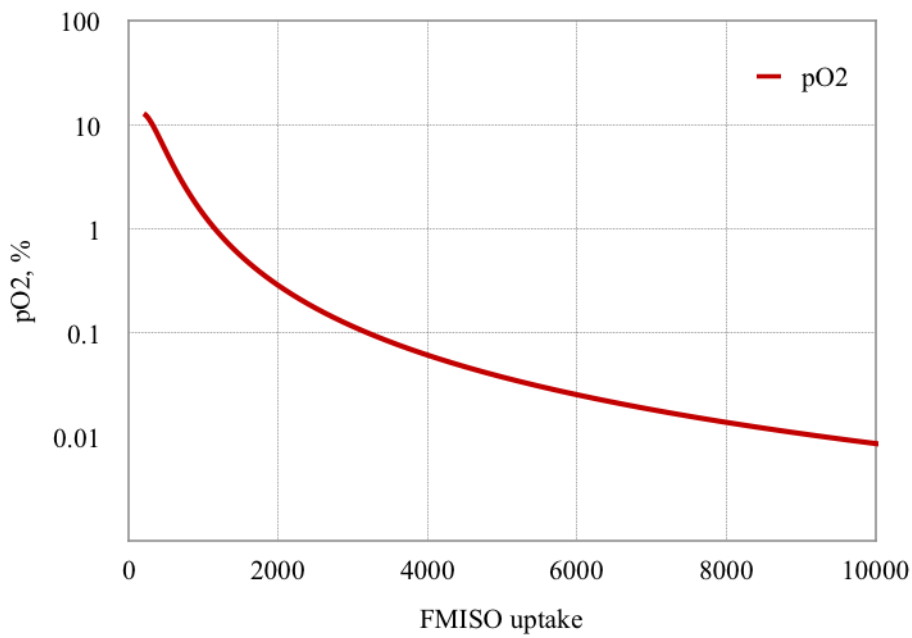

Figure F.1.: Visualization of the oxygenation lookup table generated according the [Bowen et al., 2011] approach. The *x*-axis values correspond to the FMISO uptake signal and the *y*-axis - to the recalculated pO_2 values.

Additionally, creating and loading the pO_2 distribution cubes, similar to those of Hounsfield numbers distribution cubes, is possible. This enables more realistic testing of the tool, including the cases with real patients with hypoxic tumors.

An example of the generated ellipsoid pO_2 inside a rectangular target is presented in Figure F.2. The oxygenation is gradually decreasing from 21% until 0% towards its center.

Figure F.3 shows the example of the optimization with two opposite fields of ^{16}O beams using kill-painting approach for a uniform survival of 10% in the target region. The same geometry, CT parameters and fields configuration as used in the Chapter 2 for the experiment with extended hypoxic target was used. The result of the optimization are the uniform biological (RBE- and OER-weighted) dose and the cell survival (Figures F.3(a), F.3(e), and F.3(d) and F.3(h)) achieved by delivering the physical dose boost to the central target part (Figures F.3(b) and F.3(f)). The resulting dose-averaged LET profile with a high-LET boost in the most hypoxic part is illustrated in Figures F.3(c) and F.3(g). The corresponding results for the optimization for the same geometry, but not accounting for the presence of hypoxia, are given in Figure F.4.

In both cases of oxygenation the dose and survival distributions look reasonable. An additional remark might be added concerning the dose-averaged LET distribution. One may notice that the area of the relatively high values of $\overline{\text{LET}}$ extends far beyond the target borders in lateral directions for both tests. The possible explanation to this effect can be the the presence in this region of the few high-LET particles delivering a very low total dose.

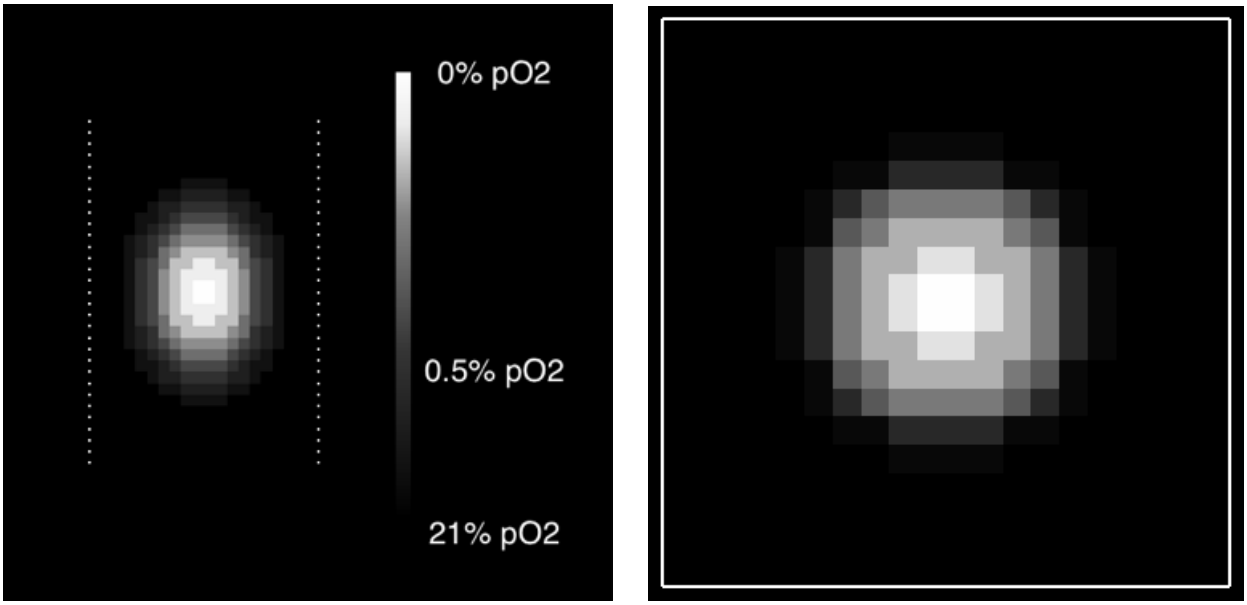

(a) (b)

Figure F.2.: Two projections of the hypoxia map describing the emulated pO_2 distribution in the target, gradually decreasing towards its center.

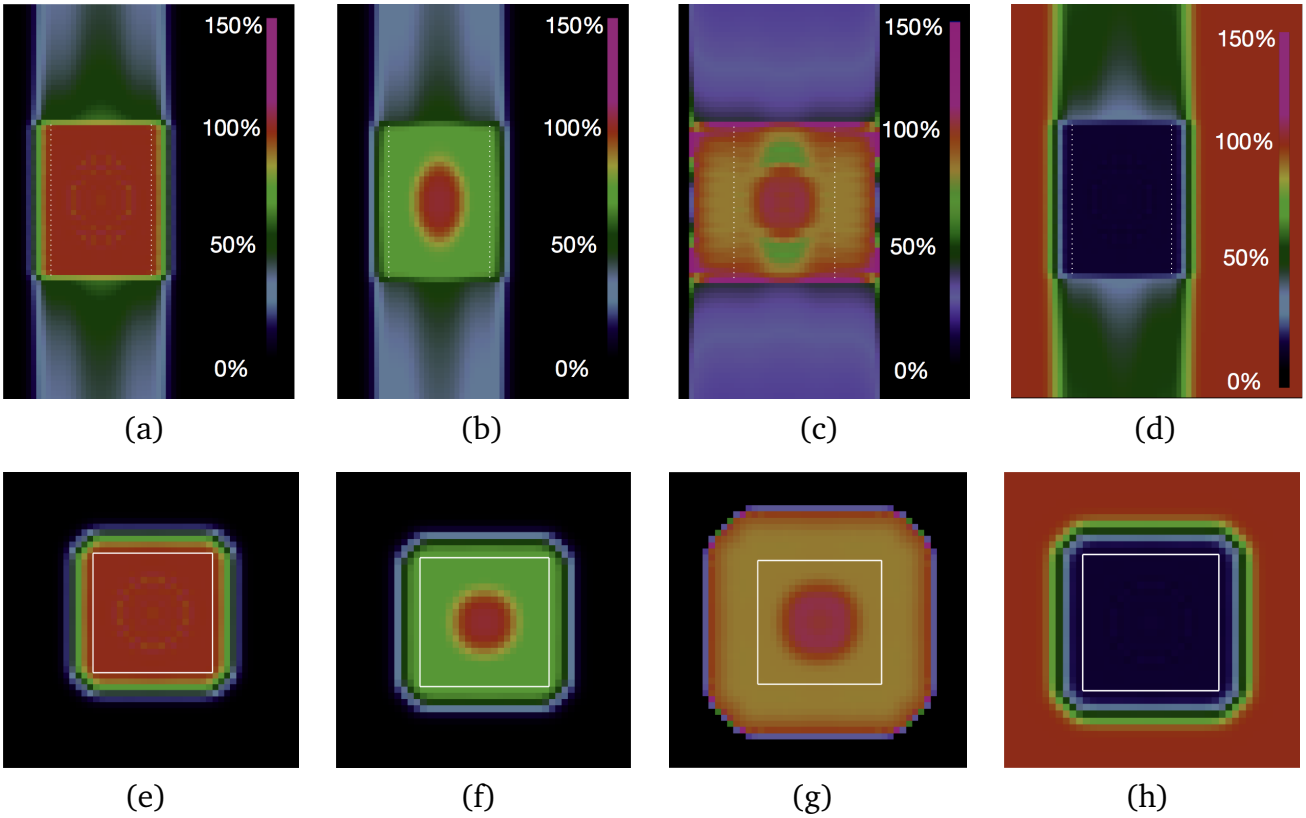

Figure F.3.: Plan optimized for a uniform survival of 10% in a target containing an ellipsoid hypoxic region in the center, irradiated with two opposite fields of ^{16}O ions. (a), (e) - RBE- and OER-weighted dose distribution, (b), (f) - absorbed dose distribution, (c), (g) - dose-averaged LET distribution, (d), (h) - survival distribution. In Figures (a), (b), (c) and (f) 100% stands for the dose of 6.5 Gy. In Figures (c) and (g) 100% stands for the 100 keV/μm and in Figures (d) and (e) - for 100% survival. The top and the bottom rows correspond to the coronal and axial panes.

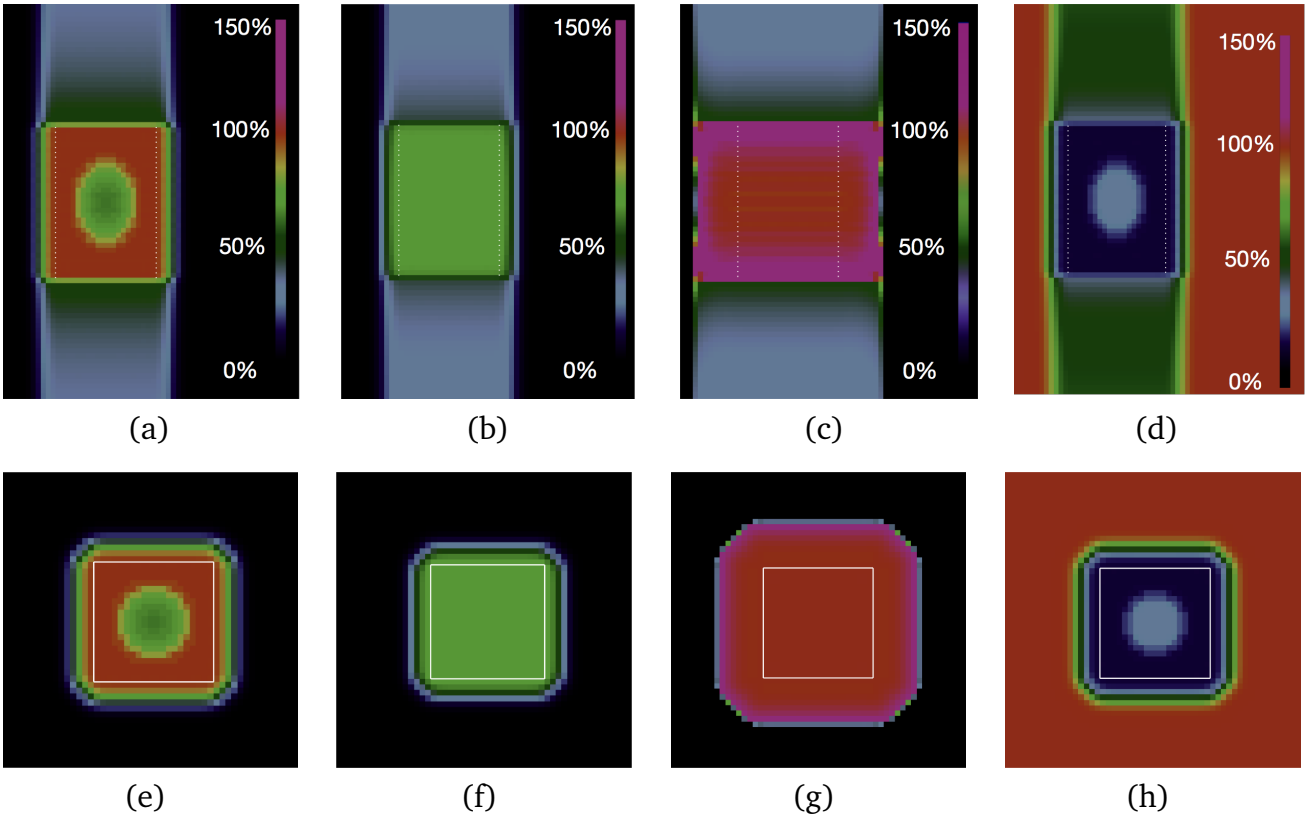

Figure F.4.: Plan optimized for an RBE-weighted dose of 6.5 Gy not accounting for the presence of an ellipsoid hypoxic region in the center, for opposite fields of ^{16}O ions. (a), (e) - RBE- and OER-weighted dose distribution, (b), (f) - absorbed dose distribution, (c), (g) - dose-averaged LET distribution, (d), (h) - survival distribution. In Figures (a), (b), (c) and (f) 100% stands for the dose of 6.5 Gy. In Figures (c) and (g) 100% stands for the 80 keV/μm and in Figures (d) and (e) - for 100% survival. The top and the bottom rows correspond to the coronal and axial panes

G Entrance channel survival data used for analysis in Chapter 3

Table G.1.: 4 Gy, 0.5 pO_2

Size, mm	^{12}C	^{4}He	^{16}O
1.0	0.708	0.737	0.719
1.2	0.709	0.735	0.709
1.6	0.710	0.729	0.717
1.8	0.714	0.728	0.714
2.0	0.698	0.716	0.715
2.2	0.700	0.712	0.707
2.4	0.693	0.712	0.696
2.8	0.693	0.703	0.704
3.0	0.692	0.697	0.701
3.2	0.680	0.691	0.703
3.6	0.683	0.688	0.695
3.8	0.678	0.682	0.694
4.0	0.676	0.677	0.691
4.2	0.665	0.671	0.691
4.4	0.662	0.655	0.689
4.8	0.656	0.661	0.682
5.0	0.647	0.646	0.675

Table G.2.: 4 Gy, 0.15 pO_2

Size, mm	^{12}C	^{4}He	^{16}O
1.0	0.704	0.717	0.709
1,2	0.698	0.718	0.686
1.6	0.696	0.702	0.708
1.8	0.697	0.705	0.708
2.0	0.682	0.687	0.702
2.2	0.673	0.674	0.691
2.4	0.674	0.673	0.691
2.8	0.664	0.655	0.689
3.0	0.651	0.644	0.681
3.2	0.653	0.644	0.684
3.6	0.641	0.627	0.673
3.8	0.639	0.625	0.673
4.0	0.627	0.612	0.667
4.2	0.613	0.599	0.656
4.4	0.609	0.599	0.655
4.8	0.605	0.585	0.643
5.0	0.581	0.580	0.634

Table G.3.: 6.5 Gy, 0.5 pO_2

Size, mm	^{12}C	^{4}He	^{16}O
1.0	0.527	0.567	0.529
1.2	0.516	0.567	0.512
1.6	0.518	0.559	0.524
1.8	0.524	0.557	0.522
2.0	0.504	0.539	0.522
2.2	0.502	0.533	0.512
2.4	0.491	0.534	0.495
2.8	0.497	0.524	0.506
3.0	0.486	0.512	0.506
3.2	0.481	0.502	0.505
3.6	0.477	0.500	0.492
3.8	0.474	0.496	0.492
4.0	0.468	0.485	0.492
4.2	0.452	0.477	0.487
4.4	0.448	0.460	0.484
4.8	0.439	0.462	0.473
5.0	0.427	0.443	0.464

Table G.4.: 6.5 Gy, 0.15 pO_2

Size, mm	^{12}C	^{4}He	^{16}O
1.0	0.509	0.543	0.513
1.2	0.504	0.541	0.494
1.6	0.498	0.527	0.512
1.8	0.501	0.519	0.512
2.0	0.478	0.502	0.502
2.2	0.467	0.476	0.487
2.4	0.471	0.478	0.489
2.8	0.454	0.454	0.484
3.0	0.435	0.439	0.473
3.2	0.435	0.438	0.478
3.6	0.420	0.416	0.460
3.8	0.408	0.414	0.462
4.0	0.403	0.400	0.452
4.2	0.377	0.387	0.438
4.4	0.376	0.391	0.436
4.8	0.371	0.370	0.419
5.0	0.355	0.360	0.408

Table G.5.: 7.5 Gy, 0.15 pO_2

Size, mm	^{12}C	^{4}He	^{16}O
1.0	0.457	0.505	0.457
1.2	0.444	0.503	0.438
1.6	0.446	0.495	0.450
1.8	0.453	0.494	0.449
2.0	0.430	0.476	0.450
2.2	0.428	0.469	0.426
2.4	0.417	0.470	0.417
2.8	0.424	0.459	0.433
3.0	0.404	0.448	0.433
3.2	0.406	0.433	0.431
3.6	0.402	0.432	0.418
3.8	0.402	0.432	0.421
4.0	0.393	0.417	0.417
4.2	0.370	0.409	0.412
4.4	0.372	0.395	0.408
4.8	0.362	0.392	0.398
5.0	0.350	0.373	0.390

Table G.6.: 7.5 Gy, 0.15 pO_2

Size, mm	^{12}C	^{4}He	^{16}O
1.0	0.434	0.479	0.440
1.2	0.429	0.484	0.428
1.6	0.423	0.466	0.438
1.8	0.427	0.464	0.438
2.0	0.404	0.441	0.428
2.2	0.390	0.427	0.412
2.4	0.395	0.432	0.412
2.8	0.384	0.406	0.410
3.0	0.355	0.396	0.398
3.2	0.360	0.394	0.402
3.6	0.342	0.377	0.383
3.8	0.348	0.376	0.385
4.0	0.326	0.357	0.374
4.2	0.304	0.351	0.360
4.4	0.304	0.350	0.358
4.8	0.293	0.330	0.340
5.0	0.277	0.320	0.330

Bibliography

Agostinelli, S., Allison, J., Amako, K. a., Apostolakis, J., Araujo, H., Arce, P., Asai, M., Axen, D., Banerjee, S., Barrand, G., et al. (2003). Geant4—a simulation toolkit. *Nuclear Instruments and Methods in Physics Research Section A: Accelerators, Spectrometers, Detectors and Associated Equipment*, 506(3):250–303.

Alper, T. and Bryant, P. (1974). Reduction in Oxygen Enhancement Ratio with Increase in LET: Tests of Two Hypotheses. *International Journal of Radiation Biology*, 26(3):203–218.

Antonovic, L. (2014). *Medical Radiation Physics, Department of Physics Stockholm University*. PhD thesis.

Astrahan, M. (2008). Some implications of linear-quadratic-linear radiation dose-response with regard to hypofractionation. *Medical Physics*, 35(9):4161–4172.

Barendsen, G. W. (1968). Responses of cultured cells, tumours, and normal tissues to radiations of different linear energy transfer. *Current Topics in Radiation Research*.

Bassler, N., Jäkel, O., Søndergaard, C. S., and Petersen, J. B. (2010). Dose- and LET-painting with particle therapy. *Acta Oncologica (Stockholm, Sweden)*, 49(July):1170–1176.

Bassler, N., Toftegaard, J., Lühr, A., Sørensen, B. S., Scifoni, E., Krämer, M., Jäkel, O., Mortensen, L. S., Overgaard, J., and Petersen, J. B. (2014). Let-painting increases tumour control probability in hypoxic tumours. *Acta Oncologica (Stockholm, Sweden)*, 53(1):25–32.

Battistoni, G., Cerutti, F., Fassò, A., Ferrari, A., Muraro, S., Ranft, J., Roesler, S., and Sala, P. R. (2007). The fluka code: description and benchmarking. *AIP Conference Proceedings*, 896(1):31–49.

Baumann, M., Krause, M., Overgaard, J., Debus, J., Bentzen, S. M., Daartz, J., Richter, C., Zips, D., and Bortfeld, T. (2016). Radiation oncology in the era of precision medicine. *Nature Reviews Cancer*, 16(4):234–249.

Baverstock, K. and Burns, W. (1976). Primary production of oxygen from irradiated water as an explanation for decreased radiobiological oxygen enhancement at high let. *Nature*, 260(5549):316–318.

Benjamin, L. C., Tree, A. C., and Dearnaley, D. P. (2017). The role of hypofractionated radiotherapy in prostate cancer. *Current Oncology Reports*, 19(4):30.

Bethe, H. (1930). Zur Theorie des Durchgangs schneller Korpuskularstrahlen durch Materie. *Annalen der Physik*, 397:325–400.

Bloch, F. (1933). Bremsvermögen von Atomen mit mehreren Elektronen. *Zeitschrift für Physik*, 81(5):363–376.

Böhlen, T. T., Bauer, J., Dosanjh, M., Ferrari, A., Haberer, T., Parodi, K., Patera, V., and Mairani, A. (2013). A monte carlo-based treatment-planning tool for ion beam therapy. *Journal of*

Radiation Research, 54(suppl_1):i77–i81.

Bopp, C., Hirayama, R., Inaniwa, T., Kitagawa, A., Matsufuji, N., and Koda, N. (2016). Adaptation of the microdosimetric kinetic model to hypoxia. *Physics in Medicine and Biology*, 61(21).

Bowen, S. R., van der Kogel, A. J., Nordsmark, M., Bentzen, S. M., and Jeraj, R. (2011). Characterization of positron emission tomography hypoxia tracer uptake and tissue oxygenation via electrochemical modeling. *Nuclear Medicine and Biology*, 38(6):771–780.

Bradt, H. L. and Peters, B. (1950). The heavy nuclei of the primary cosmic radiation. *Physical Review*, 77(1):54–70.

Brady, L. W. and Yaeger, T. E. (2013). *Encyclopedia of Radiation Oncology*. Springer Berlin Heidelberg, Berlin, Heidelberg.

Bragg, W. H. and Kleeman, R. (1905). On the α particles of radium, and their loss of range in passing through various atoms and molecules. *The London, Edinburgh, and Dublin Philosophical Magazine and Journal of Science*, 10(57):318–340.

Brahme, A. (2011). Accurate Description of the Cell Survival and Biological Effect at Low and High Doses and LET ' s. *Journal of Radiation Research*, 407:389–407.

Brizel, D. M., Scully, S. P., Harrelson, J. M., Layfield, L. J., Bean, J. M., Prosnitz, L. R., and Dewhirst, M. W. (1996). Tumor oxygenation predicts for the likelihood of distant metastases in human soft tissue sarcoma. *Cancer Research*, 56(5):941–943.

Brown, J. M. (2007). Tumor hypoxia in cancer therapy. *Methods in Enzymology*, 435:295–321.

Castro, J. R. (1995). Results of heavy ion radiotherapy. *Radiation and Environmental Biophysics*, 34(1):45–48.

Castro, J. R., Linstadt, D. E., Bahary, J.-P., Petti, P. L., Daftari, I., Collier, J., Gutin, P. H., Gauger, G., and Phillips, T. L. (1994). Experience in charged particle irradiation of tumors of the skull base: 1977-1992. *International Journal of Radiation Oncology* Biology* Physics*, 29(4):647 – 655.

Cheney, M. D., Chen, Y.-L., Lim, R., Winrich, B. K., Grosu, A. L., Trofimov, A. V., Depauw, N., Shih, H. A., Schwab, J. H., Hornicek, F. J., and DeLaney, T. F. (2014a). 18f-fmiso pet/ct visualization of tumor hypoxia in patients with chordoma of the mobile and sacrococcygeal spine. *International Journal of Radiation Oncology* Biology* Physics*, 90(5):1030–1036.

Cheney, M. D., Chen, Y.-L., Lim, R., Winrich, B. K., Grosu, A. L., Trofimov, A. V., Depauw, N., Shih, H. A., Schwab, J. H., Hornicek, F. J., et al. (2014b). [18f]-fluoromisonidazole positron emission tomography/computed tomography visualization of tumor hypoxia in patients with chordoma of the mobile and sacrococcygeal spine. *International Journal of Radiation Oncology* Biology* Physics*, 90(5):1030–1036.

Chu, W. T., Ludewigt, B. A., and Renner, T. R. (1993). Instrumentation for treatment of cancer using proton and light-ion beams. *Review of Scientific Instruments*, 64(8):2055–2122.

de Vera, P., Abril, I., and Garcia-Molina, R. (2014). Water equivalent properties of materials commonly used in proton dosimetry. *Applied Radiation and Isotopes*, 83:122–127.

Dokic, I., Mairani, A., Niklas, M., Zimmermann, F., Jäkel, O., Debus, J., Haberer, T., and Abdollahi, A. (2016). Next generation multi-scale biophysical characterization of high precision cancer particle radiotherapy using clinical proton , helium- , carbon- and oxygen ion beams. *Oncotarget*, 7(35).

Durante, M. and Loeffler, J. S. (2009). Charged particles in radiation oncology. *Nature Reviews Clinical Oncology*, 7:37 EP –.

Durante, M. and Paganetti, H. (2016). Nuclear physics in particle therapy: a review. *Reports on Progress in Physics*, 79(9):096702.

Eales, K. L., Hollinshead, K. E. R., and Tennant, D. A. (2016). Hypoxia and metabolic adaptation of cancer cells. *Oncogenesis*, 5(1):e190.

Elsässer, T., Weyrather, W. K., Friedrich, T., Durante, M., Iancu, G., Krämer, M., Kragl, G., Brons, S., Winter, M., Weber, K. J., and Scholz, M. (2010). Quantification of the relative biological effectiveness for ion beam radiotherapy: Direct experimental comparison of proton and carbon ion beams and a novel approach for treatment planning. *International Journal of Radiation Oncology* Biology* Physics*, 78(4):1177–1183.

Erickson, L. A., Highsmith, W. E., Fei, P., and Zhang, J. (2015). Targeting the hypoxia pathway to treat pancreatic cancer. *Drug Design, Development and Therapy*, 9:2029–2031.

Erkan, M., Kurtoglu, M., and Kleeff, J. (2016). The role of hypoxia in pancreatic cancer: a potential therapeutic target? *Expert Review of Gastroenterology & Hepatology*, 10(3):301–316. PMID: 26560854.

Eschmann, S.-M., Paulsen, F., Reimold, M., Dittmann, H., Welz, S., Reischl, G., Machulla, H.-J., and Bares, R. (2005). Prognostic impact of hypoxia imaging with 18f-misonidazole pet in non-small cell lung cancer and head and neck cancer before radiotherapy. *The Journal of Nuclear Medicine*, 46(2):253–260.

Fano, U. (1963). Penetration of protons, alpha particles, and mesons. *Annual Review of Nuclear Science*, 13(1):1–66.

Fleming, I. N., Manavaki, R., Blower, P. J., West, C., Williams, K. J., Harris, A. L., Domarkas, J., Lord, S., Baldry, C., and Gilbert, F. J. (2015). Imaging tumour hypoxia with positron emission tomography. *British Journal of Cancer*, 112(238-250).

Fraga, A., Ribeiro, R., Príncipe, P., Lopes, C., and Medeiros, R. (2015). Hypoxia and prostate cancer aggressiveness: A tale with many endings. *Clinical Genitourinary Cancer*, 13(4):295 – 301.

Friedrich, T., Durante, M., and Scholz, M. (2013a). The local effect model-principles and applications. *The Health Risks of Extraterrestrial Environments*.

Friedrich, T., Scholz, U., Elsässer, T., Durante, M., and Scholz, M. (2012). Calculation of the biological effects of ion beams based on the microscopic spatial damage distribution pattern. *International Journal of Radiation Biology*, 88(1-2):103–107.

Friedrich, T., Scholz, U., Elsasser, T., Durante, M., and Scholz, M. (2013b). Systematic analysis of rbe and related quantities using a database of cell survival experiments with ion beam

irradiation. *Journal of Radiation Research*, 54(3):494–514.

Furusawa, Y., Fukutsu, K., Aoki, M., Itsukaichi, H., Eguchi-Kasai, K., Ohara, H., Yatagai, F., Kanai, T., and Ando, K. (2000). Inactivation of aerobic and hypoxic cells from three different cell lines by accelerated (3)He-, (12)C- and (20)Ne-ion beams. *Radiation Research*, 154(5):485–496.

Gademann, G., Schlegel, W., Bürkelbach, J., Laier, C., Behrens, S., Brieger, S., and Wannenmacher, M. (1993). Three-dimensional radiation planning. studies on clinical integration. *Strahlentherapie und Onkologie*, 169(3):159—167.

Gemmel, A., Hasch, B., Ellerbrock, M., Kraft-Weyrather, W., and Krämer, M. (2008). Biological dose optimization with multiple ion fields. *Physics in Medicine and Biology*, 53:6691–701.

Gottschalk, B., Koehler, A. M., Schneider, R. J., Sisterson, J. M., and Wagner, M. S. (1993). Multiple coulomb scattering of 160 mev protons. *Nuclear Instruments and Methods in Physics Research Section B: Beam Interactions with Materials and Atoms*, 74(4):467–490.

Grevillot, L., Bertrand, D., Dessy, F., Freud, N., and Sarrut, D. (2012). Gate as a geant4-based monte carlo platform for the evaluation of proton pencil beam scanning treatment plans. *Physics in Medicine and Biology*, 57(13):4223.

Grimes, D. R. and Partridge, M. (2015). A mechanistic investigation of the oxygen fixation hypothesis and oxygen enhancement ratio. *Biomedical Physics & Engineering Express*, 1(4):045209.

Grumezescu, A. (2016). *Nanobiomaterials in Medical Imaging: Applications of Nanobiomaterials, 1st edition*. William Andrew.

Grün, R., Friedrich, T., Elsässer, T., Krämer, M., Zink, K., Karger, C. P. P., Durante, M., Engenhart-Cabillic, R., and Scholz, M. (2012). Impact of enhancements in the local effect model (LEM) on the predicted RBE-weighted target dose distribution in carbon ion therapy. *Physics in Medicine and Biology*, 57(22):7261–7274.

Grün, R., Friedrich, T., Krämer, M., Zink, K., Durante, M., Engenhart-Cabillic, R., and Scholz, M. (2015). Assessment of potential advantages of relevant ions for particle therapy: a model based study. *Medical Physics*, 42(2):1037–1047.

Haberer, T., Abdollahi, A., Brons, S., Dokic, I., Ellerbrock, M., Mairani, A., Andreas, P., Tessonnier, T., Debus, J., and Jäkel, O. (2017). Commissioning of helium beams for radiotherapy at the heidelberg ion beam therapy facility at the university clinic. In *56th Annual Conference of the Particle Therapy Co-operative Group (PTCOG56) Abstract book*.

Habermehl, D., Ilicic, K., Dehne, S., Rieken, S., Orschiedt, L., Brons, S., Haberer, T., Weber, K. J., Debus, J., and Combs, S. E. (2014). The relative biological effectiveness for carbon and oxygen ion beams using the raster-scanning technique in hepatocellular carcinoma cell lines. *PLoS ONE*, 9(12):1–10.

Hall, E. J. and Cox, J. D. (2010). Chapter 1 - physical and biologic basis of radiation therapy. In Cox, J. D. and Ang, K. K., editors, *Radiation Oncology (NINTH EDITION)*, pages 3 – 49. Content Repository Only!, Philadelphia, ninth edition edition.

Hall, E. J. and Giaccia, A. J. (2006). *Radiobiology for the Radiologist*. Lippincott Williams & Wilkins.

Highland, V. L. (1975). Some practical remarks on multiple scattering. *Nuclear Instruments and Methods*, 129(2):497–499.

Hoppe-Seyler, K., Mändl, J., Adrian, S., Kuhn, B. J., and Hoppe-Seyler, F. (2017). Virus/host cell crosstalk in hypoxic hpv-positive cancer cells. *Viruses*, 9(7):174.

Horcicka, M., Meyer, C., Buschbacher, a., Durante, M., and Krämer, M. (2013). Algorithms for the optimization of RBE-weighted dose in particle therapy. *Physics in Medicine and Biology*, 58(2):275–86.

Horsman, M. R., Mortensen, L. S., Petersen, J. B., Busk, M., and Overgaard, J. (2012). Imaging hypoxia to improve radiotherapy outcome. *Nature Reviews Clinical Oncology*, 9(12):674–687.

Hüfner, J., Schäfer, K., and Schürmann, B. (1975). Abrasion-ablation in reactions between relativistic heavy ions. *Physical Review C (Nuclear Physics)*, 12(6):1888–1898.

ICRU (1993). Prescribing, recording and reporting photon beam therapy. Report 50, ICRU.

Inaniwa, T., Kanematsu, N., Noda, K., and Kamada, T. (2017). Treatment planning of intensity modulated composite particle therapy with dose and linear energy transfer optimization. *Physics in Medicine and Biology*, pages 1–23.

Jäkel, O., Hartmann, G. H., Karger, C. P., Heeg, P., and Vatnitsky, S. (2004). A calibration procedure for beam monitors in a scanned beam of heavy charged particles. *Medical Physics*, 31(5):1009–1013.

Jäkel, O., Karger, C. P., and Debus, J. (2008). The future of heavy ion radiotherapy. *Medical Physics*, 35(12):5653–5663.

Janssen, H. L., Haustermans, K. M., Balm, A. J., and Begg, A. C. (2005). Hypoxia in head and neck cancer: How much, how important? *Head & Neck*, 27(7):622–638.

Jermann, M. (2011). Hadron therapy patient statistics (data recieved per may 2011; ptcog50). `https://www.ptcog.ch/archive/patient_statistics/Patientstatistics-updateMay2011.pdf`.

Jermann, M. (2016). Particle therapy patient statistics (per end of 2015). `https://www.ptcog.ch/archive/patient_statistics/Patientstatistics-updateDec2015.pdf`.

Kanai, T., Kawachi, K., and Matsuzawa, H. (1983). Three-dimensional beam scanning for proton therapy. *Nuclear Instruments and Methods*, 214:491–496.

Karger, C. P., Jäkel, O., Hartmann, G. H., and Heeg, P. (1999). A system for three-dimensional dosimetric verification of treatment plans in intensity-modulated radiotherapy with heavy ions. *Medical Physics*, 26(10):2125–2132.

Karger, C. P., Peschke, P., Sanchez-Brandelik, R., Scholz, M., and Debus, J. (2006). Radiation tolerance of the rat spinal cord after 6 and 18 fractions of photons and carbon ions: experimental results and clinical implications. *International Journal of Radiation Oncology* Biology* Physics*, 66(5):1488—1497.

Kox, S., Gamp, A., Perrin, C., Arvieux, J., Bertholet, R., Bruandet, J. F., Buenerd, M., Cherkaoui, R., Cole, A. J., El-Masri, Y., Longequeue, N., Menet, J., Merchez, F., and Viano, J. B. (1987). Trends of total reaction cross sections for heavy ion collisions in the intermediate energy range. *Physical Review C*, 35(5):1678–1691.

Kraft, G. (2000). Tumor therapy with heavy charged particles. *Progress in Particle and Nuclear Physics*, 45(Supplement 2):S473—-S544.

Kraft, G. (2007). Tumor therapy with heavy ions.

Kraft-Weyrather, W., Kraft, G., Ritter, S., Scholz, M., and Stanton, J. A. (1989). The preparation of biological targets for heavy-ion experiments up to 20 MeV/u. *Nuclear Instruments and Methods in Physics Research Section A: Accelerators, Spectrometers, Detectors and Associated Equipment*, 282(1):22–27.

Krämer, M. and Durante, M. (2010). Ion beam transport calculations and treatment plans in particle therapy. *European Physical Journal D*, 60(1):195–202.

Krämer, M., Jäkel, O., Haberer, T., Schardt, D., and Weber, U. (2000). Treatment planning for heavy-ion radiotherapy: physical beam model and dose optimization. *Physics in Medicine and Biology*, 3299.

Krämer, M. and Scholz, M. (2006). Rapid calculation of biological effects in ion radiotherapy. *Physics in Medicine and Biology*, 51(8):1959–1970.

Krämer, M., Scifoni, E., Schmitz, F., Sokol, O., and Durante, M. (2014). Overview of recent advances in treatment planning for ion beam radiotherapy. *The European Physical Journal D*, 68(10):306.

Krämer, M., Scifoni, E., Schuy, C., Rovituso, M., Tinganelli, W., Maier, A., Kaderka, R., Kraft-Weyrather, W., Brons, S., Tessonnier, T., Parodi, K., and Durante, M. (2016). Helium ions for radiotherapy? Physical and biological verifications of a novel treatment modality. *Medical Physics*, 43(4):1995–2004.

Krämer, M., Weyrather, W. K., and Scholz, M. (2003). The increased biological effectiveness of heavy charged particles: from radiobiology to treatment planning. *Technology in Cancer Research & Treatment*, 2(5):427–436.

Kurz, C., Mairani, A., and Parodi, K. (2012). First experimental-based characterization of oxygen ion beam depth dose distributions at the Heidelberg Ion-Beam Therapy Center. *Physics in Medicine and Biology*, 57(15):5017–5034.

Loeffler, J. S. and Durante, M. (2013). Charged particle therapy- optimization, challenges and future directions. *Nature Reviews Clinical Oncology*, 10(7):411–424.

Lühr, A., Hansen, D. C., Teiwes, R., Sobolevsky, N., Jäkel, O., and Bassler, N. (2012). The impact of modeling nuclear fragmentation on delivered dose and radiobiology in ion therapy. *Physics in Medicine and Biology*, 57(16):5169.

Ma, N. Y., Tinganelli, W., Maier, A., Durante, M., and Kraft-Weyrather, W. (2013). Influence of chronic hypoxia and radiation quality on cell survival. *Journal of Radiation Research*, 54(SUPPL.1):23–30.

MacCabee, H. D. and Ritter, M. A. (1974). Fragmentation of high-energy oxygen-ion beams in water. *Radiation Research*, 60(3):409–421.

Mairani, A., Böhlen, T. T., Schiavi, A., Tessonnier, T., Molinelli, S., Brons, S., Battistoni, G., Parodi, K., and Patera, V. (2013). A Monte Carlo-based treatment planning tool for proton therapy. *Physics in Medicine and Biology*, 58(8):2471–90.

Marignol, L., Coffey, M., Lawler, M., and Hollywood, D. (2008). Hypoxia in prostate cancer: A powerful shield against tumour destruction? *Cancer Treatment Reviews*, 34(4):313 – 327.

Mena-Romano, P., Cheng, C., Glowa, C., Peschke, P., Pan, L., Haberkorn, U., Dimitrakopoulou-Strauss, A., and Karger, C. P. (2015). Measurement of hypoxia-related parameters in three sublines of a rat prostate carcinoma using dynamic (18)f-fmiso-pet-ct and quantitative histology. *American Journal of Nuclear Medicine and Molecular Imaging*, 5(4):348–362.

Michael, B. (1996). A multiple-radical model for radiation action on dna and the dependence of oer on let. *International Journal of Radiation Biology*, 69(3):351–358.

Miller, R. C., Marino, S. A., Brenner, D. J., Martin, S. G., Richards, M., Randers-Pehrson, G., and Hall, E. J. (1995). The biological effectiveness of radon-progeny alpha particles. ii. oncogenic transformation as a function of linear energy transfer. *Radiation Research*, 142(1):54–60.

Mitaroff, A., Kraft-Weyrather, W., Geiss, O. B., and Kraft, G. (1998). Biological verification of heavy ion treatment planning. *Radiation and Environmental Biophysics*, 37(1):47–51.

Moliére, G. (1948). Theorie der Streuung schneller geladener Teilchen ii. Mehrfach- und Vielfachstreuung. *Zeitschrift für Naturforschung A*, 3:78–97.

Ng, C. S., Kodama, Y., Mullani, N. A., Barron, B. J., Wei, W., Herbst, R. S., Abbruzzese, J. L., and Charnsangavej, C. (2009). Tumor blood flow measured by perfusion computed tomography and 15o-labeled water positron emission tomography: a comparison study. *Journal of Computer Assisted Tomography*, 33(3):460–465.

O'Connor, J. P. B., Boult, J. K. R., Jamin, Y., Babur, M., Finegan, K. G., Williams, K. J., Little, R. A., Jackson, A., Parker, G. J. M., Reynolds, A. R., Waterton, J. C., and Robinson, S. P. (2016). Oxygen-enhanced mri accurately identifies, quantifies, and maps tumor hypoxia in preclinical cancer models. *Cancer Research*, 76(4):787.

Pathak, R., Dey, S. K., Sarma, A., and Khuda-Bukhsh, A. R. (2007). Cell killing, nuclear damage and apoptosis in Chinese hamster V79 cells after irradiation with heavy-ion beams of 16O, 12C and 7Li. *Mutation Research - Genetic Toxicology and Environmental Mutagenesis*, 632(1-2):58–68.

PTCOG (2016a). Particle therapy facilities in operation (last update: July 2017). `https://www.ptcog.ch/index.php/facilities-in-operation`.

PTCOG (2016b). Particle therapy facilities under construction (last update: June 2017). `https://www.ptcog.ch/index.php/facilities-under-construction`.

PTW (2017). Ionizing radiation detectors including codes of practice. `http://www.ptw.de/fileadmin/data/download/catalogviewer/DETECTORS_Cat_en_16522900_10/`

blaetterkatalog/index.html?startpage=22#page_1.

Resch, A. F., Fuchs, H., and Georg, D. (2017). Benchmarking gate/geant4 for 16 o ion beam therapy. *Physics in Medicine and Biology*, 62(18):N474.

Rupp, N. J., Schüffler, P. J., Zhong, Q., Falkner, F., Rechsteiner, M., Rüschoff, J. H., Fankhauser, C., Drach, M., Largo, R., Tremp, M., Poyet, C., Sulser, T., Kristiansen, G., Moch, H., Buhmann, J., Müntener, M., and Wild, P. J. (2016). Oxygen supply maps for hypoxic microenvironment visualization in prostate cancer. *Journal of Pathology Informatics*, 7:3.

Schall, I., Schardt, D., Geissel, H., Irnich, H., Kankeleit, E., Kraft, G., Magel, A., Mohar, M. F., Münzenberg, G., Nickel, F., Scheidenberger, C., and Schwab, W. (1996). Charge-changing nuclear reactions of relativistic light-ion beams ($5 \leq z \leq 10$) passing through thick absorbers. *Nuclear Instruments and Methods in Physics Research Section B: Beam Interactions with Materials and Atoms*, 117(3):221–234.

Schardt, D. (2007). Precision bragg-curve measurements for light-ion beams in water. *GSI Scientific Report*.

Schardt, D., Elsässer, T., and Schulz-Ertner, D. (2010). Heavy-ion tumor therapy: physical and radiobiological benefits. *Reviews of Modern Physics*, 82(1):383.

Schardt, D., Schall, I., Geissel, H., Irnich, H., Kraft, G., Magel, A., Mohar, M. F., Münzenberg, G., Nickel, F., Scheidenberger, C., Schwab, W., and Sihver, L. (1996). Nuclear fragmentation of high-energy heavy-ion beams in water. *Advances in Space Research*, 17(2):87–94.

Schicker, C., Von Neubeck, C., Kopf, U., and Kraft-Weyrather, W. (2009). Zellkulturbestrahlungskammer. *Europe Patent specification EP090024027*.

Schmidt, A. (2005). Examinations on multiple field optimization in ion therapy. Diploma thesis, Technische Universität Darmstadt Institut für Kernphysik.

Scholz, M. (2003). Effects of Ion Radiation on Cells and Tissues BT - Radiation Effects on Polymers for Biological Use. *Advances in Polymer Science*, 162:95–155.

Scholz, M., Kellerer, A. M., Kraft-Weyrather, W., and Kraft, G. (1997). Computation of cell survival in heavy ion beams for therapy: The model and its approximation. *Radiation and Environmental Biophysics*, 36(1):59–66.

Scholz, M. and Kraft, G. (1996). Track structure and the calculation of biological effects of heavy charged particles. *Advances in Space Research*, 18(1-2):5–14.

Schulz-Ertner, D., Nikoghosyan, A., Didinger, B., Münter, M., Jäkel, O., Karger, C. P., and Debus, J. (2005). Therapy strategies for locally advanced adenoid cystic carcinomas using modern radiation therapy techniques. *Cancer*, 104(2):338–344.

Schwaab, J., Brons, S., Fieres, J., and Parodi, K. (2011). Experimental characterization of lateral profiles of scanned proton and carbon ion pencil beams for improved beam models in ion therapy treatment planning. *Physics in Medicine and Biology*, 56(24):7813.

Scifoni, E., Tinganelli, W., Kraft-Weyrather, W., Durante, M., Maier, A., and Krämer, M. (2013). Including oxygen enhancement ratio in ion beam treatment planning: model implementation and experimental verification. *Physics in Medicine and Biology*, 58(11):3871–3895.

Serber, R. (1947). Nuclear reactions at high energies. *Physical Review*, 72(11):1114–1115.

Sihver, L., Tsao, C. H., Silberberg, R., Kanai, T., and Barghouty, A. F. (1993). Total reaction and partial cross section calculations in proton-nucleus (z_t <= 26) and nucleus-nucleus reactions (z_p and z_t <= 26). *Physical Review C*, 47(3):1225–1236.

Sokol, O., Scifoni, E., Tinganelli, W., Kraft-Weyrather, W., Wiedemann, J., Maier, A., Boscolo, D., Friedrich, T., Brons, S., Durante, M., and Krämer, M. (2017). Oxygen beams for therapy: advanced biological treatment planning and experimental verification. *Physics in Medicine and Biology*, 62(19):7798.

Stewart, R. D., Yu, V. K., Georgakilas, A. G., Koumenis, C., Park, J. H., and Carlson, D. J. (2011). Effects of radiation quality and oxygen on clustered dna lesions and cell death. *Radiation Research*, 176(5):587–602.

Strigari, L., Torriani, F., Manganaro, L., Inaniwa, T., Dalmasso, F., Cirio, R., and Attili, A. (2017). Tumor control in ion beam radiotherapy with different ions in presence of hypoxia: an oxygen enhancement ratio model based on the microdosimetric kinetic model. *Physics in Medicine and Biology*.

Tarasov, O. B. and Bazin, D. (2008). Lise++: Radioactive beam production with in-flight separators. *Nuclear Instruments and Methods in Physics Research Section B: Beam Interactions with Materials and Atoms*, 266:4657–4664.

Tessonnier, T., Böhlen, T. T., Ceruti, F., Ferrari, A., Sala, P., Brons, S., Haberer, T., Debus, J., Parodi, K., and Mairani, A. (2017a). Dosimetric verification in water of a monte carlo treatment planning tool for proton, helium, carbon and oxygen ion beams at the heidelberg ion beam therapy center. *Physics in Medicine and Biology*, 62(16):6579.

Tessonnier, T., Mairani, A., Brons, S., Haberer, T., Debus, J., and Parodi, K. (2017b). Experimental dosimetric comparison of 1H, 4He, 12C and 16O scanned ion beams. *Physics in Medicine and Biology*, 62:3958–3982.

Tinganelli, W., Durante, M., Hirayama, R., Krämer, M., Maier, A., Kraft-Weyrather, W., Furusawa, Y., Friedrich, T., and Scifoni, E. (2015). Kill-painting of hypoxic tumours in charged particle therapy. *Scientific Reports*, 5:17016.

Tinganelli, W., Ma, N.-Y., Von Neubeck, C., Maier, A., Schicker, C., Kraft-Weyrather, W., and Durante, M. (2013). Influence of acute hypoxia and radiation quality on cell survival. *Journal of Radiation Research*, 54(suppl_1):i23–i30.

Tobias, C., Blakely, E., Alpen, E., Castro, J., Ainsworth, E., Curtis, S., Ngo, F., Rodriguez, A., Roots, R., Tenfordf, T., et al. (1982). Molecular and cellular radiobiology of heavy ions. *International Journal of Radiation Oncology* Biology* Physics*, 8(12):2109–2120.

Tobias, C., Lyman, J. T., Chatterjee, A., Howard, J., Maccabee, H. D., Raju, M. R., Smith, A. R., Sperinde, J. M., and Welch, G. P. (1971). Radiological physics characteristics of the extracted heavy ion beams of the bevatron. *Science*, 174(4014):1131–1134.

Todd, P. W. (1975). Heavy-ion irradiation of human and chinese hamster cells in vitro. *Radiation Research*, 61(2):288–297.

Toma-Daşu, I., Daşuu, A., and Brahmeu, A. (2009). *Quantifying Tumour Hypoxia By Pet Imaging - A Theoretical Analysis*, pages 267–272. Springer US, Boston, MA.

Tommasino, F., Scifoni, E., and Durante, M. (2015). New Ions for Therapy. *International Journal of Particle Therapy*, pages IJPT–15–00027.1.

Toshiba (2017). Advancements in beam acceleration and delivery. International Symposium on Ion Therapy (ISIT).

Tripathi, R. K., Cucinotta, F. A., and Wilson, J. W. (1996). Accurate universal parameterization of absorption cross sections. *Nuclear Instruments and Methods in Physics Research Section B: Beam Interactions with Materials and Atoms*, 117(4):347–349.

Tripathi, R. K., Cucinotta, F. A., and Wilson, J. W. (1999). Accurate universal parameterization of absorption cross sections iii –light systems. *Nuclear Instruments and Methods in Physics Research Section B: Beam Interactions with Materials and Atoms*, 155(4):349–356.

Unkelbach, J., Botas, P., Giantsoudi, D., Gorissen, B. L., and Paganetti, H. (2016). Reoptimization of intensity modulated proton therapy plans based on linear energy transfer. *International Journal of Radiation Oncology* Biology* Physics*, 96(5):1097–1106.

Vavilov, P. V. (1957). Ionization losses of high-energy heavy particles. *Sov. Phys. JETP*, 5:749–751.

von Neubeck, C. (2006). *Aufbau eines 3-dimensionalen Systems zur biologischen Verifikation der Bestrahlungsplanung mit Schwerionen*. PhD thesis.

von Sonntag, C. (1987). *The chemical basis of radiation biology*. Taylor & Francis London.

Wenzl, T. and Wilkens, J. J. (2011). Theoretical analysis of the dose dependence of the oxygen enhancement ratio and its relevance for clinical applications. *Radiation Oncology*, 6(1):171.

Wilson, W. R. and Hay, M. P. (2011). Targeting hypoxia in cancer therapy. *Nature reviews. Cancer*, 11(6):393.

Wulf, H., Kraft-Weyrather, W., Miltenburger, H., Blakely, E., Tobias, C., and Kraft, G. (1985). Heavy-ion effects on mammalian cells: inactivation measurements with different cell lines. *Radiation Research*, 104(2s):S122–S134.

Acknowledgments

I would like to start by saying big thanks to Prof. Marco Durante who made the whole thing possible by inviting me to do my PhD studies at GSI and giving me this exciting project. To Emanuele Scifoni, for introducing me to the topic and for all his guidance, patience, and support in the most stressful moments. Huge thanks to Michael Krämer, for being always available for answering my numerous questions, sharing his endless knowledge and giving me the opportunities to present my results and the results of the group at the most important conferences. Thanks to Martina Fuß for all the long fruitful discussions that we had during the last year. I also would like to thank Prof. Thomas Aumann for being the second reviewer of this work.

Thanks to the HGS-HIRe for FAIR team for supporting and coordinating not only me, but many other PhD students, and making me meet so many great people during this time.

Big thanks to the whole beamtime team for all the productive working days and nights we had! Grazie to Walter Tinganelli for being the best teacher in the radiobiological lab, and for making me hate few particular songs on the radio. Danke to Julia Wiedemann for all the fun we had while preparing hundreds of rings, staining thousands of flasks and dishes, and for teaching me the long German words. To Andreas Maier for his countless explanations on how to deal with the gas bottles (still not sure if I remember). Our experimental work would never be complete without the support of the HIT team, in particular, Stephan Brons, to whom I am especially grateful for all his kind assistance during and after our beamtimes.

Thanks to Wilma Kraft-Weyrather, for being always there to give me precious advice in the moments of doubts. Thanks to Thomas Friedrich for his help regarding all the LEM- and RBE-related things. Thanks to Sebastian Hild for sharing his computer knowledge and helping me to progress much faster. To Rebecca Grün, Christoph Schuy, and Norman Reppingen - for the friendly office atmosphere we kept. And, of course, to my eternal office mate, Daria Boscolo, with whom we shared everyday joys and burdens of PhD life.

This time brought me together with so many great people that I would never meet otherwise. Thank you so much, Dimitri, Bjorn, Fredo, Katharina, Sofija, Marta, Pavel, Felix for all the lunches, dinners, parties and travels we shared. And, of course, thanks to all my Russian friends for still being the important part of my life.

These last three years were definitely the most challenging, and I would never manage to complete this work without the endless support of the people, that mean the most to me. I want to thank my parents for supporting me in every situation all this time despite hundreds of kilometers between us. My grandparents, whose dream was to see me getting a Doctor degree, which is really close to coming true now. The last "thank you" I want to say to my beloved husband, Ivan. I cannot imagine getting through all the hard times without you being next to

me. Thank you for always inspiring me to grow as a scientist and a person, and for being my strictest referee.

Lebenslauf Olga Sokol

Persönliche Daten

Name	Olga Sokol
Geburtstag	17 Juli 1991
Geburtsort	Dubna, Russland
Nationalität	Russisch

Universitäre Ausbildung

seit 02/2015	Mitglied der Helmholtz Graduate School for Hadron and Ion Research (HGS-HIRe)
seit 11/2014	TU Darmstadt Promotion (Durchführung an der GSI)
09/2008 - 12/2013	Lomonossow-Universität Moskau, Russland Fachbereich Physik Titel der Diplomarbeit: Mathematische Modellierung der ionotropen Rezeptorexpression im Hippocampus von Nagetieren unter Einwirkung schwerer geladener Teilchen

Schulische Ausbildung

09/1997 - 05/2002	Grundschule, Dubna, Russland
09/2002 - 06/2008	Lyceum Nr. 6 benannt nach Akademiemitglied G.N. Flerov, Dubna, Russland

Erklärung zur Dissertation

Hiermit versichere ich, die vorliegende Dissertation ohne Hilfe Dritter nur mit den angegebenen Quellen und Hilfsmitteln angefertigt zu haben. Alle Stellen, die aus Quellen entnommen wurden, sind als solche kenntlich gemacht. Diese Arbeit hat in gleicher oder ähnlicher Form noch keiner Prüfungsbehörde vorgelegen.

Darmstadt, den April 13, 2018

(Olga Sokol)